Recurrence Based Purification of Qudit Graph States

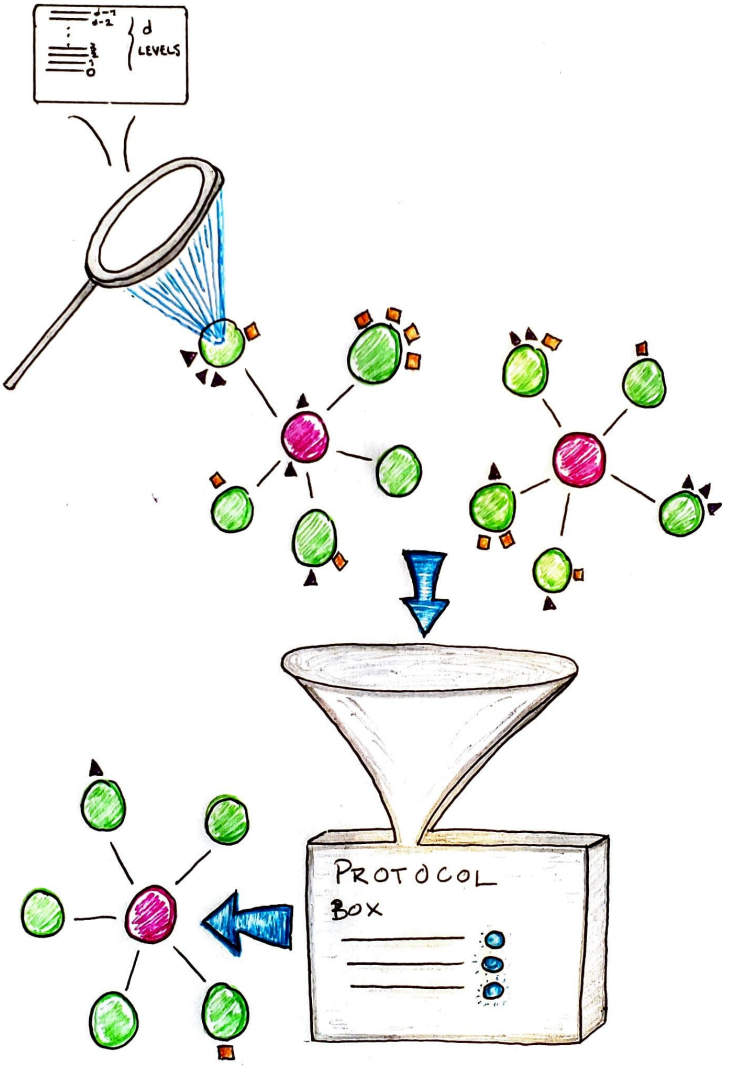

SCARLETT GAUTHIER

Recurrence Based Purification of Qudit Graph States

by

Scarlett Gauthier

to obtain the degree of Master of Science
at the Delft University of Technology,
to be defended publicly on Monday April 26th 2021, at 14:30h.

Student number:	5023602	
Project duration:	September 1 2020 - April 12 2021	
Thesis committee:	Prof. dr. S. D. C. Wehner,	TU Delft, supervisor
	Dr. J. Borregaard,	TU Delft
	Dr. M. T. Wimmer,	TU Delft
Daily Supervisors:	PhD candidate A. G. Iñesta,	TU Delft
	Dr. A. Dahlberg	

Abstract

Preparation of multi-partite entangled quantum states under realistic experimental conditions invariably results in states with non-unit fidelity to the target state. Purification protocols address the need for higher fidelity states than what can be directly prepared. These protocols consume several noisy input states and return an output state of higher fidelity, succeeding probabilistically. We introduce a recurrence based purification protocol for two-colorable graph states on d-dimensional quantum systems (qudits). We analyze the performance of the protocol in terms of the minimal required fidelity of input states as well as the expected number of attempts required to successfully reach a specific target fidelity. We find that not only is the purification regime larger for states of greater qudit dimension, but the expected number of attempts to successfully purify a state may be orders of magnitude lower. We develop error thresholds for the protocol with faulty two-qudit operations using a general uncorrelated error model and study the dependence on system dimension and state node number. We observe that the gate error threshold of the protocol improves with increasing dimension and moreover that the threshold depends on the degree of the graph but is otherwise independent of the number of nodes. The qualitative behaviour of the error threshold is captured by an analytically solvable model in which a restricted class of errors is considered. The error thresholds determined here may serve as one benchmark of assessing whether future experimental implementations of two qudit operations function well enough to realize a practical advantage of replacing qubit with qudit states in a multi-partite quantum information protocol.

Acknowledgements

Many people have supported me in the undertaking of this project. This section is intended to express my gratitude to them.

First and foremost, I would like to thank my supervisor, Prof. Stephanie Wehner, for the opportunity to conduct my thesis in her group and for teaching me to think adversarially. To both of my daily supervisors, Álvaro and Axel, thank you for the excellent feedback and the very helpful discussions. In particular, Álvaro thank you for teaching me a great deal about communicating results and for scouring my thesis completely. Thank you Helena, for your help with all the administrative aspects of this project. I would also like to thank the rest of the group for making me feel welcome.
I would like to give special thanks to Prof. Borregaard and Prof. Wimmer for kindly accepting the invitation to join my thesis committee and for taking the time to read this thesis.

I would like to thank my family for always encouraging me to follow my interests, and trusting me as I trek this winding road. Especially thank you to Aunt Joanne and Uncle Peter for supporting me throughout each step of my academic journey, I am extremely grateful. To my wonderful sister Sky, thank you for being my team mate and best friend. I really value all the times we've spent laughing and venting over video call these two years.

To my friends, thank you for showing me your worlds and bringing warmth and sunshine to even the most blustery of days. Joey, thank you for always listening to what I have to say, and even more so for your wonderful stories. Brennan, I value facing down each new day with you. Thank you for exploring with me and for making our two solo endeavours feel like proper teamwork.

This thesis has been financially supported by the QuTech Academy Scholarship 2019-2021. I would like to conclude by expressing my gratitude towards QuTech.

Contents

1

Introduction

Essentially every task in the realms of quantum communication and fault tolerant quantum computation rely upon the preparation and possible distribution of entangled quantum states. In general though, these states cannot be prepared perfectly, meaning they have non unital fidelity to the target state. In addition, quantum states are subject to decoherence and noise processes, resulting in further decrease of the fidelity over time. Purification protocols are procedures which can allow for high fidelity states to be prepared from a large number of lower fidelity initial states, at the cost of outputting only a fraction of the number of input states. For multi-partite quantum states, purification needs to be targeted towards a specific class of input states, because multi-partite entangled quantum states can be divided into non-equivalent categories of entanglement structure [1]. Transformation between entanglement categories using (possibly stochastic) local operations and classical communication is not possible. One fundamentally interesting class of multi-partite quantum states are called *graph states* – so named because each N-partite graph state has a direct correspondence with some mathematical graph with N vertices. Within the description of graph states, there is a category called two-colorable graph states (TCGS), which correspond to mathematical graphs which are two-colorable. Because they have a more rigid description than general graph states, TCGS are simpler to treat mathematically, but already many applications that make use of graph states only require TCGS. In the context of multiparty quantum communication, several proposals for quantum secret sharing [2, 3], which is an interesting protocol in it's own right that also constitutes a primitive for secure multi-party computation, use a type of TCGS called *GHZ type states* as a resource. With regards to fault tolerant quantum computation, TCGS are important both in *one way quantum compuation* and in the more mainstream *circuit model*. For one way computation, a type of TCGS known as a *cluster state* has been proven to be a universal resource [4], [5]. In order to achieve fault tolerance in the circuit model for quantum computation, it is necessary to consider encoding information vital to the computation using quantum error correcting codes [6]. Any quantum error

correcting code that is based on stabilizers can be seen also as a graph code[1] and the codewords of stabilizer codes are graph states [9]. Certain stabilizer codes have codewords that are in fact TCGS, for example every *CSS code* [9].

To date, the vast majority of research in the fields of quantum communication, computation, and information have focused on two level quantum systems, called qubits[2]. There is however mounting evidence suggesting that there are potential advantages to considering higher dimensional quantum systems, called qudits[3]. The most direct avenue in which qudits present an advantage is in terms of their information and communication capacity; specifically, $\log_2(d)$ qubits are required to encode the same amount of information that a single d dimensional qudit can encode [10]. Of a different vein, theoretical research into fault tolerant quantum computing with qudit systems has suggested, among other promising results, that higher error thresholds may be achievable for popular quantum error correcting codes [11, 12], that codes with the rare yet desirable property of a transversal non-Clifford gate can be constructed [13, 14], and that the circuit complexity of computations can be reduced [15, 16]. With regards to fundamentals of quantum information, there is experimental evidence that qudit quantum states are more robust to noise than their qubit counterparts, and that the heightened noise tolerance improves with increasing dimension. In [17] the authors tested the robustness of qubit and qudit bi-partite entangled states to tunable environmental noise by completing entanglement witness testing to determine the error threshold for which states were no longer entangled; they found that the error thresholds improved with dimension.

Many traditional qubit platforms allow encoding of higher dimensional systems, including neutral atoms [18], superconducting circuits [19], trapped ions [20] and photonic systems [21]. The state of the art in terms of experimental demonstrations of high dimensional multi-partite entangled states is currently for photons using either orbital angular momentum or time/frequency degrees of freedom [21, 22, 23]. In [22] the authors create a genuinely multi-partite entangled 3-qudit GHZ type state with dimension $d = 3$. In [23] the authors create genuinely multi-partite entangled 4-partite cluster states with dimension $d = 3$. The authors of [22] explain that the primary technical challenge in creating multi-partite entangled states in higher dimensions has been obtaining experimental realizations of the generalized CNOT gate. Getting around this challenge may require unconventional experimental design

[1] The correspondence between stabilizer codes and graph codes is valid in consideration of quantum systems where the dimension is a prime power [7, 8].

[2] Qubit stands for quantum bit.

[3] Qudit stands for quantum digit. This term refers to the fact that a d dimensional qudit has d orthogonal basis states, each of which can be used as a letter or digit in a computational or cryptographic alphabet.

such as the reliance by the authors of [22] on an in-house designed computer program [24] to search for arrangements of optical components capable of preparing a high dimensional multi-partite entangled state in the orbital angular momentum degree of freedom of photons.

In this work we present a new purification protocol for qudit TCGS, and we investigate whether the performance of the protocol with states of various qudit dimensions promises advantages compared to the qubit case. Direct comparisons cannot be made between protocols on different dimensional systems, due to potentially meaningful changes in experimental implementation of operations. Nevertheless, favorable dimension dependent scaling of performance metrics can constitute a positive indicator that working with higher dimensional systems could be beneficial. The protocol we present is restricted to qudit systems of prime dimension, a choice that takes advantage of the particularly simple mathematical structure available in describing qudit graph states of prime dimension. Here we primarily focus on relatively low qudit dimensions, such as $3, 5, 7, 11$; in the analytic analysis of Section 7.1 we take a look also at higher prime dimensions, up to and including 97. Consideration of quantum states with each of these dimensions is justified since single qudits can be achieved and coherently manipulated using qudit platforms relying on one or more of the various photonic degrees of freedom [21].
We address the following research questions:

> Can we extend the recurrence based purification protocol of [25] for qubit TCGS to a protocol that works for states where the underlying quantum systems are qudits of any prime dimension?

> How does the performance of the error-less purification protocol, as quantified by achievable output fidelities, the size of the purification regime and the expected number of attempts required to purify noisy input states to a given target fidelity depend on the qudit dimension and the number of nodes of the TCGS?

> How does the error tolerance of the purification protocol with faulty two-qudit operations depend on the the qudit dimension and the number of nodes of the TCGS?

1.1. Outline and contributions

The structure of this thesis is the following,

- In Chapter 2 we present the mathematical preliminaries necessary to describe both qudit systems and error processes in quantum mechanics.

- Chapter 3 provides a brief review of quantum state purification protocols, with a focus on recurrence type purification.
- Chapter 4 contains background on quantum graph states where the underlying physical systems are qudits. We contribute several short mathematical results regarding the transformation of quantum graph states by qudit operators, and a procedure for transforming any input state to a form that is diagonal in the graph state basis.
- Chapter 5 details the main result of this work, which is a novel recurrence type purification protocol that applies to TCGS on qudit systems of prime dimension. In Section 5.1, we elaborate the two subroutines that comprise the purification scheme and in Section 5.2 we explain how the subroutines can be combined to achieve purification. Overall, this chapter provides an affirmative answer to the first research question.
- Chapter 6 deals with the performance analysis of the proposed purification protocol, for three classes of input states: binary-like states (Section 6.1), where errors in the state preparation are confined to one node subset of the target TCGS; a one-parameter family of fully mixed states (Section 6.2); and depolarized states (Section 6.3), where each qudit of a TCGS is subject to depolarizing noise. For each class of states we study how increasing dimension and node numbers of the input states impacts the performance of the protocol, and we present models to explain the observed scaling relations. Overall we demonstrate explicitly that the error-less protocol effectively purifies each class of input states considered and that the efficacy of purification improves with qudit dimension in each case. The physical models we explore provide motivation that the protocol remains effective, especially for higher dimensions, on classes of input states not explicitly investigated here. This chapter constitutes a thorough investigation of the second research question.
- In Chapter 7 we demonstrate the performance of the protocol when all two-qudit operations are subject to errors, by developing both analytic (Section 7.1) and numeric results (Section 7.2). Here we extensively address the third research question. We quantify the advantage of working with qudit systems of larger dimension in terms of improvements in the gate error threshold, which can be of the magnitude of several percent between dimensions.

2

Mathematical preliminaries

In quantum mechanics unitary operators play a large role because they describe reversible transformations which preserve the norm of quantum states [6]. The spectral theorem for unitary matrices expounds several points that are useful for characterizing unitary operators; it is important in quantum mechanics because it provides the groundwork for constructing a basis in which quantum states can be written.

Theorem 2.1. [26] *Spectral theorem for unitary matrices:*
For a unitary matrix,

(a) All eigenvalues have absolute value 1.

(b) Eigenvectors corresponding to distinct eigenvalues are orthogonal.

(c) There is an orthogonal basis of the whole space, consisting of eigenvectors.

2.1. Operations on qudits

In order to work with individual quantum systems of dimension $d > 2$, known as quantum digits or qudits, it is necessary to introduce appropriate generalizations of the mathematical structure familiar from the study of qubits. A full representation of the state of a qubit is possible on a complex Hilbert space of dimension 2, which is a constituent of $\mathbb{C}^2$. All possible single qubit unitary operations can be generated by the Pauli group[1], $\mathcal{P}$ [6], which is the 16 element matrix group consisting of the 2×2 identity matrix, the matrices

$$\sigma_X = \begin{bmatrix} 0 & 1 \\ 1 & 0 \end{bmatrix}, \ \sigma_Z = \begin{bmatrix} 1 & 0 \\ 0 & -1 \end{bmatrix}, \ \sigma_Y = \begin{bmatrix} 0 & -i \\ i & 0 \end{bmatrix}, \tag{2.1.1}$$

and all unique products thereof, with the scalar factors ± 1, $\pm i$. The Pauli group itself is generated by the three Pauli matrices[2], $\langle \sigma_X, \ \sigma_Z, \ \sigma_Y \rangle$.

[1] Explicitly, $\mathcal{P} = \{\pm\mathbb{1}, \pm i\mathbb{1}, , \pm\sigma_X, \pm i\sigma_X, \pm\sigma_Z, \pm i\sigma_Z, \pm\sigma_Y, \pm i\sigma_Y\}$

[2] The angled brackets are not to be confused with expectation values in quantum mechanics. In this work $\langle\cdot\rangle$ refers only to the generator of a group.

In order to obtain an equally powerful formalism for understanding single qudit operations, it is possible to generalize the Pauli group, and introduce the related discrete Weyl group. In doing so, we mainly follow [27]. For further information, see [28, 8, 9].

2.1.1. The generalized Pauli group

The Hilbert space of a single d-dimensional quantum system, $\mathcal{H}_d$, is a constituent of $\mathbb{C}^d$. Label the computational basis for $\mathcal{H}_d$ by $\{|0\rangle, |1\rangle, \cdots, |d-1\rangle\}$. The shift operator, X, and the phase operator, Z, are an analog of the Pauli matrices σ_X and σ_Z [28]. These operators are defined as,

$$X = \sum_{j=0}^{d-1} |j \oplus 1\rangle \langle j| , \tag{2.1.2}$$

$$Z = \sum_{j=0}^{d-1} \omega^j |j\rangle \langle j| . \tag{2.1.3}$$

Throughout this work, define ω to be the first *d-th* primitive root of unity, $\omega := e^{\frac{2\pi i}{d}}$. In the above definition, $\oplus$ denotes addition modulo the dimension, d. The most glaring thing to notice about the shift and phase operator is that they are both unitary, but for $d > 2$ neither is Hermitian. As a consequence of unitarity (Theorem 2.1, [26]), they each possess orthogonal eigenspaces and all eigenvalues are of the form ω^j for some $j \in \mathbb{Z}_d$; hence they may still be interpreted as physical observables [29], and measurement outcomes can be labelled by their complex eigenvalues. The Hermitian conjugates of X and Z are given by X^{d-1} and Z^{d-1} respectively. For proper bookkeeping in d dimensions, it is important to note that there are differences between the cases of even and odd dimensions. To present a unified treatment, introduce $\tau = (-1)^d e^{\frac{i\pi}{d}} = e^{i\pi\frac{(d^2+1)}{d}}$, and notice that $\tau^2 = \omega$. Allow D to denote the order of τ, meaning that D is the lowest number such that $\tau^D = 1$. In the case of d even, then $D = 2d$, whereas in the case d is odd, $D = d$ directly. The analog of the third Pauli operator σ_Y can be constructed as $Y = \tau X^\dagger Z^\dagger = \tau X^{d-1} Z^{d-1}$, in order to preserve the commutation relation $XYZ = \tau \mathbb{1}$ from the qubit case ($\tau = i$ when $d = 2$). The generalized Pauli group, $\mathcal{P}_{d,N}$, where N is the number of qudits, is generated by the shift, phase, and Y operators, $\langle X, Z, Y\rangle$. From the action of the shift and phase operator on the basis vectors, it is simple to verify the following commutation relation,

$$Z^a X^b = \tau^{2ab} X^b Z^a. \tag{2.1.4}$$

For a register of N qudits, the associated Hilbert space, $\mathcal{H}_{d,N}$ is $(\mathbb{C}^d)^{\otimes N}$ and the computational basis vectors are $|\boldsymbol{q}\rangle = |q_1, q_2, \cdots, q_N\rangle = |q_1\rangle \otimes |q_2\rangle \otimes \cdots \otimes |q_N\rangle$, where each $q_i \in \mathbb{Z}_d$. The elements of the generalized Pauli group for an N qudit

register or quantum state are all possible N fold tensor products of the operators from a single copy of the group. A generating set for the group is given by

$$\begin{aligned}\langle X \otimes \mathbb{1}^{\otimes(N-1)},\ \mathbb{1} \otimes X \otimes \mathbb{1}^{\otimes(N-2)}, \cdots,\ \mathbb{1}^{\otimes(N-1)} \otimes X,\\ Z \otimes \mathbb{1}^{\otimes(N-1)},\ \mathbb{1} \otimes Z \otimes \mathbb{1}^{\otimes(N-2)}, \cdots,\ \mathbb{1}^{\otimes(N-1)} \otimes Z,\\ Y \otimes \mathbb{1}^{\otimes(N-1)},\ \mathbb{1} \otimes Y \otimes \mathbb{1}^{\otimes(N-2)}, \cdots,\ \mathbb{1}^{\otimes(N-1)} \otimes Y\rangle.\end{aligned}$$

2.1.2. The Clifford group

The Clifford group is the natural symmetry group of the (generalized) Pauli group, meaning that it consists of all unitaries which map Pauli operators to Pauli operators [27]. That is, a unitary operator U_C is a Clifford operator if for any Pauli operator $P \in \mathcal{P}_{d,N}$ it holds that,

$$U_C P U_C^\dagger = P' \in \mathcal{P}_{d,N}. \tag{2.1.5}$$

For two states to be local Clifford equivalent means that one of the states can be transformed into the other by the action of local Clifford operations. The Clifford group is important to the study of graph states because many graph states are local Clifford equivalent to other interesting quantum states, such as stabilizer states (see Section 4.2).

An example of a Clifford operator is the generalized Hadamard [30] operator. For qudits of dimension d the operator is defined as,

$$H = \frac{1}{\sqrt{d}} \sum_{x,y=0}^{d-1} \omega^{xy} |x\rangle \langle y| . \tag{2.1.6}$$

That the Hadamard is a Clifford operator follows from the two relations,

$$HXH^\dagger = Z \tag{2.1.7}$$

$$HZH^\dagger = X^{(d-1)}, \tag{2.1.8}$$

which generalize the qubit relations and can be easily verified using Equations 2.1.6, 2.1.2 and 2.1.3.

2.1.3. The discrete Weyl group

A more complete[3] foundation for operations on N qudits is given by the discrete Weyl group. In the study of continuous variable systems with canonical coordinates[4][33], [31] all possible states of a system with N constituents may be represented in *phase space*, such that each state has a unique position in the $2N$-dimensional space.

[3] In the descriptive sense, not in the analysis sense.

[4] Canonical coordinates typically are given in terms of position and momentum [31] but more generally may be specified by any two canonically conjugate operators [32], meaning operators A and B which satisfy the relation $[A, B] = i\mathbb{1}$.

Definition 2.1. (Symplectic form and vector space). Let V be an N-dimensional vector space over $\mathbb{R}$ and let $u : V \times V \mapsto \mathbb{R}$ be a bilinear map. Denote by V^* the dual space to V. If the map u is:

1. *skew-symmetric*: $u(\boldsymbol{s}, \boldsymbol{t}) = -u(\boldsymbol{t}, \boldsymbol{s})$ for all $\boldsymbol{s},\ \boldsymbol{t} \in V$.
2. *non-degenerate*: u is non-degenerate if the linear map $\tilde{u} : V \mapsto V^*$ given by $\tilde{u}(\boldsymbol{s})(\boldsymbol{t}) = u(\boldsymbol{s}, \boldsymbol{t})$, for all $\boldsymbol{s}, \boldsymbol{t} \in V$, is a bijection.

then u is a symplectic form on V and (V, u) is a symplectic vector space [34].

The phase space is a *symplectic vector space*, defined in Definition 2.1. The coordinates in phase space of a system are given by the N canonical coordinate pairs of the constituents. A useful feature of this picture is that operators on states can be described purely in terms of the translations they induce in phase space. With the language of discrete Weyl systems, it is possible to give a phase space type of formulation to finite-dimensional systems.

In order to properly introduce the elements of the Weyl group, the *Weyl operators*, it is helpful to first equip the vector space $\mathbb{Z}^{2N}$ with the *standard symplectic scalar product*, given in the following definition.

Definition 2.2. (Standard symplectic scalar product). The standard symplectic scalar product $[\cdot, \cdot]$ is a symplectic form defined by,

$$[(\boldsymbol{s}, \boldsymbol{t}), (\boldsymbol{s}', \boldsymbol{t}')] := (\boldsymbol{s}, \boldsymbol{t}) \begin{bmatrix} \mathbf{0}_N & -\mathbb{1}_N \\ \mathbb{1}_N & \mathbf{0}_N \end{bmatrix} (\boldsymbol{s}', \boldsymbol{t}')^T = \boldsymbol{t} \cdot \boldsymbol{s}' - \boldsymbol{s} \cdot \boldsymbol{t}', \tag{2.1.9}$$

where $\boldsymbol{s}, \boldsymbol{t}, \boldsymbol{s}'$ and $\boldsymbol{t}' \in V$, with V an N-dimensional vector space over $\mathbb{R}$.

We will often replace the symplectic vector space $\left(\mathbb{Z}^{2N}, [\cdot, \cdot]\right)$ with the space $\left(\mathbb{Z}_D^{2N}, [\cdot, \cdot]\right)$, where it is helpful to recall that $D = d$ if d is odd, and $D = 2d$ in the case of even d. Notice that in the case of prime d, the base vector space $\mathbb{Z}_d$ is an isomorphically equivalent instance of the unique finite field of order d, $\mathbb{F}_d$.

Definition 2.3. (Weyl Operator). For a system of N qudits, fix any pair of multi-indices $\boldsymbol{x} = (\boldsymbol{s}, \boldsymbol{t}) \in \mathbb{Z}^{2N}$ and define the Weyl operator,

$$\begin{aligned} W_{\boldsymbol{x}} = W_{\boldsymbol{s},\boldsymbol{t}} &= \tau^{-\boldsymbol{s}\cdot\boldsymbol{t}} (Z^{s_1} X^{t_1}) \otimes (Z^{s_2} X^{t_2}) \otimes \cdots \otimes (Z^{s_N} X^{t_N}) \\ &= \tau^{-\boldsymbol{s}\cdot\boldsymbol{t}} Z^{\boldsymbol{s}} X^{\boldsymbol{t}}. \end{aligned} \tag{2.1.10}$$

The notation $Z^{\boldsymbol{s}} X^{\boldsymbol{t}}$ is a short hand for $(Z^{s_1} X^{t_1}) \otimes (Z^{s_2} X^{t_2}) \otimes \cdots \otimes (Z^{s_N} X^{t_N})$. Each Weyl operator is an element of the generalized Pauli group on N constituents, and conversely every element of the generalized Pauli group is a Weyl operator, up to a phase that is a power of τ.

Notice that each Weyl operator $W_{\boldsymbol{x}}$ is described entirely by the vector $\boldsymbol{x} \in \mathbb{Z}^{2N}$. This means that the operators can be specified in the phase space picture solely by the vectors $\boldsymbol{x}$. It is also useful to note that it follows from the definition of the Clifford group that Weyl operators remain Weyl operators under Clifford operations. Let U_C be a Clifford operator and $W_{\boldsymbol{x}}$ a Weyl operator. Then,

$$U_C W_{\boldsymbol{x}} U_C^\dagger = W_{\boldsymbol{x}'}, \text{ for some } \boldsymbol{x}' \in \mathbb{Z}^{2N}. \tag{2.1.11}$$

Before introducing more properties of the Weyl operators, a preliminary to the commutation relations can be stated, which is a consequence of equation 2.1.4,

$$W_{\boldsymbol{v}+\boldsymbol{w}} = \tau^{[\boldsymbol{v},\boldsymbol{w}]} W_{\boldsymbol{v}} W_{\boldsymbol{w}}, \tag{2.1.12}$$

where $\boldsymbol{v} = (\boldsymbol{v}_1, \boldsymbol{v}_2),\ \boldsymbol{w} = (\boldsymbol{w}_1, \boldsymbol{w}_2) \in \mathbb{Z}^{2N}$.

Proof.

$$\begin{aligned} W_{\boldsymbol{v}+\boldsymbol{w}} &= \tau^{-(\boldsymbol{v}_1+\boldsymbol{w}_1)\cdot(\boldsymbol{v}_2+\boldsymbol{w}_2)} Z^{\boldsymbol{v}_1+\boldsymbol{w}_1} X^{\boldsymbol{v}_2+\boldsymbol{w}_2} \\ &= \tau^{-(\boldsymbol{v}_1\cdot\boldsymbol{v}_2+\boldsymbol{w}_1\cdot\boldsymbol{w}_2+\boldsymbol{v}_1\cdot\boldsymbol{w}_2+\boldsymbol{v}_2\cdot\boldsymbol{w}_1)} \tau^{2(\boldsymbol{w}_1\cdot\boldsymbol{v}_2)} \left(Z^{\boldsymbol{v}_1} X^{\boldsymbol{v}_2}\right)\left(Z^{\boldsymbol{w}_1} X^{\boldsymbol{w}_2}\right) \\ &= \tau^{\boldsymbol{v}_2\cdot\boldsymbol{w}_1 - \boldsymbol{w}_2\cdot\boldsymbol{v}_1} \tau^{-\boldsymbol{v}_1\boldsymbol{v}_2} \tau^{-\boldsymbol{w}_1\boldsymbol{w}_2} \left(Z^{\boldsymbol{v}_1} X^{\boldsymbol{v}_2}\right)\left(Z^{\boldsymbol{w}_1} X^{\boldsymbol{w}_2}\right) \\ &= \tau^{[\boldsymbol{v},\boldsymbol{w}]} W_{\boldsymbol{v}} W_{\boldsymbol{w}}. \end{aligned}$$

□

The commutation relations as well as other nice properties of the Weyl operators are collected in Lemma 2.1, which was originally stated in [28]. A short proof is given in Appendix A for the purpose of demonstrating that these properties follow from those already established.

Lemma 2.1. [28] For any two Weyl operators $W_{\boldsymbol{v}}$ and $W_{\boldsymbol{w}}$ with $\boldsymbol{v}, \boldsymbol{w} \in \mathbb{Z}^{2N}$ the following properties hold:

(i) $W_{\boldsymbol{v}} W_{\boldsymbol{w}} = \tau^{2[\boldsymbol{w},\boldsymbol{v}]} W_{\boldsymbol{w}} W_{\boldsymbol{v}} = \omega^{[\boldsymbol{w},\boldsymbol{v}]} W_{\boldsymbol{w}} W_{\boldsymbol{v}}$, these are the commutation relations for Weyl operators.

(ii) $\left[W_{\boldsymbol{v}}, W_{\boldsymbol{w}}\right] = 0$ if and only if $[\boldsymbol{v}, \boldsymbol{w}] = 0 \bmod d$. This is a corollary of (i).

(iii) $W_{\boldsymbol{v}}^t = W_{t\boldsymbol{v}}$ for $t \in \mathbb{Z}$. In particular, $W_{\boldsymbol{v}}^\dagger = W_{-\boldsymbol{v}}$.

(iv) The order of $W_{\boldsymbol{v}}$ divides d.

It will also be particularly useful for the purposes of Section 4.3 to note that it is possible to use modular arithmetic with Weyl operators. This follows from Lemma 2.2, which was originally stated in [28]. A proof is provided in Appendix A.

Lemma 2.2. [28] For all $\boldsymbol{v}, \boldsymbol{w} \in \mathbb{Z}^{2N}$ we have $W_{\boldsymbol{v}} \propto W_{\boldsymbol{w}}$ if and only if $\boldsymbol{w} = \boldsymbol{v} + d \cdot \boldsymbol{x}$ for some $\boldsymbol{x} \in \mathbb{Z}^{2N}$, in which case

$$W_{\boldsymbol{w}} = (-1)^{(d+1)[\boldsymbol{x},\boldsymbol{v}]} W_{\boldsymbol{v}}. \tag{2.1.13}$$

In particular, $W_{\boldsymbol{w}} = W_{\boldsymbol{v}}$ if $\boldsymbol{w} = \boldsymbol{v} \bmod D$.

Recall that in two dimensions, the importance of the Pauli group is underpinned by the fact that the group generates all possible unitary operations on the Hilbert space, $\mathcal{H}_2$. In higher dimensions, the Weyl operators are similarly important because the re-scaled Weyl operators, $\{d^{\frac{N}{2}} W_{\boldsymbol{x}}\}$ for $\boldsymbol{x} \in \mathbb{Z}_d^{2N}$, form an orthonormal basis for the Hilbert space $\mathcal{H}_{d,N}$, where orthonormality is defined with respect to the Hilbert-Schmidt inner product $\langle \mathcal{A},\ \mathcal{B} \rangle = \mathrm{Tr}\big(\mathcal{A}^\dagger \mathcal{B}\big)$ [27]. As a consequence, any operator $\mathcal{B}$ on $\mathcal{H}_{d,N}$ can be expanded as

$$\mathcal{B} = d^{-\frac{N}{2}} \sum_{\boldsymbol{x}} c_{\mathcal{B}}(\boldsymbol{x}) W_{\boldsymbol{x}}, \tag{2.1.14}$$

where $\{c_{\mathcal{B}}(\boldsymbol{x})\}$ is a set of expansion coefficients and $\boldsymbol{x} \in \mathbb{Z}_d^{2N}$.

2.1.4. Construction of controlled two qudit operations

For quantum systems with dimension greater than two, there are multiple non-equivalent ways that a CNOT type of operation may be realized. An operation is a generalized CNOT if it is a two-qudit operation in which the state of the second qudit is changed from one basis state to another, according to the state of the first qudit. Several possible forms of generalized CNOT operations have been presented [35, 36, 30]. Here the focus is on the same two realizations of the CNOT as in [36]. These generalizations can be constructed from the phase and shift operators and may be characterized by their action on a general two qudit input state. First, we introduce the operator CX_d^+, which we will refer to as the controlled raising operation,

$$CX_d^+ \left|i\right\rangle \left|j\right\rangle \longmapsto \left|i\right\rangle \left|j \oplus i\right\rangle. \tag{2.1.15}$$

Note that this operator is unitary but not Hermitian. It's inverse is given by $(CX_d^+)^{d-1}$. As in the qubit case, this gate admits a decomposition in terms of the shift and phase matrices,

$$\begin{aligned} CX_d^+ &= \frac{1}{d}\Big(\left|0\right\rangle\left\langle 0\right| \otimes \mathbb{1} + \left|1\right\rangle\left\langle 1\right| \otimes X + \left|2\right\rangle\left\langle 2\right| \otimes X^2 + \cdots + \left|d-1\right\rangle\left\langle d-1\right| \otimes X^{d-1} \Big) \\ &= \frac{1}{d}\Big(\sum_{n=0}^{d-1} \left|n\right\rangle\left\langle n\right| \otimes X^n \Big) \\ &= \frac{1}{d}\Big(\sum_{n=0}^{d-1} [\sum_{m=0}^{d-1} \omega^{d-mn} Z^m] \otimes X^n \Big). \end{aligned} \tag{2.1.16}$$

As a second generalization of the qubit CNOT gate, we introduce the operator CX_d^-, which we will refer to as the controlled lowering operator,

$$CX_d^- \left|i\right\rangle \left|j\right\rangle \longmapsto \left|i\right\rangle \left|j \ominus i\right\rangle . \tag{2.1.17}$$

Note that $\ominus$ denotes subtraction modulo d. As for the controlled raise operation, the controlled lowering operator is unitary but not Hermitian. It's inverse is given by $(CX_d^-)^{d-1}$. The decomposition in terms of shift and phase matrices is as follows:

$$\begin{aligned} CX_d^- &= \frac{1}{d}\Big(\left|0\right\rangle\left\langle 0\right| \otimes \mathbb{1} + \left|1\right\rangle\left\langle 1\right| \otimes X^{d-1} + \left|2\right\rangle\left\langle 2\right| \otimes X^{d-2} + \cdots + \left|d-1\right\rangle\left\langle d-1\right| \otimes X^{1} \Big) \\ &= \frac{1}{d}\Big(\sum_{n=0}^{d-1} \left|n\right\rangle\left\langle n\right| \otimes X^{n\cdot(d-1)} \Big) \\ &= \frac{1}{d}\Big(\sum_{n=0}^{d-1} [\sum_{m=0}^{d-1} \omega^{d-mn} Z^m] \otimes X^{n\cdot(d-1)} \Big). \end{aligned} \tag{2.1.18}$$

In Chapter 3 these decompositions are used together with the relations in Section 4.3 in order to characterize the action of the operators CX_d^+ and CX_d^- on graph basis states.

2.2. Quantum channels

A large variety of processes affecting quantum states can be understood in terms of the quantum channel framework [37].

Definition 2.4. (Quantum Channel). A quantum channel is a process $\mathcal{E}(\cdot)$, which maps density operators to density operators. It has the following properties,

1. *Linearity*:
$$\mathcal{E}(\alpha\rho_1 + \beta\rho_2) = \alpha\rho_1 + \beta\rho_2, \tag{2.2.1}$$
for $\alpha, \beta \in \mathbb{C}$ and $\rho_1, \rho_2 \in \mathcal{H}_{d,N}$.

2. *Preserves Hermiticity*:
$$\rho = \rho^\dagger \text{ implies } \mathcal{E}(\rho) = \mathcal{E}(\rho^\dagger). \tag{2.2.2}$$

3. *Preserves positivity*:
$$\rho \geq 0 \text{ implies } \mathcal{E}(\rho) \geq 0, \tag{2.2.3}$$
where for an operator A the notation $A \geq 0$ means that A is positive semi-definite.

4. *Preserves trace*:
$$\mathrm{Tr}\Big(\mathcal{E}(\rho)\Big) = \mathrm{Tr}(\rho). \tag{2.2.4}$$

Furthermore, quantum channels are often called Completely Positive Trace Preserving (CPTP) maps. The qualifier "completely positive" means that the channel remains positive when it acts on a system which is only part of a larger system.

In analogy to the familiar notion of a classical communication channel, one example of a quantum channel is a system, such as an optical fiber, which is used to transport quantum information between a sender and receiver. The description of such a quantum channel includes information about errors that could possibly affect the quantum information over the course of transmission. In fact, this notion of quantum channel encapsulates situations beyond communication. An important example is the storage of a quantum system. Since quantum systems are subject to decoherence, due to coupling with an external environment [6], in general errors are incurred in the storage and later retrieval of a quantum state. In the most wide conception, quantum channels can describe any trace preserving process which affects a quantum state.

Whenever considering a quantum channel we will make use of an error model to specify the action of the channel on quantum states. To this end, we distinguish between two classes of errors, correlated and uncorrelated errors. Uncorrelated errors are noise processes which independently affect single qudits, which may be part of a larger state, and do not affect the rest of the qudits. This type of error model is especially useful when considering systems without short range local interactions between qudits, such as states composed of spatially distant qudits. In contrast, correlated errors are joint quantum operations acting on several qudits of a system, possibly relying on multiple ancilliary qudits. All errors can be grouped into one of these two classes. In this work we will consider only uncorrelated error models, and moreover we will be interested in two types of quantum channel: *depolarizing channels* and *shift error channels*. Since these processes act on qudits independently, it is possible to characterize them by their action on a single qudit.

2.2.1. Depolarizing channels

The usual formulation of a depolarizing channel describes a process whereby a single qudit of a quantum state is replaced by the maximally mixed state with some probability p. We can model this process [38] by writing the depolarizing quantum channel with parameter $p \in [0, 1]$, acting on qudit j as,

$$\mathcal{E}_j(\rho) = (1-p)\rho + p\frac{\mathbb{1}_j}{d} \otimes \mathrm{Tr}_j(\rho), \tag{2.2.5}$$

where Tr_j denotes the partial trace over qubit j. An equivalent formulation of a depolarizing channel describes a process whereby a quantum state is exposed to

white noise with probability q. In the qubit case [6], this formulation is also well known and is alternatively modelled by,

$$\mathcal{E}_j^{(d=2)}(\rho) = (1-q)\rho + \frac{q}{3}\big(\sigma_{X_j}\rho\sigma_{X_j} + \sigma_{X_j}\sigma_{Z_j}\rho\sigma_{X_j}\sigma_{Z_j} + \sigma_{Z_j}\rho\sigma_{Z_j}\big),$$

where $q = \frac{3}{4}p$. Note that the use of $\sigma_X\sigma_Z$ in the previous equation is equivalent to σ_Y.

Similarly in the d dimensional case it is possible to construct a quantum depolarizing channel in the d dimensional Hilbert space [38], using the action of the Weyl operators (Section 2.1.3) on a quantum state. This formulation of the depolarizing channel is preferable from the operational standpoint because it is written explicitly in terms of operators, and hence can be applied naturally to any specific quantum state. Define the standard basis vectors for $\mathbb{Z}_D^N$ by $\{\boldsymbol{e}_k\}$, $k \in \mathbb{Z}$. In this form the depolarizing quantum channel with parameter $q \in [0, \frac{d^2-1}{d^2}]$, acting on qudit j is

$$\mathcal{E}_j(\rho) = (1-q)\rho + \frac{q}{(d^2-1)}\sum_{\{m,n\}\setminus(0,0)} W_{(m\boldsymbol{e}_j, n\boldsymbol{e}_j)}\rho\big(W_{(m\boldsymbol{e}_j, n\boldsymbol{e}_j)}\big)^\dagger. \tag{2.2.6}$$

In the above reformulation of the depolarization channel, we changed from parameter p to q to quantify the level of noise in the channel; the two parameters are related as $q = \frac{(d^2-1)p}{d^2}$. From now on, in referring to the depolarization channel we will make use of the form in 2.2.6. The multi-partite state that results from sending each qudit of an N qudit quantum state ρ_0 through such a channel is,

$$\rho(q) = \mathcal{E}_1 \circ \mathcal{E}_2 \circ \cdots \circ \mathcal{E}_N(\rho_0). \tag{2.2.7}$$

Notice that $q = 0$ ($p = 0$) corresponds to perfect transmission, whereas $q = \frac{d^2-1}{d^2}$ ($p = 1$) corresponds to a completely depolarized state.

2.2.2. Shift error channels

The shift error channel is the higher dimensional generalization of the well known *bit flip channel* [6]. The shift error channel describes a process in which a quantum state remains unaffected with probability $(1-q)$, but is exposed to each of the possible $(d-1)$ shift type errors with probability $\frac{q}{d-1}$. Physically speaking, this model applies in the case that shift type errors are the dominant error mechanism. We can model this process by writing the shift error channel with parameter q, acting on qudit j as,

$$\begin{aligned}\mathcal{E}_j(\rho) &= (1-q)\rho + \frac{q}{d-1}\sum_{m=1}^{d-1} X_j^m\rho(X_j^m)^\dagger \\ &= (1-q)\rho + \frac{q}{d-1}\sum_{m=1}^{d-1} W_{(m\boldsymbol{e}_j,\boldsymbol{0})}\rho W_{(m\boldsymbol{e}_j,\boldsymbol{0})}^\dagger,\end{aligned} \tag{2.2.8}$$

where as before $\{\boldsymbol{e}_k\}$, $k \in \mathbb{Z}$ are the standard basis vectors of $\mathbb{Z}_D^N$. This error channel is useful for treating situations where we want to analytically study the effect of adding some noise to a process, since it is simpler to treat than the more general depolarizing noise. In Section 7.1 we will use this restricted model to analytically study the effect of imperfect two qudit local operations in a purification protocol.

3

Purification of quantum states

For many applications in quantum information science and quantum computing it is necessary for a group of independent and possibly spatially separated users to share a specific entangled quantum state, either as a resource state, or as an encoding of the information which a computation takes as input. In the well known case of quantum teleportation [39], the resource states are two copies of a bi-partite qubit state with perfect correlations between the two qubits, $|\Phi_{00}\rangle = \frac{1}{\sqrt{2}}(|00\rangle + |11\rangle)$, which is known as the Bell state $|\Phi_{00}\rangle$. In the field of quantum error correction, a tool necessary to achieve fault tolerant quantum computation, stabilizer codes [40] require the preparation of large multi-partite entangled states as codewords. No matter the application, a global characteristic of schemes that rely on resource states or encoded information is that the probability that the scheme succeeds, or even the result of the scheme, is tied to the quality of the resource states or the encoding of the information. In the ideal scenario, all the quantum states used during execution of a quantum application would perfectly match their description by the application. In reality, the physical states are subject to errors both during their preparation and throughout the time taken to execute the application. Preparation errors may for example be the cause of imperfect operations or faulty measurements in the lab where the state is prepared. Over the course of running the application, errors may be due to a coupling between the target systems and the environment, communication of quantum information through noisy channels, or once again faulty operations and measurements. Since in reality all applications currently interface with imperfect quantum states, it is necessary both to have a way of quantifying how well the physical realization reproduces the target state, as well as to have a method for systematically improving this overlap. One quantitative measure of the "closeness" of two quantum states is the *fidelity*, stated in Definition 3.1.

Definition 3.1. Let ρ, σ be density operators on two equal dimension Hilbert spaces $\mathcal{H}_1$, $\mathcal{H}_2$, that is $dim(\mathcal{H}_1) = dim(\mathcal{H}_2)$. The fidelity of states ρ and σ is

defined as

$$F(\rho,\sigma) = \left(Tr(\sqrt{\rho^{1/2}\sigma\rho^{1/2}})\right)^2. \tag{3.0.1}$$

In the special case where one of the two states is pure, $|\psi\rangle$, the fidelity can be written in a simpler manner,

$$F(|\psi\rangle, \rho) = \langle\psi|\,\rho\,|\psi\rangle\,. \tag{3.0.2}$$

In particular, throughout this work we will only need to make use of the fidelity between a pure state, which is the target state of the application, and a general state ρ, the physical state prepared for use in the application. As a quantifier for the distance between two quantum states the fidelity has several nice properties [6]. Here we list those that will be relevant to the discussion in this chapter and in Chapter 5:

1. *Fidelity is bounded*: $0 \leq F(\rho,\sigma) \leq 1$. If $\rho \neq \sigma$ then $F(\rho,\sigma) < 1$ and $\rho = \sigma \;\Rightarrow\; F(\rho,\sigma) = 1$. If $F(\rho,\sigma) = 0$, it implies that ρ and σ have support on orthogonal subspaces.

2. *Fidelity is Symmetric*: $F(\rho,\sigma) = F(\sigma,\rho)$.

3. *Fidelity is invariant under unitary transformations*: Let U be a unitary operator. Then,
$$F(U\rho U^\dagger, U\sigma U^\dagger) = F(\rho,\sigma).$$

4. *Monotonicity of the Fidelity*: Restrict $\mathcal{E}$ to be a trace-preserving quantum operation. Then,
$$F(\mathcal{E}[\rho], \mathcal{E}[\sigma]) \geq F(\rho,\sigma).$$

Properties one and two guarantee that the fidelity reproduces intuitive expectations of how a measure for the similarity of states should function. Namely property one specifies that if two states are identical, the fidelity is maximum; whereas if the two states have support only on orthogonal subspaces, then the fidelity attains its minimum; any non-identical states with support on the same subspace of basis functions have an intermediate fidelity. In complement property two guarantees that the measure of similarity does not depend on how the states are labelled, or on the order of the comparison. Armed with the fidelity for measuring the similarity between states, it is desirable also to have a method of increasing the similarity. Properties three and four guarantee that any operations which are unitary, or even simply trace-preserving, will not cause the fidelity to decrease. Hence these types of operations can be useful in a scheme aimed at improving the fidelity. As a final remark on the fidelity, note that there are many other measures by which the quality of a physically realized quantum state may be judged. Some of these other methods, such as the trace distance [6] are true mathematical distance measures,

while others are measures of the entanglement, such as the concurrence [41] and its multi-dimensional counterpart the D-concurrence [42]. In light of the large variety of existing measures, the motivation to focus on the fidelity is that it is not only theoretically simple to calculate, but also can typically be calculated in a straightforward method from experimental measurements (see for example Equation 1 in [43]). Moreover, in the presentation of experimental results, the fidelity achieved is typically the measure reported on, even for higher dimensional quantum systems, as in [22] and [44].

3.1. Purification protocols

Methods which have as their goal increasing the fidelity of physically realized states with respect to a specific target state are known as purification protocols. Typically, these protocols take as input many copies of a flawed quantum state with fidelity F to the target state and aim to output one copy of a state with increased fidelity $\widetilde{F} > F$. Primarily this work will be focused on recurrence type protocols. These consist of one or more subroutines, which are iteratively applied, taking always states output by the previous iteration as input. These subroutines rely on application of local operations, local measurements and classical communication of the measurement results. In each subroutine a post-selection condition is applied based on the observed measurement outcomes, resulting in probabilistic success of the routine. The number of successful iterations performed can be selected by the users of the protocol, in order to reach a targeted final fidelity and based on how efficiently the protocol is expected to work under the given experimental conditions (which may be only approximately known to the users). The other types of purification protocols of interest are hashing and breeding protocols, which succeed deterministically and operate on a large number N of input copies. These protocols are especially effective in the limit $N \to \infty$. There is also another kind of purification, called *filtering*, which applies to a single copy of a given state and depends on local measurements, succeeding probabilistically according to the measurement outcomes. Unfortunately filtering protocols are applicable only to a restricted class of input states, and cannot for example be used to increase the fidelity of any full rank mixed two qubit state [45].

Recurrence type protocols were first introduced for bi-partite qubit states, with Bell states as the target states [46, 47]. Following the introduction of these initial bi-partite protocols, recurrence type protocols were also introduced for various multi-partite input states (see Section 7 from [45] for a review which covers most possibilities), especially for target states within the class of graph states (introduced in Chapter 4) [25, 48].

All recurrence type protocols have a similar skeleton structure, and their effectiveness and conditions of applicability share some common characteristics. The setup and general structure is delineated in Box 1.

Box 1: Anatomy of purification: Recurrence Type Protocols.

The target state is a multi-partite entangled quantum state consisting of N qudits. There are N independent and possibly spatially separated users who wish to share a physical realization of the target state between them, with a fidelity $\widetilde{F}$ that is at least sufficient for their intended application. The users decide on the sequence of purification subroutines to use, and how many iterations are needed.

Setup: To begin the first subroutine, the N parties collaborate to prepare two copies of a noisy entangled state, with fidelity $F < \widetilde{F}$ to their target state. The two copies are usually considered to be identical, however results can also be stated for non-identical states, usually with the help of the quantum de Finetti theorem [49], [50]. Each of the N collaborators holds one qudit from each of the two noisy copies, so they each hold two qudits in total (Figure 3.1a) and are responsible for any operations or measurements on these systems.

To begin the **n**-th subroutine two states output by the subroutine **n-1** are retrieved from memory. Retrieval from memory is accomplished locally by the N parties, who each swap their two qudits belonging to the two states out of local quantum memories.

Phase 1: Copy information. Each participant independently performs local operations on their two qudits, which will include a controlled two-qudit gate (Figure 3.1b). The goal of the multi-lateral application of controlled two-qudit gates is to copy information from the first noisy state to the second.

Phase 2: Measure and read out information. The N participants measure their second qudit in the basis indicated by the subroutine, which in total means that the second noisy state is measured (Figure 3.1c). The outcomes of the local measurements provide information about the second copy of the state.

Phase 3: Post-select and declare success/failure. To determine whether success is achieved, the participants communicate their measurement results over a classical channel and apply a post selection condition, such that success if declared if the condition is met, or else failure is declared (Figure 3.1d). Whenever success is declared, then because of the selection condition the participants can be sure that the measurement results reveal information about the remaining noisy state. If failure is declared the subroutine is restarted when appropriate.

Continue to next subroutine or stop.

In quantum mechanics, learning information about a state is akin to decreasing the classical uncertainty about what the state is, which implies purification. Hence heuristically speaking each subroutine in a purification protocol can be seen as increasing the fidelity by way of extracting information about the noisy states, and selecting for instances where the information is useful in decreasing uncertainty.

As for the conditions of applicability, every recurrence type protocol requires that the input states meet at least some minimal fidelity, $F_{\min}$. If the input fidelity $F < F_{\min}$, then the protocol will not be able to achieve purification. In the case of perfect operation of the protocol (i.e. all operations, measurements and communication are ideal and noiseless), then any input state satisfying $F > F_{\min}$ converges towards a state with fidelity $\widetilde{F} = 1$, given sufficiently many applications of the purifying subroutines. In the more realistic case where noise is introduced into the protocol, there is also a maximum reachable fidelity, $F_{\max} < 1$. In general, recurrence protocols have a lower minimal fidelity $F_{\min}$ than hashing or breeding protocols, meaning that they can be applied to a wider range of input states. As a drawback however, in the presence of noise the maximal reachable fidelity, $F_{\max}$, is lower than the corresponding maximum achievable using a hashing or breeding protocol. In this way, recurrence and hashing or breeding protocols are complementary, in that for input states of low initial fidelity, recurrence type protocols may be used to purify until the fidelity is greater than the minimum for a hashing or breeding protocol, at which point these protocols may be used to complete the purification and reach a greater final fidelity [45].

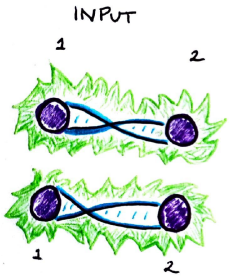

(a) Recurrence protocols take as input two copies of a noisy entangled state.

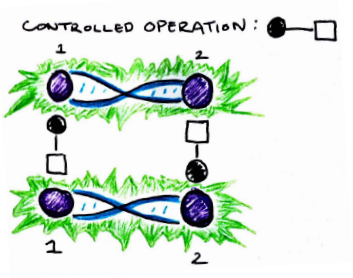

(b) In phase 1 information is copied from the second state to the first. The copying of information is facilitated by a sequence of local operations, including a controlled two-qudit operation.

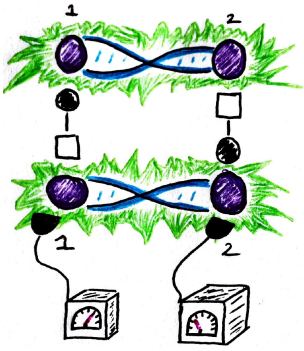

(c) In phase 2 the second state copy is measured.

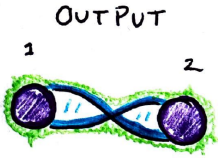

(d) In phase 3 it is determined whether the measurement results satisfy a post-selection condition. If so, the protocol is declared successful and the first state is kept. The output state is a less noisy version of the target entangled state.

Figure 3.1: Phases of a recurrence type purification protocol. Here we demonstrate with a noisy bi-partite entangled state (i.e. $N = 2$), but in general we consider N-partite states. The underlying physical systems (represented by the purple circles) are qudits of any dimension. Curved blue lines between qudits represent entanglement and green shapes surrounding states represent noise.

Definition 3.2 (Yield of a purification protocol)**.** The yield of a purification protocol is the ratio of the single purified state output by the protocol to the average number of input state copies consumed during purification.

Another important consideration is that an output state with unit fidelity, $\widetilde{F} = 1$ can only be achieved in the asymptotic limit, meaning a large number of subroutine iterations are necessary. In this limit however the yield of the protocol (Definition 3.2) vanishes. To see this intuitively, note that each successful subroutine has a yield of one half, and subroutines succeed only probabilistically. Hence as the number of iterations grow, the expected number of times a subroutine or chain of iterated subroutines must be repeated also grows. For these reasons, the yield is zero in the asymptotic regime. For completeness, an explicit calculation of the yield is demonstrated in Appendix B. Nevertheless, for any desired final fidelity within the purification regime accessible given a specific purification protocol and noise level, the target fidelity is achievable in a finite number of iterations and the overall process has a finite yield.

The main constraint on existing multi-partite recurrence protocols[1] is that they are restricted to working for states with qubits as the underlying physical systems. In contrast, in the case of bi-partite states, several works have presented purification protocols which are suitable for higher dimensional systems [35, 51, 52]. Another major constraint is that qubit multi-partite recurrence protocols require a very large expected number of attempts to successfully output states of reasonably high fidelity, essentially due to the low yield and success probabilities of each purification stage. To address these restrictions, a recurrence type protocol which has graph states on qudits of prime dimension as the target states is presented in Chapter 5 and constitutes the main result of this thesis. In Section 6.3 we demonstrate that for qudits of sufficiently high dimension, the proposed protocol requires a much lower expected number of attempts to successfully output states of reasonably high fidelity.

[1] Note that in [51] the authors propose a hashing type protocol for qudit GHZ-type states.

4

General dimension graph states

Consider a mathematical graph, G. Let V denote the set of vertices of the graph, E the set of edges and N the size of the set of vertices, $N := |V|$. A graph is called undirected if the edges do not have an orientation, meaning that if one was to trace their finger over the graph, they could choose in which direction to follow each edge. The graph may be fully specified by its adjacency matrix Γ, which is an $N \times N$ matrix with one row and column per vertex. The matrix entries Γ_{ij} encode the number of edges shared between vertices i and j. The matrix entry Γ_{ij} will of course be zero whenever vertices i and j do not share an edge. The degree of a vertex is the number of edges which terminate at that vertex. In terms of the adjacency matrix, the degree of vertex j is the number of non-zero entries in the the j^{th} row or column of the matrix. In this work the degree of the graph will be used as shorthand terminology to refer to the maximum degree of any vertex in the graph.

Very often we will focus specifically on two colorable graphs, which are graphs where the set of vertices can be split into a bi-partition of subsets V_A and V_B of sizes $N_A := |V_A|$ and $N_B := |V_B|$, such that there are no edges between vertices of one subset. As such, all edges of these graphs are between a vertex of V_A and another vertex of V_B. It is of interest to focus on two-colorable graphs because already many applications in quantum information processing and communication which require reference to mathematical graphs actually only require the specific class of two colorable graphs [9]. In reference to any two colorable graph we will assume that a suitable bi-partition has been made. For the sake of clarity, when numbering the veritces of a two-colorable graph we will always number the vertices of set V_A first, and those of set V_B second, unless otherwise indicated. The effect of this choice is that in the adjacency matrix of a two colorable graph the first N_A rows and columns will correspond to vertices of set V_A.

Now that we have introduced the relevant notation relating to mathematical graphs, we can shift attention to quantum graph states, each of which is essentially the quantum analog of a particular mathematical graph. This is to say that there is a surjective mapping from the set of all possible mathematical graphs on N vertices to the set of quantum graph states on N identical quantum systems, which may be d-dimensional. There are two ways to understand the correspondence between mathematical graphs and quantum graphs states, known as the *constructive formulation* and the *stabilizer formulation* [9]. In the constructive formulation a mathematical graph is used as a set of instructions for how to prepare a quantum graph state. In complement, in the stabilizer formulation the mathematical graph specifies a complete set of generators for the stabilizer group of the quantum graph state. Each of these formulations is expanded upon in the following sections.

4.1. Constructive formulation

A graph state on N vertices with adjacency matrix $\mathbf{\Gamma}$ can be built by first associating each vertex with a d dimensional qudit prepared in the state

$$|+\rangle := \frac{1}{\sqrt{d}} \sum_{j=0}^{d-1} |j\rangle \,. \tag{4.1.1}$$

Next, for each entry Γ_{ab} of the adjacency matrix, repeatedly perform the generalized CPHASE (G-CZ) gate, $C_z^{(a,b)}$, between the qudits labelled a and b, Γ_{ab} times. As in the qubit case the G-CZ gate is invariant with respect to swapping the control and target qudit. For this reason qudit graph states correspond to undirected graphs and we can choose to always write the G-CZ gate as,

$$\begin{aligned} C_z^{(a,b)} :&= \sum_{j=0}^{d-1} |j\rangle\langle j|_a \otimes Z_b^j \otimes \mathbb{1}_{V\setminus\{a,b\}} \\ &= \frac{1}{d} \sum_{j=0}^{d-1} \Big[\sum_{m=0}^{d-1} \omega^{d-jm} Z^m \Big]_a \otimes Z_b^j \otimes \mathbb{1}_{V\setminus\{a,b\}} \end{aligned} \tag{4.1.2}$$

Recall that the weighted edges of the graph are specified by the adjacency matrix, so that the edge between vertices a and b is given by Γ_{ab}. In the constructive formalism then, a graph state $|G\rangle$ is specified by

$$|G\rangle = \prod_{\substack{a,b\in V \\ a>b}} \big(C_z^{(a,b)}\big)^{\Gamma_{ab}} |+\rangle^{\otimes N} \,. \tag{4.1.3}$$

If one considers measuring a graph state, which can be done by choosing a basis and measuring each qudit in that basis, then it is useful to start by writing the graph state explicitly in the eigenbasis of the Z operator. For the sake of clarity, we

introduce the string of labels $\boldsymbol{q} \in \mathbb{F}_d^{\otimes N}$, i.e. $\boldsymbol{q} = (q_1,\ q_2,\ \cdots,\ q_N)$, where $q_i \in \mathbb{F}_d$. Denote by $\{\boldsymbol{e}_k\}$, $k \in \mathbb{Z}$, the standard basis vectors of $\mathbb{Z}^N$. With some algebra, Equations 4.1.1, 4.1.2 and 4.1.3 can be combined to re-express the graph state $|G\rangle$ in the phase basis,

$$|G\rangle = \frac{1}{d^{\frac{N}{2}}} \sum_{\boldsymbol{q}} \omega^{\sum\limits_{\{a,b \in V | a>b\}} \Gamma_{ab}(\boldsymbol{q}\cdot\boldsymbol{e}_a)(\boldsymbol{q}\cdot\boldsymbol{e}_b)} |\boldsymbol{q}\rangle\,. \tag{4.1.4}$$

4.2. Stabilizer formulation

A quantum stabilizer state on N d-dimensional quantum systems is a simultaneous $+1$ eigenstate of a commutative subgroup $\mathcal{S}$ of the Weyl group, which does not contain any multiples of the identity, except for $\mathbb{1}$ itself [8], [9]. For a stabilizer state to be uniquely defined (up to a global phase), it is necessary that the order of $\mathcal{S}$ is d^N. In the case that d is a prime number, $\mathcal{S}$ can be generated by only N operators [9], [7], called the *stabilizer generators*. In the case that d has multiple prime factors, then the number of generators is m, where $N \leq m \leq 2N$ [8]. The framework of stabilizer states is instrumental to the study of graph states because it has been proven that whenever d is a prime power i.e. $d = p^k$ for prime p and integer k, then any stabilizer state is local Clifford equivalent (Section 2.1.2) to a graph state, and conversely each graph state is local Clifford equivalent to a stabilizer state [7, 8]. Motivated by these known results, we will henceforth make the restriction to consider only prime dimensions (not prime powers), which will stand throughout the rest of this work. With this restriction in place, all graph states considered are also stabilizer states, and the stabilizer is generated by only N operators. One advantage of relating graph states to stabilizer states is that the known action of the stabilizer can be exploited to determine how other operators act on the states; this approach is explored in Section 4.3. Following from these considerations, a graph state can be viewed in terms of its stabilizer generators [9, 7]. For each vertex $v \in V$ there is an associated stabilizer generator [9],

$$g_v = X_v \prod_{w \in \mathcal{N}(v)} Z_w^{\Gamma_{vw}}, \tag{4.2.1}$$

where we have introduced the notation $\mathcal{N}(v)$ to denote the neighbors of vertex v, meaning all the vertices which share a weighted edge with v.

The stabilizer formulation can be linked to the constructive formulation in another way as well. It is possible to form a basis, called the graph state basis, for the d^N dimensional space in which $|G\rangle$ itself is a basis state. We will denote this basis $\{|\Psi_{\boldsymbol{\mu}}\rangle_G\}$ and label $|\Psi_{\mathbf{0}}\rangle_G := |\boldsymbol{G}\rangle$. If it is clear from context we will drop the label G and write instead $\{|\Psi_{\boldsymbol{\mu}}\rangle\}$ and $|\Psi_{\mathbf{0}}\rangle$. Like $|G\rangle$, elements of the graph state basis

are superposition states over all length N strings with values in $\mathbb{F}_d$. States in the basis are differentiated by the relative phases of the superposition. As shown in Section 4.1, the relative phases of components in the graph state itself are essentially determined by the adjacency matrix of the graph. Since only the relative phases change between different elements of the graph state basis, each element of the basis can be generated from $|G\rangle$ by appropriate application of the phase operators, Z^{μ_i}, on each qudit. That is, for every label $\boldsymbol{\mu} \in \mathbb{F}_d^{\otimes N}$ there is an element of the graph state basis generated from $|G\rangle$ according to

$$|\Psi_{\boldsymbol{\mu}}\rangle_G = Z_1^{\mu_1} \otimes \cdots \otimes Z_N^{\mu_N} |\Psi_{\mathbf{0}}\rangle_G \equiv W_{(\mathbf{0},\boldsymbol{\mu})} |\Psi_{\mathbf{0}}\rangle_G . \tag{4.2.2}$$

Since there are d^N of these states, it is only necessary to confirm orthogonality in order to prove that they are an orthogonal basis of the Hilbert space.

Consider the inner product of two states, $|\Psi_{\boldsymbol{\mu}_1}\rangle$ and $|\Psi_{\boldsymbol{\mu}_2}\rangle$, defined according to Equation 4.2.2 and a known graph G. The inner product is,

$$\langle\Psi_{\boldsymbol{\mu}_1}|\Psi_{\boldsymbol{\mu}_2}\rangle = \langle\Psi_{\mathbf{0}}| (Z^{\boldsymbol{\mu}_1})^\dagger Z^{\boldsymbol{\mu}_2} |\Psi_{\mathbf{0}}\rangle . \tag{4.2.3}$$

If $\boldsymbol{\mu}_1 = \boldsymbol{\mu}_2$ then Equation 4.2.3 is equal to 1. We focus on the case $\boldsymbol{\mu}_1 \neq \boldsymbol{\mu}_2$. Employing Equation 4.1.3, the sequence of operations $(Z^{\boldsymbol{\mu}_1})^\dagger Z^{\boldsymbol{\mu}_2} |\Psi_{\mathbf{0}}\rangle$ may be re-written,

$$(Z^{\boldsymbol{\mu}_1})^\dagger Z^{\boldsymbol{\mu}_2} |\Psi_{\mathbf{0}}\rangle = (Z^{\boldsymbol{\mu}_1})^\dagger Z^{\boldsymbol{\mu}_2} \mathcal{U} |+\rangle^{\otimes N} , \tag{4.2.4}$$

where we denote the the sequence of unitary operations $\prod_{\substack{a,b\in V \\ a>b}} \left(C_z^{(a,b)}\right)^{\Gamma_{ab}}$ by $\mathcal{U}$, since taken together they constitute a unitary process with Hermitian conjugate $\mathcal{U}^\dagger$. From Equation 4.1.2, we see that $\mathcal{U}$ commutes with $Z^{\boldsymbol{\nu}}\ \forall\ \boldsymbol{\nu} \in \mathbb{F}_d^{\otimes N}$, since each $\left(C_z^{(a,b)}\right)^{\Gamma_{ab}}$ can be written entirely in terms of identity and phase type operators on the N qudits. Equation 4.2.4 is equivalent to,

$$\begin{aligned} (Z^{\boldsymbol{\mu}_1})^\dagger Z^{\boldsymbol{\mu}_2} |\Psi_{\mathbf{0}}\rangle &= \mathcal{U}\ (Z^{\boldsymbol{\mu}_1})^\dagger Z^{\boldsymbol{\mu}_2} |+\rangle^{\otimes N} \\ &= \mathcal{U}\ Z^{\boldsymbol{\mu}_2+(d-1)\boldsymbol{\mu}_1} |+\rangle^{\otimes N} . \end{aligned} \tag{4.2.5}$$

Overall then,

$$\begin{aligned} \langle\Psi_{\boldsymbol{\mu}_1}|\Psi_{\boldsymbol{\mu}_2}\rangle &= \langle+|^{\otimes N}\ \mathcal{U}^\dagger\mathcal{U}\ Z^{\boldsymbol{\mu}_2+(d-1)\boldsymbol{\mu}_1} |+\rangle^{\otimes N} \\ &= \frac{1}{d^N} \sum_{\boldsymbol{k}} \langle\boldsymbol{k}|\ \mathbb{1}_N \left[\sum_{\boldsymbol{m}} \omega^{\boldsymbol{m}\cdot[\boldsymbol{\mu}_2+(d-1)\boldsymbol{\mu}_1]} |\boldsymbol{m}\rangle \langle\boldsymbol{m}|\right] \sum_{\boldsymbol{j}} |\boldsymbol{j}\rangle \\ &= \frac{1}{d^N} \sum_{\boldsymbol{m}} \omega^{\boldsymbol{m}\cdot[\boldsymbol{\mu}_2+(d-1)\boldsymbol{\mu}_1]} \sum_{\boldsymbol{k}} \sum_{\boldsymbol{j}} \delta_{\boldsymbol{k},\boldsymbol{m}}\delta_{\boldsymbol{m},\boldsymbol{j}} \\ &= 0. \end{aligned} \tag{4.2.6}$$

In the second line we used Equations 4.1.1 and 2.1.3, and in the final line we used that the sum over all powers of the roots of unity is equal to zero. Having confirmed the orthogonality, we conclude that the states $|\Psi_{\boldsymbol{\mu}}\rangle$ constitute a basis.

We focus on two-colorable graph states (TCGS) in this work, which are quantum graph states where the corresponding graph is two-colorable. Recall that for two-colorable graphs we chose the convention that all vertices from set V_A are numbered before those of set V_B, so that the first N_A rows and columns of the adjacency matrix are associated with the vertices in V_A. In light of these considerations, we introduce a modified notation for two-colorable graph basis states. If G is two-colorable, then $\boldsymbol{\mu} = (\boldsymbol{\mu}_A, \boldsymbol{\mu}_B)$, where $\boldsymbol{\mu}_A \in \mathbb{F}_d^{\otimes N_A}$ and $\boldsymbol{\mu}_B \in \mathbb{F}_d^{\otimes N_B}$, and the graph basis states are,

$$\{|\Psi_{\boldsymbol{\mu}}\rangle_G\} = \{|\Psi_{\boldsymbol{\mu}_A,\boldsymbol{\mu}_B}\rangle_G\}. \tag{4.2.7}$$

4.3. The graph state basis

As introduced in Section 4.2, the states $|\Psi_{\boldsymbol{\mu}}\rangle_G = W_{(\mathbf{0},\boldsymbol{\mu})}\,|\Psi_{\mathbf{0}}\rangle_G$ form a basis for the d^N dimensional quantum space, known as the graph state basis. For certain applications, such as purification protocols where the performance is evaluated based on the fidelity of the output state, it is useful to work explicitly in the graph state basis. For this reason we set about establishing some basic facts about how the basis states transform under the action of specific operators. The relations presented here are well known in the qubit case [25].

Proposition 4.1. The states $|\Psi_{\boldsymbol{\mu}}\rangle_G$ are eigenstates of the stabilizers presented in Equation 4.2.1,

$$\Big\{g_j = X_j \prod_{k\in\mathcal{N}(j)} Z_k^{\Gamma_{jk}}\Big\}\ \forall\ j \in V.$$

In particular, for every g_i, $|\Psi_{\boldsymbol{\mu}}\rangle_G$ is an eigenstate with eigenvalue $\omega^{-\mu_j}$.

Proof.
By definition, $g_j\,|\Psi_{\mathbf{0}}\rangle_G = |\Psi_{\mathbf{0}}\rangle_G$, $\forall\ j \in V$ and hence $W_{(\mathbf{0},\boldsymbol{\mu})}g_j\,|\Psi_{\mathbf{0}}\rangle_G = |\Psi_{\boldsymbol{\mu}}\rangle_G$. To determine $g_jW_{(\mathbf{0},\boldsymbol{\mu})}\,|\Psi_{\mathbf{0}}\rangle_G$ it is useful to evaluate the full set of commutation relations $\big[g_j, W_{(\mathbf{0},\boldsymbol{\mu})}\big]\ \forall\ j \in V$. First, define $\boldsymbol{\Gamma}_j$ to be the $j-th$ row of the adjacency matrix $\boldsymbol{\Gamma}$ and $\boldsymbol{e}_j$ to be the $j-th$ standard basis vector of $\mathbb{Z}^N$. The stabilizers can then be re-written as a Weyl operator, using Definition 2.3, $g_j = \tau^{\boldsymbol{e}_j\cdot\boldsymbol{\Gamma}_j}W_{(\boldsymbol{e}_j,\boldsymbol{\Gamma}_j)}$. Using the commutation relations from Lemma 2.1, it then holds automatically that,

$$\begin{aligned} g_jW_{(\mathbf{0},\boldsymbol{\mu})} &= \tau^{\boldsymbol{e}_j\cdot\boldsymbol{\Gamma}_j}\ W_{(\boldsymbol{e}_j,\boldsymbol{\Gamma}_j)}W_{(\mathbf{0},\boldsymbol{\mu})} \\ &= \omega^{[(\boldsymbol{e}_j,\boldsymbol{\Gamma}_j),(\mathbf{0},\boldsymbol{\mu})]}\ W_{(\mathbf{0},\boldsymbol{\mu})}\tau^{\boldsymbol{e}_j\cdot\boldsymbol{\Gamma}_j}W_{(\boldsymbol{e}_j,\boldsymbol{\Gamma}_j)} \\ &= \omega^{-\boldsymbol{e}_j\cdot\boldsymbol{\mu}}\ W_{(\mathbf{0},\boldsymbol{\mu})}g_j \end{aligned} \tag{4.3.1}$$

Overall then, the commutation relations are,

$$g_j W_{(\mathbf{0},\boldsymbol{\mu})} = \omega^{-\mu_j}\ W_{(\mathbf{0},\boldsymbol{\mu})} g_j. \tag{4.3.2}$$

Therefore, the state $|\Psi_{\boldsymbol{\mu}}\rangle_G$ is an eigenstate of each g_j, with corresponding eigenvalue $\omega^{-\mu_j}$,

$$g_j |\Psi_{\boldsymbol{\mu}}\rangle_G = \omega^{-\mu_j} W_{(\mathbf{0},\boldsymbol{\mu})} g_j |\Psi_{\mathbf{0}}\rangle_G = \omega^{-\mu_j} |\Psi_{\boldsymbol{\mu}}\rangle_G . \tag{4.3.3}$$

□

Proposition 4.2. The action of a phase type operator Z on qudit j of an N qudit graph state is given by

$$Z_j |\Psi_{\boldsymbol{\mu}}\rangle_G = \left|\Psi_{\boldsymbol{\mu}+\boldsymbol{e}_j}\right\rangle_G . \tag{4.3.4}$$

It follows by repeated action of Z_j that the action of powers of phase type operators is given by,

$$Z_j^m |\Psi_{\boldsymbol{\mu}}\rangle_G = \left|\Psi_{\boldsymbol{\mu}+m\boldsymbol{e}_j}\right\rangle_G ,\ \forall\ m \in \mathbb{Z}_d. \tag{4.3.5}$$

Proof.

$$\begin{aligned} Z_j |\Psi_{\boldsymbol{\mu}}\rangle_G &= W_{(\mathbf{0},\boldsymbol{e}_j)} W_{(\mathbf{0},\boldsymbol{\mu})} |\Psi_{\mathbf{0}}\rangle_G \\ &= W_{(\mathbf{0},\boldsymbol{\mu}+\boldsymbol{e}_j)} |\Psi_{\mathbf{0}}\rangle_G \\ &= \left|\Psi_{\boldsymbol{\mu}+\boldsymbol{e}_j}\right\rangle_G \end{aligned} \tag{4.3.6}$$

□

Proposition 4.3. The action of a shift type operator X on qudit j of an N qudit graph state is given by

$$X_j |\Psi_{\boldsymbol{\mu}}\rangle_G = \omega^{\mu_j(d-1)} \left|\Psi_{\boldsymbol{\mu}+(d-1)\boldsymbol{\Gamma}_j}\right\rangle_G . \tag{4.3.7}$$

It follows by repeated action of X_j that the action of powers of shift type operators is given by,

$$X_j^m |\Psi_{\boldsymbol{\mu}}\rangle_G = \omega^{m\left(\mu_j(d-1)\right)} \left|\Psi_{\boldsymbol{\mu}+m(d-1)\boldsymbol{\Gamma}_j}\right\rangle_G \ \forall\ m \in \mathbb{Z}_d. \tag{4.3.8}$$

Proof.
The transformation is actually simplest when the $d-1$ power of the shift operator is applied, so this is considered first,

$$\begin{aligned} X_j^{d-1} |\Psi_{\boldsymbol{\mu}}\rangle_G &= \omega^{\mu_j} X_j^{d-1} g_j |\Psi_{\boldsymbol{\mu}}\rangle_G \\ &= \omega^{\mu_j}\ W_{((d-1)\boldsymbol{e}_j,\mathbf{0})}\ \tau^{\boldsymbol{e}_j\cdot\boldsymbol{\Gamma}_j}\ W_{(\boldsymbol{e}_j,\boldsymbol{\Gamma}_j)} W_{(\mathbf{0},\boldsymbol{\mu})} |\Psi_{\mathbf{0}}\rangle_G \\ &= \omega^{\mu_j} W_{(\mathbf{0},\boldsymbol{\Gamma}_j)} W_{(\mathbf{0},\boldsymbol{\mu})} |\Psi_{\mathbf{0}}\rangle_G \\ &= \omega^{\mu_j} W_{(\mathbf{0},\boldsymbol{\mu}+\boldsymbol{\Gamma}_j)} |\Psi_{\mathbf{0}}\rangle_G \\ &= \omega^{\mu_j} \left|\Psi_{\boldsymbol{\mu}+\boldsymbol{\Gamma}_j}\right\rangle_G . \end{aligned} \tag{4.3.9}$$

Following a similar derivation, the action of the shift operator on a graph basis state can be calculated by repeatedly invoking the stabilizer operator eigenvalue equations,

$$\begin{aligned} X_j \left|\Psi_{\boldsymbol{\mu}}\right\rangle_G &= \omega^{\mu_j(d-1)} X_j g_j^{d-1} \left|\Psi_{\boldsymbol{\mu}}\right\rangle_G \\ &= \omega^{\mu_j(d-1)} X_j^{1+d-1} W_{(\mathbf{0},(d-1)\boldsymbol{\Gamma}_j)} W_{(\mathbf{0},\boldsymbol{\mu})} \left|\Psi_{\mathbf{0}}\right\rangle_G \\ &= \omega^{\mu_j(d-1)} \mathbb{1} W_{(\mathbf{0},\boldsymbol{\mu}+(d-1)\boldsymbol{\Gamma}_j)} \left|\Psi_{\mathbf{0}}\right\rangle_G \\ &= \omega^{\mu_j(d-1)} \left|\Psi_{\boldsymbol{\mu}+(d-1)\boldsymbol{\Gamma}_j}\right\rangle_G \end{aligned} \tag{4.3.10}$$

□

4.4. Depolarization of states

For the sake of tractability, it is frequently useful to restrict the type of input states to a quantum information protocol to have a standard form. Furthermore, many simple models of noisy quantum states are diagonal in the graph state basis. An example is the state which corresponds to the target state with probability p, but to the maximally mixed state with probability $1-p$. Studying only a restricted form for input states may raise concerns however as to the wider applicability and performance of a protocol. In this section we demonstrate that there exists a procedure, called the depolarization procedure, by which a general multi-partite qudit state ρ with fidelity F to some target graph state $|G\rangle$ can be brought into a form that is diagonal in the graph state basis, without decreasing the fidelity F. This procedure may however decrease the overall entanglement of the state (according to some entanglement measure, such as the D-concurrence [42]), [51]. The existence of such a procedure allows restricting the class of input states to those which are diagonal in the graph state basis, without loss of generality.

Consider an arbitrary graph G with N vertices, $V = \{v_1, v_2, \cdots, v_N\}$, and N distinct spatially separated parties, each holding one of N qudits belonging to a general mixed state ρ. We consider the N particle graph basis states associated with G, $\{|\Psi_{\boldsymbol{\mu}}\rangle\}_G$. Since these states form a basis for the d^N dimensional state space $\mathcal{H}_{d,N}$, the density operator ρ may be expressed

$$\rho = \sum_{\boldsymbol{\mu},\boldsymbol{\nu}} \lambda_{\boldsymbol{\mu},\boldsymbol{\nu}} \left|\Psi_{\boldsymbol{\mu}}\right\rangle \left\langle\Psi_{\boldsymbol{\nu}}\right|_G . \tag{4.4.1}$$

We demonstrate that it is possible to depolarize ρ to a state ρ_G which is diagonal in the graph state basis using only LOCC operations, without altering the diagonal coefficients. Now, consider two graph basis states $|\Psi_{\boldsymbol{\mu}}\rangle_G$ and $|\Psi_{\boldsymbol{\nu}}\rangle_G$ which differ in at least one bit, say $\mu_1 \neq \nu_1$. Then, using the stabilizer generators introduced in

Section 4.2 and the eigenvalue equations for graph basis states from Section 4.3, we have that $g_1 |\Psi_{\boldsymbol{\mu}}\rangle_G = \omega^{-\mu_1} |\Psi_{\boldsymbol{\mu}}\rangle_G$ and $g_1 |\Psi_{\boldsymbol{\nu}}\rangle_G = \omega^{-\nu_1} |\Psi_{\boldsymbol{\nu}}\rangle_G$, where ω is the first $d-th$ primitive root of unity. If the N parties then jointly perform with uniform probability $\frac{1}{d}$ the operations corresponding to one of $\{\mathbb{1}, g_1, g_1^2, \cdots, g_1^{d-1}\}$, then the resulting state is

$$\rho_G = \frac{1}{d}\left(\rho + g_1\rho(g_1)^\dagger + g_1^2\rho(g_1^2)^\dagger + \cdots + g_1^{d-1}\rho(g_1^{d-1})^\dagger\right). \tag{4.4.2}$$

The amplitude of the term $|\Psi_{\boldsymbol{\mu}}\rangle \langle\Psi_{\boldsymbol{\nu}}|_G$ resulting from this process is

$$\frac{\lambda_{\boldsymbol{\mu},\boldsymbol{\nu}}}{d}(1 + \omega^{(\nu_1-\mu_1)} + \omega^{2(\nu_1-\mu_1)} + \cdots + \omega^{(d-1)(\nu_1-\mu_1)}). \tag{4.4.3}$$

For any possible combination of ν_1 and μ_1 such that $\mu_1 \neq \nu_1$ (both elements of $\mathbb{F}_d^N$), this amplitude is simply a multiple of the sum of the $d-th$ primitive roots of unity, and hence is equal to zero. If instead $\mu_1 = \nu_1$, then the sum in Equation 4.4.3 is equal to d and the diagonal coefficients remain fixed. Following suit, all off diagonal elements can be eliminated in a total of N rounds by probabilistically applying the operations corresponding to a power of $\{g_j\}\ \forall\ j \in \{1, \cdots, \mathrm{N}\}$ to the state resulting from the previous round. Overall, the resulting state is

$$\rho_G = \sum_{\boldsymbol{\mu}} \lambda_{\boldsymbol{\mu}} |\Psi_{\boldsymbol{\mu}}\rangle \langle\Psi_{\boldsymbol{\mu}}|_G ,$$

with $\lambda_{\boldsymbol{\mu}} \equiv \lambda_{\boldsymbol{\mu},\boldsymbol{\mu}}$.

4.5. Examples of two-colorable graph states

There are many possible configurations of two-colorable graphs possible, especially when allowing graphs that have weighted edges, as is appropriate for graphs corresponding to qudit graph states. For the sake of testing the efficacy of a purification protocol for graph states, it is helpful to have a particular class of TCGS in mind. In this work we will introduce and focus on two classes of TCGS: Greenberger–Horne–Zeilinger (GHZ) type states, and Linear Cluster states.

4.5.1. GHZ type states

GHZ type states on N qudits are an important class of entangled quantum state. In two dimensions, GHZ type states maximally violate N qubit Bell inequalities [53]. In general dimensions, GHZ type states are a useful resource for quantum communication protocols, including quantum secret sharing [2], [3], which can be used as a primitive for secure function evaluation. A GHZ state can be written as [54],

$$|\mathrm{GHZ}_{d,N}\rangle = \frac{1}{\sqrt{d}}\big(\,|0\rangle^{\otimes N} + |1\rangle^{\otimes N} + \cdots + |d-1\rangle^{\otimes N}\,\big)$$
$$= \frac{1}{\sqrt{d}}\big(\,|\mathbf{0}\rangle + |\mathbf{1}\rangle + \cdots + |\boldsymbol{d-1}\rangle\,\big). \tag{4.5.1}$$

A quantum graph state corresponding to either the *complete graph* or the *star graph*, of which examples are shown in Figure 4.1, is local Clifford equivalent to a GHZ type state. In Appendix C we demonstrate the local unitary equivalence of GHZ type states and star graph states by applying generalized Hadamard operations to all but the first qudit of a GHZ type state.

Definition 4.1. (Local complementation). For two sets X and Y define the symmetric difference between the sets by,

$$X\Delta Y = \big(X\bigcup Y\big)\backslash\big(X\bigcap Y\big). \tag{4.5.2}$$

Local complementation about a vertex v of a graph G is an operation τ_v which complements the induced subgraph on the neighborhood of v [9]. The neighborhood $\mathcal{N}_v$ of a vertex v consists of all the vertices which share an edge with v, i.e. $\mathcal{N}_v = \{u \mid (v,u) \in E\}$. For each vertex u of G, with neighborhood $\mathcal{N}_u$, the graph $\tau_v(G)$ resulting from local complementation about vertex v has the updated neighborhood,

$$\mathcal{N}_u^{(\tau_v(G))} = \begin{cases} \mathcal{N}_u \Delta (\mathcal{N}_v \backslash \{u\}), & \text{if } (u,v) \in E, \\ \mathcal{N}_u, & \text{otherwise.} \end{cases} \tag{4.5.3}$$

The complete graph is related to the star graph with vertex n as the central vertex by local complementation (Definition 4.1) about vertex n. In both the qubit case [9] and the qudit case with prime dimension $d > 2$ [55], local complementation about a single vertex can be accomplished by a Clifford operator; hence the complete graph state is local Clifford equivalent to the GHZ type state. Note that the complete graph is not two colorable, whereas the star graph is always two-colorable. For this reason, it is preferable to reference star graphs and not complete graphs when working with GHZ type states.

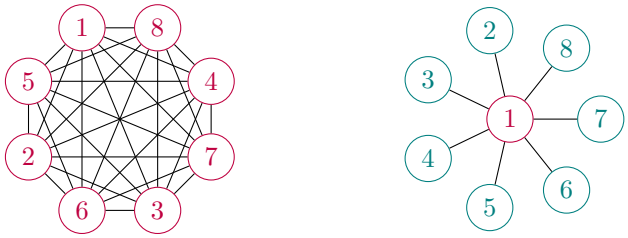

(a) The complete graph with 8 vertices (b) The star graph with 8 vertices

Figure 4.1: Graphs corresponding to graph states with local Clifford equivalence to GHZ type states.

4.5.2. Linear Cluster States

Cluster states are graph states corresponding to a square lattice graph in s spatial dimensions. For $s \geq 2$ it has been shown both for qubits [4] and for qudits with $d > 2$ [5] that cluster states constitute a universal resource for the so-called *one way quantum computer* [4]. One way quantum computation is an alternative approach to the circuit model of quantum computation, and it is based on performing measurements of resource states in order to perform a computation. Examples of s-dimensional cluster states for the first three spatial dimensions are shown in Figure 4.2. The name *linear cluster states* is given to cluster states in one spatial dimension. Note that the 3-dimensional cluster state shown in Figure 4.2c is only a single unit cell of the lattice.

(a) Linear cluster state: spatial dimension 1.

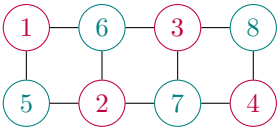

(b) Spatial dimension 2.

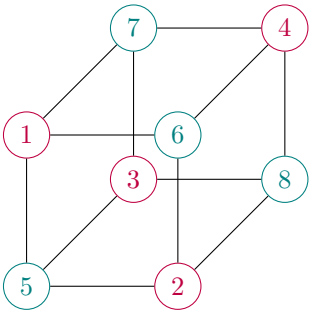

(c) Spatial dimension 3, unit cell.

Figure 4.2: Cluster states in the first three spatial dimensions.

Despite the simplicity of the description of cluster states within the stabilizer formalism, an explicit form for these states, in any basis, requires a number of terms

that is exponential in the number of qudits in the state. For the case of qubits, the tie between entanglement of cluster states and the large number of basis states needed to express them has been expressed in terms of the Schmidt measure – a measure for multi-partite entanglement [56]. For qubit states in spatial dimensions 1, 2, and 3 the entanglement as quantified by the Schmidt measure scales with the number of qubits and is $\lfloor \frac{N}{2} \rfloor$ [9]. For comparison, the Schmidt measure of any qubit GHZ type state is 1 [9], and hence does not scale with the number of qubits in the state.

Although linear cluster states are not a universal resource for one way quantum computation, unlike their higher spatial dimension counterparts, they are appealing as example states for performance evaluation of a protocol. From a performance evaluation standpoint linear cluster states are interesting because they are simple to work with in calculations, but they have the same degree structure (constant degree) as their higher spatial dimension counterparts. Additionally, at least by one measure (the Schmidt measure – proven in the qubit case) they have the same entanglement structure.

5

Recurrence scheme for qudit graph state purification

The recurrence based purification scheme for qudit TCGS we here propose is a simple extension of the qubit scheme presented in reference [25], with some important modifications that account for the difficulties presented by working over a configuration space with elements in $\mathbb{F}_d$ as opposed to $\mathbb{F}_2$. Recall that the vertices of a two-colorable graph can be split into two subsets, V_A and V_B of size $N_A = |V_A|$ and $N_B = |V_B|$, such that all vertices within one subset only share edges with vertices from the other subset; the set of edges of the graph is E. A perfect graph state corresponding to graph G is denoted $|\Psi_{\mathbf{0},\mathbf{0}}\rangle_G$. As explained in Equations 4.2.2 and 4.2.7, any N qudit quantum state can be represented in the graph state basis of the graph G and each of these basis states is uniquely labeled by a vector $\boldsymbol{\mu} = (\boldsymbol{\mu_A}, \boldsymbol{\mu}_B)$, where $\boldsymbol{\mu}_A \in \mathbb{F}_d^{N_A}$ and $\boldsymbol{\mu}_B \in \mathbb{F}_d^{N_B}$.

As setup, we consider N spatially separated experimenters who each require one qudit of a specific N qudit TCGS, corresponding to a graph G. They organize themselves into two groups, according to the sets V_A and V_B. The experimenters are able to collaborate in order to prepare identical copies of N qudit quantum states of fidelity F to their target graph state. These states are distributed such that each experimenter corresponds to a vertex of the desired graph state, and for every imperfect copy of the graph state an experimenter has control of the qudit matching their vertex. We will assume that the experimenters perform the depolarization procedure presented in Section 4.4, so that their input states are always diagonal in the graph state basis. That is, they can jointly prepare states

$$\rho = \sum_{\boldsymbol{\mu}_A, \boldsymbol{\mu}_B} \lambda_{\boldsymbol{\mu}_A, \boldsymbol{\mu}_B} \left|\Psi_{\boldsymbol{\mu}_A, \boldsymbol{\mu}_B}\right\rangle \left\langle\Psi_{\boldsymbol{\mu}_A, \boldsymbol{\mu}_B}\right|, \tag{5.0.1}$$

where $\lambda_{\mathbf{0},\mathbf{0}} = F$. We propose a purification protocol relying on local operations by each individual experimenter and classical communication between experimenters.

Success of the protocol is achieved probabilistically, as long as $F > F_{\min}$, where $F_{\min}$ is the minimal required initial fidelity. With this protocol, the group uses many input states of fidelity F to the desired graph state to prepare a single output state of target fidelity $\widetilde{F}$, where $\widetilde{F} > F$. The protocol consists of two subroutines, P1 and P2, which target errors on the subsets of qudits V_A and V_B, respectively. The subroutines take two identical copies of a state as input and are applied iteratively, so that two states output by the previous level of subroutines are used as input in the subsequent level of subroutines. In this way, the number of initial input states required is exponential in the number of levels of subroutine processing applied.

5.1. Purification subroutines

Each purification subroutine takes as input two identical copies ρ_1, and ρ_2 of a state ρ (Equation 5.0.1), diagonal in the graph state basis and with fidelity F to the target graph state. If the subroutine is successful, a single copy $\tilde{\rho}$ with fidelity $\widetilde{F}$ is output. The total input state is $\rho_{12} = \rho_1 \otimes \rho_2$. The lack of initial correlations between the two input copies is guaranteed by the initial depolarization procedure (Section 4.4).

The exact sequence of actions which make up subroutine P1 are detailed in Box 2. Subroutine P2 can be obtained from P1 by exchanging the roles of set V_A and V_B. The main difference in these sub-routines from the qubit version of the protocol, presented in [25], is that the parties in V_A apply different realizations of the CNOT gate to their qudits than the parties in V_B. In the qubit case all parties apply CNOT's because there is a unique realization of the CNOT gate in two dimensions.

Box 2: Subroutine: P1

Phase one: Local operations.

1. All parties belonging to set V_A apply local controlled raise operations, CX_d^+, to their two qudits, with the one from state ρ_2 as source and the one from state ρ_1 as target. See Figure 5.1c.

2. All parties from set V_B apply controlled lowering operations, CX_d^-, to their two qudits, with the one from ρ_1 as source and the one from ρ_2 as target. See Figure 5.1d.

The action of this sequence of multilateral controlled raising and lowering operations is,

$$|\Psi_{\boldsymbol{\mu}_A,\boldsymbol{\mu}_B}\rangle\,|\Psi_{\boldsymbol{\nu}_A,\boldsymbol{\nu}_B}\rangle \longmapsto |\Psi_{\boldsymbol{\mu}_A,\boldsymbol{\mu}_B\oplus\boldsymbol{\nu}_B}\rangle\,\left|\Psi_{\boldsymbol{\nu}_A\oplus(d-1)\boldsymbol{\mu}_A,\boldsymbol{\nu}_B}\right\rangle, \tag{5.1.1}$$

where $\oplus$ denotes addition modulo d. A proof is given in Appendix D.

Phase two: Measurements.

3. All qudits belonging to the set V_B of the second state copy ρ_2 are measured in the eigenbasis of the phase operator, $\{|0\rangle, |1\rangle, \cdots, |d-1\rangle\}$.

4. All parties belonging to set V_A apply a Hadamard operation to their qudit from state ρ_2. This changes the measurement basis from the phase basis to the shift basis.

5. All qudits belonging to set V_A of the second state copy, ρ_2, are measured in the eigenbasis of the shift operator $\{|0\rangle_x, |1\rangle_x, \cdots, |d-1\rangle_x\}$.

6. Each experimenter announces their measurement result over a classical communication channel.

The measurement results in the sets V_A and V_B yield results ω^{α_j} and ω^{β_i}, respectively, with $\alpha_j,\ \beta_i \in \mathbb{F}_d$, $i \in \mathbb{Z}_{N_A}$, $j \in \mathbb{Z}_{N_B}$.

Phase three: Post-selection.

7. Each party belonging to set V_A adds to their measurement result, α_j, the results of all parties from set V_B that share an edge with their vertex, $\{\beta_k \mid \Gamma_{jk} \neq 0\}$, weighted by the corresponding edge weight, Γ_{jk}, from the adjacency matrix $\boldsymbol{\Gamma}$.

8. Each party belonging to set V_A announces the result of their calculation modulo d. If every member of subset V_A obtains a result that is 0, then the subroutine is declared to have been successful.

That is, subroutine P1 is successful and the first state is kept if the measurement results fulfill the condition,

$$(\alpha_j + \sum_{(k,j)\in E} \Gamma_{jk}\beta_k) \bmod d = 0,\ \forall j \in \mathbb{Z}_{N_A}. \tag{5.1.2}$$

Fulfillment of this condition implies that $\boldsymbol{\mu}_A \equiv \boldsymbol{\nu}_A$. A full proof that subroutine P1 works as described is given in Appendix D. In the case that the measurement condition is not satisfied, the first state is also discarded and subroutine P1 failed.

Resulting state.

When the protocol is successful, the resulting state $\tilde{\rho}$ remains diagonal in the graph state basis and has the updated coefficients

$$\tilde{\lambda}_{\boldsymbol{\gamma}_A,\boldsymbol{\gamma}_B} = \sum_{\{(\boldsymbol{\mu}_B,\boldsymbol{\nu}_B)|\boldsymbol{\mu}_B\oplus\boldsymbol{\nu}_B=\boldsymbol{\gamma}_B\}} \frac{1}{K_1}\lambda_{\boldsymbol{\gamma}_A,\boldsymbol{\mu}_B}\lambda_{\boldsymbol{\gamma}_A,\boldsymbol{\nu}_B}, \tag{5.1.3}$$

where K_1 is a normalization constant, such that $tr(\tilde{\rho}) = 1$, and indicates the success probability of the protocol. Explicitly,

$$K_1 = \sum_{\boldsymbol{\mu}_A}\sum_{\boldsymbol{\mu}_B}\sum_{\boldsymbol{\nu}_B} \lambda_{\boldsymbol{\mu}_A,\boldsymbol{\mu}_B}\lambda_{\boldsymbol{\mu}_A,\boldsymbol{\nu}_B}. \tag{5.1.4}$$

To understand why the normalization factor K_1 corresponds to the success probability of the sub-routine, note that it is simply the probability that the measurement results are compatible with the post-selection condition, which determines the success of the sub-routine.

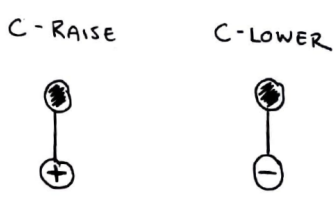

(a) Symbols for controlled raise (CX_d^+) and controlled lower (CX_d^-) operations.

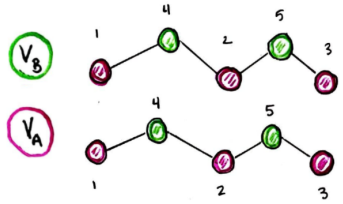

(b) Input: Two identical copies of an N qudit state.

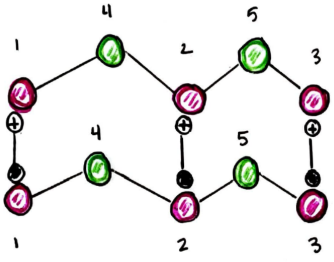

(c) Step 1: members of set V_A do CX_d^+ operations from state two to state one.

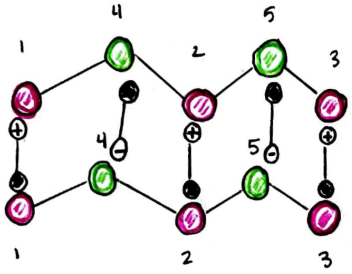

(d) Step 2: members of set V_B do CX_d^- operations from state one to state two.

Figure 5.1: Local operation sequence of subroutine P1. In (b), (c) and (d) the colored nodes of the two graphs represent qudits; the edges of the graphs represent entanglement between qudits. In each graph, the nodes in subset V_A are colored pink and drawn lower than the nodes in subset V_B, which are colored green.

The sequence of operations in phase one of subroutines P1 and P2 are visualized in Figures 5.1 and 5.2 respectively. Since subroutine P2 is simply obtained from P1 by exchanging the roles of set V_A and V_B, we do not explicitly run through the steps of the routine. Rather, we state only the post-selection condition and the formula for the coefficients of an updated state. Subroutine P2 is successful if the measurement results fulfill the condition

$$(\beta_i + \sum_{(i,k)\in E} \Gamma_{ki}\ \alpha_k) \bmod d = 0,\ \forall i\ \in \mathbb{Z}_{N_B}, \tag{5.1.5}$$

where $\{\beta_j\}$ is the set of measurement results recorded when all parties in set V_B measure their qudit from state copy two in the shift basis, and $\{\alpha_k\}$ is the set of measurement results recorded when all parties in set V_A measure their qudit from state copy two in the phase basis. When P2 is successful, the resulting state $\tilde{\rho}$ remains diagonal in the graph state basis and has the updated coefficients,

$$\tilde{\lambda}_{\boldsymbol{\gamma}_A,\boldsymbol{\gamma}_B} = \sum_{\{(\boldsymbol{\mu}_A,\boldsymbol{\nu}_A)|\boldsymbol{\mu}_A\oplus\boldsymbol{\nu}_A=\boldsymbol{\gamma}_A\}} \frac{1}{K_2}\lambda_{\boldsymbol{\mu}_A,\boldsymbol{\gamma}_B}\lambda_{\boldsymbol{\nu}_A,\boldsymbol{\gamma}_B}. \tag{5.1.6}$$

The normalization constant $K2$ is given by,

$$K_2 = \sum_{\boldsymbol{\mu}_A}\sum_{\boldsymbol{\nu}_A}\sum_{\boldsymbol{\mu}_B} \lambda_{\boldsymbol{\mu}_A,\boldsymbol{\mu}_B}\lambda_{\boldsymbol{\nu}_A,\boldsymbol{\mu}_B}. \tag{5.1.7}$$

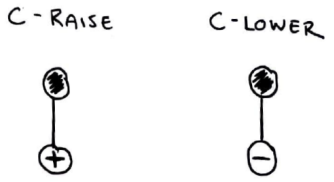

(a) Symbols for controlled raise (CX_d^+) and controlled lower (CX_d^-) operations.

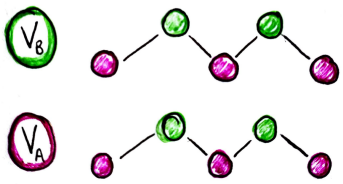

(b) Input: Two identical copies of an N qudit state.

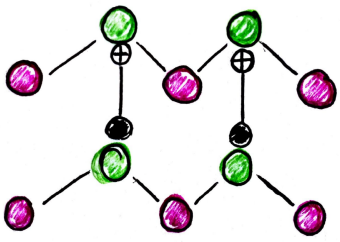

(c) Step 1: members of set V_B do CX_d^+ operations from state two to state one.

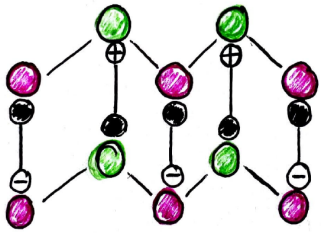

(d) Step 2: members of set V_A do CX_d^- operations from state one to state two.

Figure 5.2: Local operation sequence of subroutine P2. In (b), (c) and (d) the colored nodes of the two graphs represent qudits; the edges of the graphs represent entanglement between qudits. In each graph, the nodes in subset V_A are colored pink and drawn lower than the nodes in subset V_B, which are colored green.

5.2. Full purification protocol

The full purification protocol proceeds by iterative application of sub-protocols P1 and P2, always using two identical copies output by the previous iteration as input for the new round. For general input states diagonal in the graph state basis and an initial fidelity greater than the minimum, simple alternation between P1 and P2, starting with either P1 or P2 is an effective scheme for purification. We have not been able to devise a general proof that this scheme is effective – that is, without making reference to a particular class of input states – however in the following chapter we provide analysis of the efficacy with respect to three classes of input states, including both analytic and numeric results. We can however offer a general heuristic discussion of why the protocol works. Successful application of subroutine P1 reveals information about $\boldsymbol{\mu}_A$, resulting in purification within the subset V_A. On the other hand, subroutine $P2$ reveals information about $\boldsymbol{\mu}_B$, resulting in purification within the subset V_B. Overall purification requires interleaving the two subroutines, in order to extract information about both subsets of vertices. This scheme is not optimized, in the sense that for particular forms of input states, a sequence such as P1-P2-P1-P1-P1-P2-P2 may be more effective. In Section 6.1, we consider a type of input state for which repeated application of only sub-protocol P1 suffices.

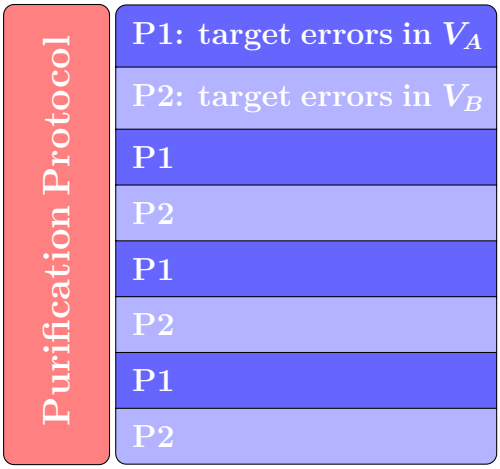

Figure 5.3: Subroutine structure of the purification protocol.

6

Performance analysis of the error-less protocol

In order to characterize the performance of the purification protocol presented in Chapter 5 we study the effect of purification on three different classes of input states. The performance of the protocol for states of different dimensions and node numbers is primarily measured using the minimal required fidelity of an input state as metric. In Section 6.3 we introduce the expected number of attempts required to successfully purify a noisy input state to a given target fidelity as another quantitative performance metric.

6.1. Binarylike mixtures

The first type of input state that we will consider are those where all of the errors are confined to one subset of nodes, either V_A or V_B. Given a specific two-colorable graph G, take for example states where all errors are confined to set V_A (i.e. $\boldsymbol{\mu}_B = 0$),

$$\rho_A = \sum_{\boldsymbol{\mu}_A} \lambda_{\boldsymbol{\mu}_A,\mathbf{0}} \left|\Psi_{\boldsymbol{\mu}_A,\mathbf{0}}\right\rangle \left\langle\Psi_{\boldsymbol{\mu}_A,\mathbf{0}}\right|_G . \tag{6.1.1}$$

Physically, this type of state could arise if an experimenter in an ideal laboratory locally prepares a perfect graph state $|\Psi_{\mathbf{0},\mathbf{0}}\rangle_G$ and keeps all of the nodes belonging to set V_B in noiseless memories, while sending each of the nodes from set V_A through dephasing channels to N_A other experimenters. For this type of state only application of sub-protocol P1 is needed in order to achieve purification, since only errors on set V_A need to be corrected. Given two identical copies of any state of this type, the result of a single successful round of protocol P1 is an output state $\tilde{\rho}_A$. According to Equations 5.1.3 and 5.1.4 the updated coefficients are

$$\tilde{\lambda}_{\boldsymbol{\mu}_A,\mathbf{0}} = \frac{\lambda^2_{\boldsymbol{\mu}_A,\mathbf{0}}}{\sum\limits_{\boldsymbol{\mu}_A} \lambda^2_{\boldsymbol{\mu}_A,\mathbf{0}}}. \tag{6.1.2}$$

Hence, conditioned upon success, this process applies a map which amplifies the

weight of the largest coefficient relative to the other coefficients. For distillation of these states to be possible it is then sufficient that $\lambda_{\mathbf{0},\mathbf{0}} > \lambda_{\boldsymbol{\mu}_A,\mathbf{0}}\ \forall \boldsymbol{\mu}_A \neq \mathbf{0}$.

For the sake of concreteness, we examine a one-parameter family of states,

$$\rho_A(F) := F\,|\Psi_{\mathbf{0},\mathbf{0}}\rangle\langle\Psi_{\mathbf{0},\mathbf{0}}|_G + \sum_{\boldsymbol{\mu}_A\neq 0}\frac{(1-F)}{(d^{N_A}-1)}\,|\Psi_{\boldsymbol{\mu}_A,\mathbf{0}}\rangle\langle\Psi_{\boldsymbol{\mu}_A,\mathbf{0}}|_G\,, \tag{6.1.3}$$

defined by the fidelity F between $\rho_A(F)$ and the ideal graph state. Using Equations 6.1.1 and 6.1.2, we determine the fidelity of the output state $\rho_A(\widetilde{F})$ to be

$$\widetilde{F} = \frac{F^2}{F^2 + \frac{(1-F)^2}{d^{N_A}-1}}. \tag{6.1.4}$$

The probability that a single round of protocol P1 is successful can be read from the normalization constant in the denominator of $\widetilde{F}$, and is equal to $F^2 + \frac{(1-F)^2}{d^{N_A}-1}$. As mentioned in Section 5.1, the normalization constant indicates the success probability of the protocol because it corresponds to the probability that the measurement results are compatible with the post-selection condition, which determines whether the protocol succeeds. The continuous map resulting from successful application of protocol P1 has attractive fixed points at $F = 0$ and $F = 1$, which are separated by a repulsive fixed point $F_{\min} = \frac{1}{d^{N_A}}$, corresponding to the minimum initial fidelity to achieve purification. The fixed point of fidelity equal to one is attractive for all initial fidelities greater than the minimum.

One observation that can already be made from the simple analysis of these binarylike input states is that the output fidelity $\widetilde{F}$ increases both with the dimension d and N_A, the number of nodes in set V_A. Hence the dimension of the underlying quantum systems and the type of graph state under consideration influence the efficacy of the protocol. Notice however that the final fidelity is independent of the total number of nodes in the graph state, and depends only on the number of nodes in the targeted subset, here V_A. In Figure 6.1 the initial and final fidelity are compared for various dimensions of the underlying quantum systems, first for a GHZ type state with any number of nodes (Figure 6.1a) and then for a five node linear cluster state (Figure 6.1b). Recall that a GHZ type state has only one node in the set V_A, so an N node GHZ type state has $N-1$ nodes in the set V_B, which are each connected by an edge to the single node in set V_A. Since for this type of input state the efficacy of sub-routine P1 depends only on N_A and not on N, the performance is the same for GHZ type states of any number of nodes, N. In contrast, for linear cluster states the number of nodes in set V_A scales with the number of nodes, N. The analytic results from Figure 6.1 confirm that the dimension of the underlying quantum systems makes a dramatic impact on the efficacy of the protocol, which

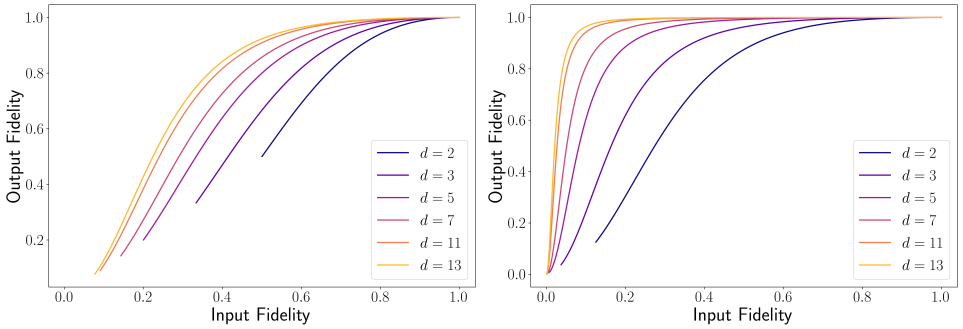

(a) GHZ state ($N_A = 1$). (b) 5 node linear cluster state ($N_A = 3$).

Figure 6.1: Input fidelity vs. output fidelity following a single application of P1 for various dimensions of the underlying quantum systems. Note that due to the different sizes of V_A in (a) the minimum fidelity to purify is $\frac{1}{d}$, whereas in (b) it is $\frac{1}{d^3}$.

produces a much higher output fidelity for a given input fidelity for systems of larger dimension.

To paint an intuitive picture of why purification should benefit so much from larger system dimension, we can consider the Von Neumann entropies [6] of the graph states before and after purification.

Definition 6.1. (Von Neumann entropy). The Von Neumann entropy of a quantum state ρ is

$$\mathrm{S}(\rho) = -\mathrm{Tr}\big(\rho \log_2(\rho)\big), \tag{6.1.5}$$

where the logarithm is usually defined to have base 2. If $\{\lambda_x\}$ are the eigenvalues of ρ, then the Von Neumann entropy may be re-expressed as

$$\mathrm{S}(\rho) = -\sum_x \lambda_x \log_2(\lambda_x). \tag{6.1.6}$$

In fact, using the change of base formula for the logarithm it is straightforward to show that changing the base of the logarithm in the Von-Neumann entropy yields a simple re-scaling of the entropy.

Definition 6.2. (Re-scaled Von Neumann entropy). For a quantum state ρ, the re-scaled Von Neumann entropy is given by

$$S_a(\rho) = -\mathrm{Tr}(\rho \log_a(\rho)). \tag{6.1.7}$$

The relation between $S_a(\rho)$ and $S(\rho)$ is as follows,

$$S_a(\rho) = \frac{S(\rho)}{\log_2(a)}. \tag{6.1.8}$$

An insightful interpretation of the re-scaled Von Neuman entropy is provided by Achim Kempf [57], "*the amount of ignorance, i.e. the entropy,* $\boldsymbol{S_a}$*, is the number of questions – of the type that possess* $\boldsymbol{a}$ *possible outcomes – that we would need to have answered to remove our ignorance*". It follows from this interpretation that when working with qudits of dimension d, it is most natural to use S_d to measure the entropy, since any questions we ask about the quantum states (i.e. measurements), will have d possible outcomes. For the one parameter family of states under consideration, the entropy of the initial states is given by

$$S_{a,\mathrm{In}} = -\Big(F \cdot \log_a(F) + (1-F) \cdot \log_a\left(\frac{1-F}{d^{N_A}-1}\right)\Big). \tag{6.1.9}$$

Following a single successful round of purification the density matrix has coefficients given by (6.1.2) and has entropy:

$$S_{a,\mathrm{Out}} = -\big(\widetilde{F} \cdot \log_a(\widetilde{F}) + (d^{N_A}-1)(1-\widetilde{F}) \cdot \log_a(1-\widetilde{F})\big). \tag{6.1.10}$$

To emphasize the role of dimension, first fix $a = 2$ in Equations 6.1.9 and 6.1.10, meaning that the entropies are calculated with log base 2, as in the standard Von Neumann entropy. Note that for any fixed fidelity and number of nodes in V_A, the initial entropy of the states rises with the dimension of the qudits, since increasing the dimension shrinks the argument of the logarithm. In contrast, the entropy of the output states decreases with the dimension, which can easily be verified by numeric evaluation of Equation 6.1.10. In terms of entropy then, the purification process is more effective for larger dimensions because a greater total amount of entropy is removed by the procedure and an output state of lower entropy relative to those from smaller dimensions is achieved. The preceding statements are illustrated in Figure 6.2a, which compares for several dimensions the initial Von Neumann entropy of a five node linear cluster state to the ratio of the initial to final entropy, in a single log plot. Now, for the sake of emphasizing that for d dimensional qudits it is helpful to consider the re-scaled entropy S_d, set $a = d$ in Equations 6.1.9 and 6.1.10. As can be seen in Figure 6.2b, with this change the previous remarks – that for larger dimensions the purification process is more effective because a greater total amount of entropy is removed – still hold true. The benefit of working with the re-scaled entropy, S_d, is that it removes the staggering of magnitudes of the initial entropy, which are due to the differences in minimum initial fidelity between the dimensions, allowing for a clearer comparison.

6.2. One parameter family of fully mixed states

Another simple type of input state that can be considered is a one parameter mixture between the perfect graph state and a fully mixed state. Given a specific two-colorable graph G with $|V| = N$ and taking x to be the control parameter, this

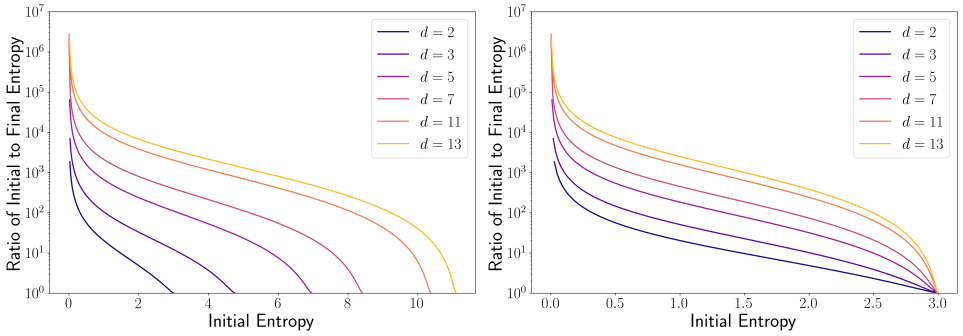

(a) Standard Von Neumann entropy, S_2.

(b) Re-scaled entropy, S_d.

Figure 6.2: Ratio of the initial and final Von Neumann entropy (log scale) compared with the initial Von Neumann entropy of a 5 node linear cluster state ($N_A = 3$).

family of states can be written,

$$\rho(x) = x \left|\Psi_{\mathbf{0},\mathbf{0}}\right\rangle \left\langle\Psi_{\mathbf{0},\mathbf{0}}\right|_G + \frac{1-x}{d^N}\mathbb{1}, \tag{6.2.1}$$

where d is the dimension of the qudits which form the nodes of the graph state. This type of state is realized physically if an experimenter executes a preparation procedure that works flawlessly with probability x, but malfunctions and creates a completely unknown state on the N qudits with probability $(1-x)$. For this family of states we analytically examine the effect of applying one round of purification, using either sub-protocol P1 or P2 and then numerically simulate further rounds of purification which proceed by alternating between P1 and P2. The fidelity of an input state from this family to the perfect graph state is $x + \frac{1-x}{d^N}$. Following a single successful application of sub-routine P1 or P2, the fidelity of the output state is calculated using Equation 5.1.3 or 5.1.6, resulting in Equation 6.2.2 or 6.2.3, respectively.

$$\widetilde{F}^{(\mathrm{P1})}(x) = \frac{d^{N_A}}{(x^2(d^{N_A}-1)+1)}\left(x^2 + 2x\frac{1-x}{d^N} + d^{N_B}\frac{(1-x)^2}{d^{2N}}\right), \tag{6.2.2}$$

$$\widetilde{F}^{(\mathrm{P2})}(x) = \frac{d^{N_B}}{(x^2(d^{N_B}-1)+1)}\left(x^2 + 2x\frac{1-x}{d^N} + d^{N_A}\frac{(1-x)^2}{d^{2N}}\right). \tag{6.2.3}$$

The success probabilities of sub-protocols P1 and P2 can be read off from the pre-factor in the updated fidelity, and are $p_{\mathrm{succ}}^{(\mathrm{P1})} = d^{-N_A}(x^2(d^{N_A}-1)+1)$ and $p_{\mathrm{succ}}^{(\mathrm{P2})} = d^{-N_B}(x^2(d^{N_B}-1)+1)$, respectively. Comparison of the updated fidelity and success probability corresponding to each of the sub-protocols exposes that differences in magnitude between the two are dictated entirely by the number of nodes in the subsets V_A and V_B.

By analytically studying the updated coefficients following a single application of sub-routine P1 or P2 we determine the minimum fidelity on input states necessary to achieve purification. Each of the functions corresponding to P1 or P2 respectively has three fixed points in the fidelity[1], i.e. where $\widetilde{F}(F) = F$; for both functions the first is $\widetilde{F} = 1 = F$, which occurs when $x = 1$; for both functions the second is $\widetilde{F} = \frac{1}{d^N} = F$, which occurs for $x = 0$; the third fixed point for either function[2] can be used to determine the minimum purification fidelity. The third fixed point of the two functions occurs at the parameter:

$$x_*{}^{(\mathrm{P1})} = \frac{d^N - 2d^{N_A} + 1}{1 - d^N - d^{N_A} + d^{N+N_A}} \tag{6.2.4}$$

$$x_*{}^{(\mathrm{P2})} = \frac{d^N - 2d^{N_B} + 1}{1 - d^N - d^{N_B} + d^{N+N_B}} \tag{6.2.5}$$

Having analytically determined the points $x_*{}^{(\mathrm{P1})}$, $x_*{}^{(\mathrm{P2})}$, we numerically verify that for any input state $\rho(x)$ such that $x > \max(x_*{}^{(\mathrm{P1})}, x_*{}^{(\mathrm{P2})})$ purification can be achieved by nested alternating application of P1 and P2, and an output state of fidelity 1 can be achieved asymptotically in the number of purification steps. In the non-asymptotic regime, meaning when we consider any specific finite number of purification subroutine iterations, a final fidelity that is arbitrarily close to one can be achieved given any initial x value greater than the minimum and using a finite number of purification stages, succeeding with a non-zero cumulative probability. Figure 6.3 illustrates for a 3 node GHZ type state with $d = 5$ that starting from an initial x value greater than the minimum by only $1e-4$, updated fidelities larger than $1-1e-2$, $1-1e-3$, $1-1e-6$ and $1-1e-7$ can be achieved after 4, 5, 6, and 7 rounds of purification respectively. Note that the cumulative success probability of the protocol in Figure 6.3 is very low, at about 20%; in contrast, the individual purification subroutine success probability is less than 50% only for the first iteration, and the probabilities subsequently rise to near 100% by the fifth iteration. We conclude that the cumulative probability is limited by the success probability of the first purification subroutine, which for the case of an input state with nearly the minimal initial fidelity, is very low. Thus the drawback of purifying states near the boundary of the purification regime is a limited probability of success.

Keeping in mind that any state in this family with initial x value greater than the minimum can be purified to a fidelity arbitrarily close to one, the minimum initial fidelity is a quantitative measure that can be used to draw comparison between

[1] As opposed to fixed point in the parameter x, which would be $\widetilde{F}(x) = x$.

[2] The expression of the fidelity of the third fixed point is more complicated, so we confine ourselves to only presenting the formula for the parameter at which it occurs.

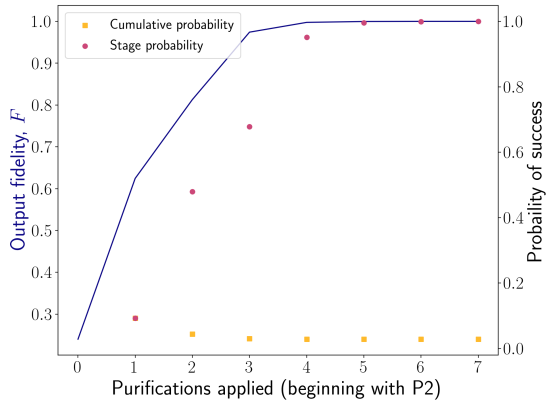

Figure 6.3: Left axis: Fidelity of output state $\rho(\tilde{x})$ versus number of purification steps applied, beginning with sub-protocol P2 and alternating between P1 and P2 thereafter, for a 3 node GHZ type state ($N_A = 1,\ N_B = 2$) with underlying system dimension of 5. Right axis: probability that the indicated purification step succeeds (red markers) and probability that the overall sequence of purification steps succeeds (teal markers). For this input state ${x_*}^{(\mathrm{P1})} = 0.2339$ and ${x_*}^{(\mathrm{P2})} = 0.0255$, and the initial x value (corresponding to purification step 0) was chosen to be $x = 1e-4+\max({x_*}^{(\mathrm{P1})}, {x_*}^{(\mathrm{P2})})$.

states of different dimensions, as well as between linear cluster and GHZ type states. In Figure 6.4 we plot the minimum initial fidelity required to achieve purification against the number of qudits in the graph state for (a) linear cluster states and (b) GHZ type states, for various dimensions of the qudits making up the graph states. From Figure 6.4a, it is apparent that for every dimension of qudit considered the minimum initial fidelity decreases approximately exponentially in the number of qudits that make up the state. In contrast, for GHZ states, (Figure 6.4b) the minimum fidelity required actually increases with the size of the graph state. For both types of states we see that states made up of qudits of larger dimension have far less stringent minimal initial fidelities that their lower dimension counterparts, and hence can be distilled for a much larger range of fidelities.

6.3. Depolarized states

The most important family of noisy quantum states that we will consider are depolarized states. These are states where each of the qudits in the state has been subject to depolarizing noise. Physically, this type of state corresponds to the preparation of a perfect graph state in an ideal laboratory, followed by subsequently sending each qudit through a depolarizing channel to a new laboratory, where a different experimenter will have control of that qudit throughout the rest of the protocol. Within

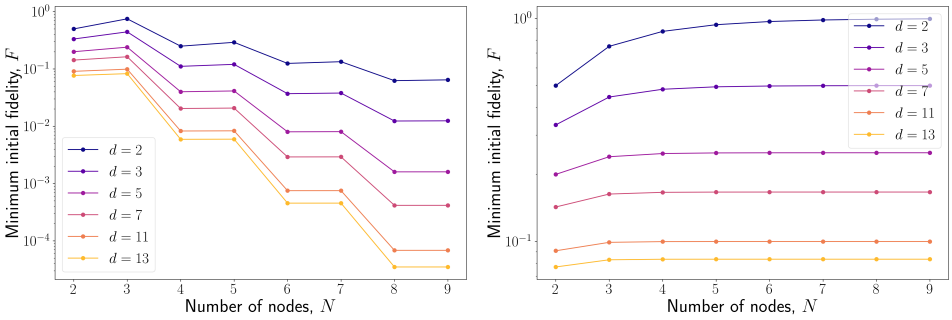

(a) Linear cluster state.

(b) GHZ type state.

Figure 6.4: Minimum initial fidelity required to achieve purification vs. the number of qudits in the graph state, N for (a) linear cluster type states and (b) GHZ type state, for various dimensions of the states qudits.

the restriction to uncorrelated error models this is a sort of worst case preparation procedure, since real sources of uncorrelated noise are not perfectly depolarizing. We expect any noise source where some errors are less common than others to have a less harmful effect on entangled states than depolarizing noise, as long as any quantitative comparison considers the error parameter for the weaker noise to be based on the most probable error type. For modelling of the depolarizing channel, refer to Section 2.2.1. For a TCGS G, label the nodes in subset V_A of size $N_A = |V_A|$ by $\{a_1, a_2, \cdots, a_{N_A}\}$ and the nodes in V_B of size $N_B = |V_B|$ by $\{b_1, b_2, \cdots, b_{N_B}\}$. The multi-particle state that results from sending each node of the perfect TCGS through such a channel is

$$\rho(q) = \mathcal{E}_{a1} \circ \cdots \mathcal{E}_{a_{N_A}} \circ \mathcal{E}_{b1} \circ \cdots \circ \mathcal{E}_{b_{N_B}} \left(|\Psi_{\mathbf{0}}\rangle \langle \Psi_{\mathbf{0}}|_G \right), \tag{6.3.1}$$

where each $\mathcal{E}_j$ is given by 2.2.6. Notice that $q = 0$ corresponds to perfect transmission, whereas $q = \frac{d^2-1}{d^2}$ corresponds to a completely depolarized state. Observe from Equation 2.2.6 that charting the effect of the depolarization channel requires the action of $d^2 - 1$ operators per qudit in the N qudit state. The depolarization process may introduce up to d^N terms (the size of the graph state basis) into the quantum state. Overall then, determining the depolarized state $\rho(q)$ involves the action of $N \times (d^2 - 1)$ operators on up to d^N graph basis states. As a result of the exponential scaling involved in determining and representing the depolarized input state, we proceed by numerical analysis to study the purification regime for depolarized input states. In Appendix F.1 we verify the correctness of the numerical depolarization channel by comparison to an analytical calculation for a qubit GHZ type state with three nodes.

The purification regime for depolarized input states is defined by two different met-

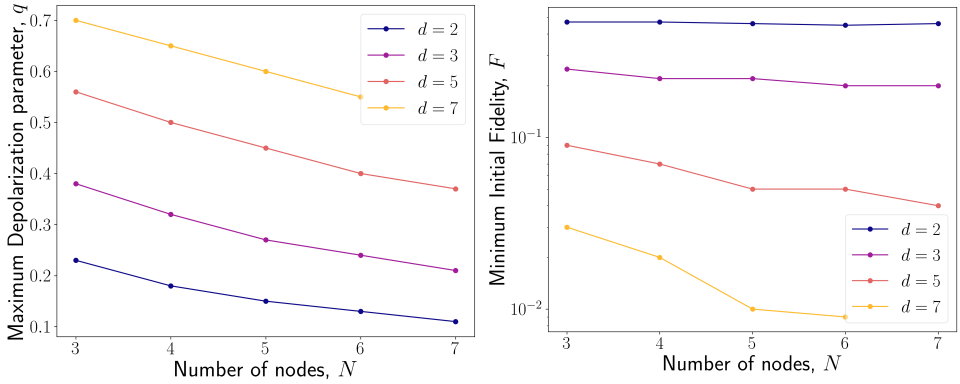

(a) Maximum depolarization noise per qudit.

(b) Minimum fidelity to achieve purification.

Figure 6.5: Purification regimes for depolarized GHZ type states of qudits of low prime dimensions.

rics. The first is the maximum depolarization noise that is tolerated per qudit of an N qudit state, meaning the maximum q such that the state $\rho(q)$ can still be purified by the purification protocol. We consider the depolarization noise applied per qudit to be equal across the entire state. In a realistic scenario we may suppose that each qudit of a graph state may be subjected to a slightly different level of noise, for example in the case of white noise where the noise parameter q is distributed according to a Gaussian distribution with some mean μ and standard deviation σ. If the standard deviation of the noise is small relative to the mean, then we expect the performance with a constant noise level on each qudit to be a faithful reflection of the performance with variable per qudit noise. The other metric of interest is the minimal fidelity to the perfect graph state that a depolarized state can have and still be purified. The minimal fidelity of a depolarized input state is set by the maximum depolarization noise per qudit. In Figures 6.5 and 6.6 we plot for GHZ type states and linear cluster states, respectively, first the scaling of the maximum depolarization parameter with d and N, and then the scaling of the minimal initial fidelity with d and N. Immediately it is evident from the figures that there is very favorable scaling with the dimension, both in the maximum depolarization noise tolerated per qudit as well as in the minimum initial fidelity, for both families of states. The scaling with N however, differs between the two families of states. For GHZ type states the maximal amount of depolarization noise tolerated per qudit decreases as the number of nodes of the graph state increases. In contrast, for linear cluster type states the maximal amount of depolarization noise tolerated is essentially constant in the number of nodes, N.

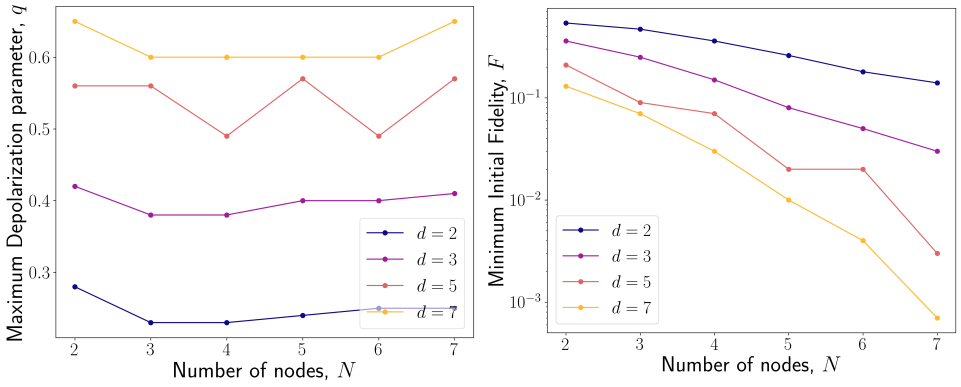

(a) Maximum depolarization noise per qudit.

(b) Minimum fidelity to achieve purification.

Figure 6.6: Purification regimes for depolarized linear cluster states of qudits of low prime dimensions.

To explain the differences in scaling of the purification range with N between GHZ and linear cluster type states, we look to the structure of the graphs. We propose that noise tolerance per qudit of a TCGS is chiefly dependent upon the degree of the related graph. Recall that the degree of a vertex in a graph is the number of edges which terminate at that vertex, and we call the degree of the graph the maximum degree of any of the vertices. From Sections 4.5.1 and 4.5.2, the degree of the graph corresponding to a GHZ type state is $N - 1$, whereas the degree of a linear cluster state is 2 – independent of N. In the qubit case, the proposition that the noise tolerance per qudit depends on the degree of the graph as opposed to N is supported by previous analysis [25]. Understanding why the degree of the graph has the dominant impact on the noise tolerance per qudit is possible with reference to Equation 4.3.7, which says that when a shift type error occurs on a qudit, it is equivalent to phase type errors occuring on each of the qudits with which it shares an edge in the graph. This means that any vertex with high connectivity (large degree) is exposed to a large amount of excess errors. It is as if vertices with high degree see a higher effective noise level than that which is being strictly applied per qudit.

The proposition that degree of the graph dictates the noise tolerance per qudit is also instrumental in explaining why the minimal fidelity required to purify linear cluster states drops exponentially with the number of nodes in the state, Figure 6.6b. Since the degree of linear cluster states is constant, the amount of noise tolerated per qudit in the state is independent of the node number. As the number of nodes in a state is increased then, the total amount of noise tolerated increases,

resulting in a decrease of the minimal initial fidelity. Although it is theoretically quite interesting that states with very low initial fidelity (example: $F = 1e-3$ for a 7 node linear cluster state with $d = 7$) can be purified by the protocol, there is a practical limitation restricting the usefulness of such low fidelity states. The success probability of the protocol is proportional to the fidelity of the input state, so the expected number of attempts necessary to a successfully complete a subroutine iteration grows sharply for states of very low input fidelity. Moreover, for states of lower input fidelity a greater number of subroutine iterations will be required in order to reach any specific target fidelity.

To look closer at the practicality of using this protocol we will consider a scenario in which a target fidelity of 0.99 is set for purification, and the depolarized input states have been prepared with 20% depolarization noise, i.e. $q = 0.20$. For linear cluster states with 3 or 7 nodes and in various prime dimensions, we determine how many purification subroutine iterations are necessary to reach the target fidelity, as well as the expected number of attempts needed to successfully complete the protocol. The expected number of attempts needed to complete the total protocol can be calculated from the number of attempts required to complete each subroutine iteration, which follows a geometric distribution [58], with iteration success probability p_k, where k is the iteration number. Recall from Section 5.1 that the probability of success for an iteration of subroutine P1 (P2) is given by Equation 5.1.4 (5.1.7). Because each subroutine iteration takes two states from the previous iteration as input, reaching the $k-th$ subroutine iteration requires completing the first iteration $2^{(k-1)}$ times, the second iteration $2^{(k-2)}$ times, etc. Overall, the expected number of attempts to complete a protocol consisting of K subroutine iterations is given by,

$$\text{Expected number of attempts } = 2^{\frac{K(K-1)}{2}} \left\lceil \frac{1}{p_1 p_2 \cdots p_M} \right\rceil \tag{6.3.2}$$

The results indicated in Figure 6.7 indicate that both the number of subroutine iterations required as well as the corresponding expected number of attempts needed to reach the target fidelity drop dramatically with increasing dimension. The minimum number of iterations needed to reach the target fidelity for a depolarized input state is 2, since one iteration of each of subroutines P1 and P2 is needed. Of particular importance is the steep decline of the expected number of attempts, as this consideration can be considered a limiting factor for the practical execution of the protocol. We see from comparison of Figures 6.7a and 6.7b that the expected number of attempts is especially favorable for smaller linear cluster states with dimensions greater than 7. It is also interesting to point out that for $d = 2$ the expected number of attempts is inordinate (10^{15} for the 3 node state and 10^{11} for the 7 node state), which partially occurs because the depolarization parameter 0.2 is very near the critical parameter (Figure 6.6a) for $d = 2$.

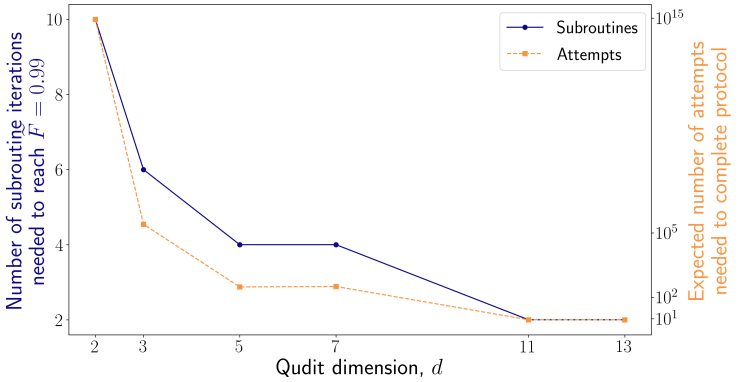

(a) 3 Node Linear Cluster State.

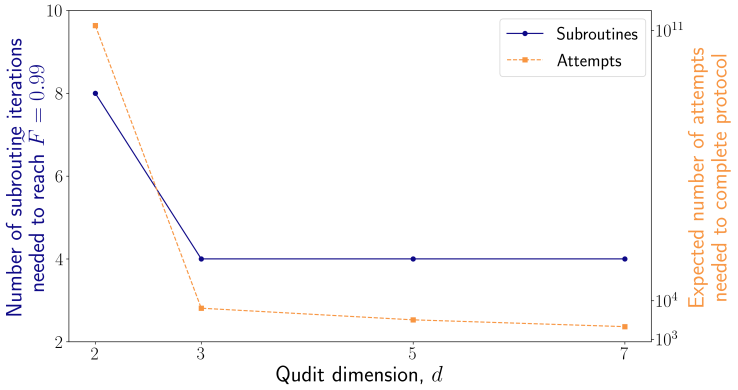

(b) 7 Node Linear Cluster State.

Figure 6.7: The number of purification subroutine iterations (left axis), and the corresponding overall expected number of attempts (right axis) required in order to reach a target fidelity of $\widetilde{F} = 0.99$ by purifying a depolarized input state with depolarization parameter $q = 0.2$.

7

Performance analysis with imperfect local operations

Up until this point we have considered perfect execution of the purification protocol, including perfect two-qudit operations and perfect measurements. In reality, quantum operations are imperfect and generally are associated with some level of error. We now study the performance of the purification protocol when all two-qudit operations (2.1.15 and 2.1.17) mandated by the protocol are faulty. We consider an error model where faulty local two qudit operations are described by the completely positive map,

$$\mathcal{E}_{U_{jk}}(\rho) = U_{jk}[\mathcal{E}_j \circ \mathcal{E}_k(\rho)]U_{jk}^{\dagger}, \tag{7.0.1}$$

in which U_{jk} is a local unitary operation between qudits j and k of a quantum state, and $\mathcal{E}_j$, $\mathcal{E}_k$ are given by Equation 2.2.6 or 2.2.8, with error parameter q. That is, a two qudit faulty unitary operation is modelled by applying a noise process with probability q to each qudit independently, followed by application of the perfect unitary operation.

Throughout the performance analysis of the error-less protocol conducted in Chapter 6 one of the most important performance metrics is the minimal initial fidelity that an input state must have, since this fidelity marks the boundary of the purification regime. The upper boundary of the purification regime in the error-less case is always a final state fidelity of $\widetilde{F} = 1$. When errors are introduced into the purification protocol the upper boundary of the purification regime changes, and there is for every gate error parameter a maximal reachable fidelity for the purification protocol. In studying the protocol with faulty two qudit operations the size of the purification regime, defined as the region between the minimum required and maximal reachable fidelity, for any specific gate error, is used to define the performance metric of interest, which is the *gate error threshold*. The error parameter for which the purification regime disappears (the minimum initial fidelity and maximum reachable fidelity converge) is defined to be the gate error threshold. Viewed

another way, the error threshold is the maximum value of q_g for which purification remains possible.

To study the performance of the protocol we first develop analytic results under a limited noise model, where the error processes $\mathcal{E}$ are restricted to shift type errors, given by Equation 2.2.8, for a restricted class of input states. Then, we remove these constraints and numerically study the performance when the operations are afflicted by white noise and the input states are depolarized states (Equation 2.2.7). The numerical analysis is computationally limited by speed and memory requirements, since the density matrix for two copies of an imperfect state $\rho_{12} = \rho_1 \otimes \rho_2$, diagonal in the graph state basis, with N nodes in d dimensions, contains d^{2N} terms. This unfavorable exponential scaling of the number of terms in the states restricts the numerical analysis to low dimensions and node numbers.

7.1. Analytical analysis under a restricted noise model

It is possible to derive analytic results for the gate error threshold of the purification protocol with two qudit gate errors by restricting both the error model and the class of input states considered. As a consequence of the restrictions, such results are only an upper bound on the tolerance of the protocol to errors under a more general error model. From the upper bounds we can extract predictions about the trends of scaling with dimension and node number when a more general error model and input states are considered.

To begin, we restrict to input states that are binary-like mixtures, meaning that the input states have been subject to dephasing noise only on nodes from one subset, V_A or V_B. The performance of the error-less protocol with this class of input states is covered in Section 6.1. As before, without loss of generality we work through the analysis with input dephasing noise constrained to subset V_A, so that the input states have the form,

$$\rho_A = \sum_{\boldsymbol{\mu}_A} \lambda_{\boldsymbol{\mu}_A,\mathbf{0}} \left|\Psi_{\boldsymbol{\mu}_A,\mathbf{0}}\right\rangle \left\langle\Psi_{\boldsymbol{\mu}_A,\mathbf{0}}\right|_G . \tag{6.1.1}$$

Since the input state only has imperfections on one subset of nodes, it is suitable to only execute the purification subroutine targeting that subset. In the case of our example that means subroutine P1, targeting subset V_A.

The next restriction is to the error model, describing the functioning of the two-qudit operations in the purification subroutine. We consider shift error type noise, as described by Equation 2.2.8. Moreover, we impose the constraint that only

operations on qudits from set V_B are faulty. That is, we model faulty two-qudit operations by,

$$\mathcal{E}_{U_{jk}}(\rho_{12}) = U_{jk}\big[\mathcal{M}_j\mathcal{M}_k(\rho_{12})\big]U_{jk}^{\dagger}, \tag{7.1.1}$$

with the error processes $\mathcal{M}$ given by,

$$\mathcal{M}_j(\rho) = \begin{cases} \mathbb{1}, \text{ if } j \in V_A, \\ (1-q)\rho + \frac{q}{d-1}\sum_{m=1}^{d-1} X_j^m \rho (X_j^m)^{\dagger}, \text{ if } j \in V_B. \end{cases} \tag{7.1.2}$$

Notice that these faulty gates act on the opposite subset from the one involved in the binary mixture, 6.1.1. The reason for this choice follows from Equation 4.3.7, which says that shift type errors on vertices of subset V_B are equivalent to phase type errors on the adjacent nodes from subset V_A. The advantage of this combined choice of error model and binary-like input states is that the states maintain their binary-like form under the noise model, making it possible to treat the purification process analytically.

It is useful to ask whether the error processes and the two qudit unitaries commute, because if this is the case then it is sufficient to determine the effect of the error processes on the input state, followed by the known action of the perfect subroutine P1, given by Equation 5.1.3. The answer to this question is affirmative, as summarized by proposition 7.1, which is proven in Appendix E.

Proposition 7.1. Application of purification subroutine P1 (P2)[1] with faulty two-qudit operations modeled by Equations 7.1.1 and 7.1.2 is equivalent to first applying all noise processes, followed by application of the errorless purification subroutine.

Having established the setting of the analytical treatment, we present the analysis for two particular classes of input states, namely GHZ type states and closed linear cluster states. These two classes of states are amenable to analytical treatment primarily because they correspond to graphs with very simple adjacency matrices.

7.1.1. GHZ type states

For GHZ type states the vertex subset V_A contains only one node. We will consider binary-like mixture type input states belonging to the one parameter family,

$$\rho_A(x) = x\,|\Psi_{0,\mathbf{0}}\rangle\langle\Psi_{0,\mathbf{0}}| + (1-x)\frac{\mathbb{1}_{V_A}}{d}, \tag{7.1.3}$$

[1] For use of P2 we must consider binarylike input states with noise confined to subset V_B and the the restricted error model must be modified by swapping the role of subsets V_A and V_B in equation 7.1.2

where $\mathbb{1}_{V_A} := \sum_{l=0}^{d-1} |\Psi_{l,\mathbf{0}}\rangle$. The full input state is $\rho_{12} = \rho_A(x) \otimes \rho_A(x)$, however since we will apply all of the error processes before the two-qudit gates, we can apply them to each state independently. Since the two state copies begin unentangled and the error processes are uncorrelated, the copies remain unentangled following the error processes. Overall then, it suffices to determine $\mathcal{M}_{b_{N_B}} \circ \cdots \circ \mathcal{M}_{b_2} \circ \mathcal{M}_{b_1}\big(\rho_A(x)\big)$, where b_i is the i-th vertex in V_B, $i \in \{1, \cdots, N_B\}$. The following proposition, which is proven in Appendix E, makes it possible to determine the effect of the sequence of error processes.

Proposition 7.2. The state resulting from the error process $\mathcal{M}_{b_j}(\cdot)$, $j \in \{1, \cdots, N_B\}$, given by Equation 7.1.2, on an input state given by Equation 7.1.3, remains of the same form but with the new parameter $x(1-q)$. That is,

$$\mathcal{M}_{b_j}\big(\rho_A(x)\big) = \rho_A(x(1-q)). \tag{7.1.4}$$

The following Corollary, which summarizes the effect of all $N-1$ error processes, can be established by repeated application of Equation 7.1.4.

Corollary 7.1. The state resulting from the error processes affecting all $N-1$ nodes of subset V_B is given by,

$$\mathcal{M}_{b_{N_B}} \circ \cdots \circ \mathcal{M}_{b_2} \circ \mathcal{M}_{b_1}\big(\rho_A(x)\big) = \rho_A(x'), \text{ with } x' = x(1-q)^{N-1}. \tag{7.1.5}$$

The meaning of this corollary is that for input states of the form described in Equation 7.1.3, the effect of purification subroutine P1 with faulty two qudit operations is equivalent to the action of the perfect subroutine on input states $\rho_A(x')$, with $x' = x(1-q)^{N-1}$, where q is the parameter which characterizes the error level of the faulty operations. With this result in hand, the effect of the faulty purification subroutine can be determined by applying the coefficient update formula for subroutine P1, adapted to binary-like mixtures – Equation 6.1.2, to the state $\rho_A(x')$. Of particular interest is the effect that this procedure has on the fidelity of the state. The fidelity of the original input state, $\rho_A(x)$ is $F = x + \frac{1-x}{d}$. Following the noise processes, the state $\rho_A(x')$ has fidelity $F' = x' + \frac{1-x'}{d} = x(1-q)^{N-1} + \frac{1-x(1-q)^{N-1}}{d}$. Using Equation 6.1.4, the updated fidelity resulting from application of the error-less subroutine P1 to $\rho_A(x')$ is given by,

$$\begin{aligned}\widetilde{F} &= \frac{F'^2}{F'^2 + \frac{(1-F')^2}{d-1}} \\ &= \frac{\left(x(1-q)^{N-1} + \frac{1-x(1-q)^{N-1}}{d}\right)}{\left(x(1-q)^{N-1} + \frac{1-x(1-q)^{N-1}}{d}\right)^2 + \frac{\left(1-x(1-q)^{N-1} - \frac{1-x(1-q)^{N-1}}{d}\right)^2}{d-1}}.\end{aligned} \tag{7.1.6}$$

To achieve purification, it is necessary that $\widetilde{F} > F$. To determine the critical values for q and x, that is the values which define the boundary of the purification regime, we look for fixed points in of the fidelity, $\widetilde{F}(x,q) = F(x)$. In Appendix E we derive the maximum value of x for a given error parameter q, which defines the maximum reachable fidelity for a given error parameter q, as well as the error threshold q_{crit}.

When purification subroutine $P1$ with faulty two-qudit operations of the form described by Equations 7.1.1 and 7.1.2 is used to purify states of the form given in Equation 7.1.3, the maximum state parameter $x_{\max}$, which defines the maximum reachable fidelity, is given by,

$$x_{\max} = \frac{\frac{d-2}{d-1}(1-q)^{2(N-1)} + \sqrt{\left(\frac{d-2}{d-1}\right)^2(1-q)^{4(N-1)} + 4(1-q)^{2(N-1)}\left(\frac{2(1-q)^{N-1}-1}{d-1}\right)}}{2(1-q)^{2(N-1)}}. \tag{7.1.7}$$

The maximum reachable fidelity for a given error level, q, is $\widetilde{F}_{\max}(x_{\max}, q)$, where $\widetilde{F}$ is as in Equation 7.1.6. Moreover, the error threshold q_{crit} is,

$$q_{\text{crit}} = 1 - \left[2\frac{(d-1)}{(d-2)^2}\left(\sqrt{4 + \frac{(d-2)^2}{d-1}} - 2\right)\right]^{\frac{1}{N-1}}. \tag{7.1.8}$$

Observe from Equation 7.1.8 that the error threshold scales positively in the dimension, by a multiplicative factor, whereas the scaling with the node numbers is repressed by a power relationship. Together these relationships are in line with the scaling with d and N observed in Chapter 6. In Table 7.1 we tabulate the error threshold for various sets of dimension and node numbers. We expect that these gate error thresholds for binary-like GHZ type states purified by subroutine P1 within a restricted model of faulty two-qudit operations provide an upper bound to the error threshold for GHZ type states purified by the full protocol and under the more general gate error model with depolarizing noise. Although this is expected to be a rather loose upper bound due to the constraints imposed in the derivation, we expect the scaling with d and N indicated by the analytic results to be faithful because of the agreement with the scaling relationships observed for the error-less protocol in Chapter 6.

d	$N=3$	$N=4$	$N=5$	$N=6$
3	0.30	0.21	0.17	0.13
5	0.33	0.24	0.18	0.15
7	0.36	0.26	0.20	0.16
11	0.40	0.29	0.22	0.18

Table 7.1: Gate error thresholds q_{crit} for various qudit dimensions and GHZ state node numbers, as given by Equation 7.1.8.

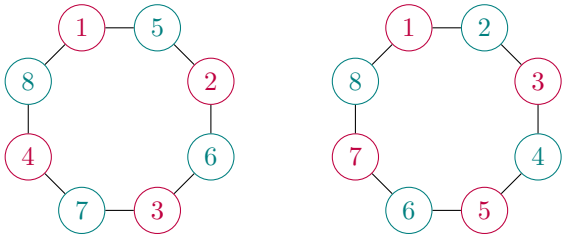

(a) Previous numbering convention: All nodes from V_A numbered before those in V_B.

(b) New numbering convention: Sequential, starting with V_A.

Figure 7.1: Graph corresponding to a closed linear cluster state with 8 vertices. Deletion of the edge between the 1^{st} and 8^{th} vertices would return the graph of the 8 node linear cluster state of Figure 4.2a.

7.1.2. Closed linear cluster states

Closed linear cluster states are linear cluster states that have one extra edge, joining the two terminal vertices of the state. The closure changes the topology of the graphs so that they are only two-colorable if there is an even number of vertices; for this reason we restrict to considering an even number of vertices $N = 2M$, so that M characterizes the number of vertices in each vertex subset, $|V_A| = |V_B| = M$. Figure 7.1 shows an example of a closed linear cluster state with 8 vertices. We look at closed linear cluster states for the analytical analysis because they have constant degree and no boundary nodes. For ease of analysis, in this section we change the numbering scheme for the nodes of a two-colorable graph state, so that vertices are numbered sequentially and odd numbered nodes correspond to vertex subset V_A, while even numbered nodes correspond to vertex subset V_B, see Figure 7.1b. The analysis differs slightly depending on whether M is even or odd, so we here choose to present results in the case that M is odd.

We consider binary-like mixture type states belonging to the one parameter family,

$$\rho_A(x) = x\,|\Psi_{\mathbf{0},\mathbf{0}}\rangle\langle\Psi_{\mathbf{0},\mathbf{0}}| + (1-x)\frac{\mathbb{1}_{V_A}}{d^M}, \tag{7.1.9}$$

where $\mathbb{1}_{V_A} = \sum_{\boldsymbol{\mu}_A} |\Psi_{\boldsymbol{\mu}_A,\mathbf{0}}\rangle\langle\Psi_{\boldsymbol{\mu}_A,\mathbf{0}}|$. Notice that $\rho_A(x)$ has rank $d^M = d^{N_A}$, since $\boldsymbol{\mu}_A \in \mathbb{F}_d^M$, and that the initial fidelity of the state to the perfect graph state is $F = x + \frac{1-x}{d^M}$.

To determine the effect of purification subroutine P1 with faulty two-qudit operations we make use of Proposition 7.1 so that we only need to determine how the sequence of error processes $\mathcal{M}_{2M} \circ \cdots \circ \mathcal{M}_2(\cdot)$ acts on $\rho_A(x)$, where $\mathcal{M}_j$ is as in

Equation 7.1.2. Once the action of the error processes is established we apply the perfect subroutine P1 on binary-like inputs, dictated by Equation 6.1.2. The effect of a single error process from a faulty operation is summarized in the following Proposition 7.3, which is proven in Appendix E.

Proposition 7.3. A single error process $\mathcal{M}_j$, given by Equation 7.1.2, preserves the identity on subset V_A, $\mathcal{M}_j(\mathbb{1}_{V_A}) = \mathbb{1}_{V_A}$, and acts on binary-like closed linear cluster graph basis states as,

$$\mathcal{M}_j\Big(\left|\Psi_{\boldsymbol{\mu}_A,\mathbf{0}}\right\rangle\left\langle\Psi_{\boldsymbol{\mu}_A,\mathbf{0}}\right|\Big) = (1-p)\left|\Psi_{\boldsymbol{\mu}_A,\mathbf{0}}\right\rangle\left\langle\Psi_{\boldsymbol{\mu}_A,\mathbf{0}}\right| + \frac{p}{d-1}\sum_{k=1}^{d-1}\left|\Psi_{\boldsymbol{\mu}_A\oplus k[\boldsymbol{e}_{j-1}\oplus\boldsymbol{e}_{j+1}],\mathbf{0}}\right\rangle\left\langle\Psi_{\boldsymbol{\mu}_A\oplus k[\boldsymbol{e}_{j-1}\oplus\boldsymbol{e}_{j+1}],\mathbf{0}}\right|, \quad (7.1.10)$$

where $(1-p) = \frac{1}{d}\big((d-1)(1-q)+1\big)$.

Having characterized the action of a single error process we see that the sequence of error processes $\mathcal{M}_{2M}\circ\cdots\circ\mathcal{M}_2(\cdot)$ will leave $\mathbb{1}_{V_A}$ fixed, and it remains only to to calculate the effect on the $|\Psi_{\mathbf{0},\mathbf{0}}\rangle$ part of the input state $\rho_A(x)$, which we do in Appendix E, by iterative application of Equation 7.1.10.

Proposition 7.4. The effect of the error sequence $\mathcal{M}_{2M}\circ\cdots\circ\mathcal{M}_2(\cdot)$ on the perfect closed linear cluster state, $|\Psi_{\mathbf{0},\mathbf{0}}\rangle$ with $N = 2M$ vertices, where M is odd, can be described using a subset of the basis states $\{|\Psi_{\boldsymbol{\mu}_A,\mathbf{0}}\rangle\}$. Define $\{|\Phi_K\rangle\}$ to be the subset of basis states[2] with the phase type errors Z^{l_1}, Z^{l_2}, $\cdots$, Z^{l_K} on K pairs of next nearest neighbor vertices, such that the error Z^{l_i} applies to both nodes of the i-th pair of next nearest neighbor nodes. Furthermore, if we write a sum over $b_{M,K}\left|\Phi_K\right\rangle\left\langle\Phi_K\right|$, where $b_{M,K} = \binom{M}{K}(d-1)^K$, it is to be interpreted as the sum of all possible samples of states from $\{|\Phi_K\rangle\}$, of which there are $b_{M,K}$. In this notation, the effect of the error sequence is,

$$\mathcal{M}_{2M}\circ\cdots\circ\mathcal{M}_2\Big(\left|\Psi_{\mathbf{0},\mathbf{0}}\right\rangle\left\langle\Psi_{\mathbf{0},\mathbf{0}}\right|\Big) = (1-p)^M\left|\Psi_{\mathbf{0},\mathbf{0}}\right\rangle\left\langle\Psi_{\mathbf{0},\mathbf{0}}\right| + \sum_{K=1}^{M}(1-p)^{M-K}\Big(\frac{p}{d-1}\Big)^K b_{M,K}\left|\Phi_K\right\rangle\left\langle\Phi_K\right|. \quad (7.1.11)$$

Corollary 7.2. The state resulting from the sequence of error processes $\mathcal{M}_{2M}\circ\cdots\circ\mathcal{M}_2(\cdot)$ on an input state of the type in Equation 7.1.9, with M odd is,

$$\mathcal{M}_{2M}\circ\cdots\circ\mathcal{M}_2\Big(\rho_A(x)\Big) = x\left[(1-p)^M\left|\Psi_{\mathbf{0},\mathbf{0}}\right\rangle\left\langle\Psi_{\mathbf{0},\mathbf{0}}\right| + \sum_{K=1}^{M}(1-p)^{M-K}\Big(\frac{p}{d-1}\Big)^K b_{M,K}\left|\Phi_K\right\rangle\right] + (1-x)\frac{\mathbb{1}_{V_A}}{d^M}. \quad (7.1.12)$$

[2] For example: $\{|\Phi_0\rangle\} = \{|\Psi_{\mathbf{0},\mathbf{0}}\rangle\}$,
$\{|\Phi_1\rangle\} = \Big\{\left|\Psi_{l_1[\boldsymbol{e}_1\oplus\boldsymbol{e}_3],\mathbf{0}}\right\rangle, \left|\Psi_{l_1[\boldsymbol{e}_3\oplus\boldsymbol{e}_5],\mathbf{0}}\right\rangle, \cdots, \left|\Psi_{l_1[\boldsymbol{e}_{2M-1}\oplus\boldsymbol{e}_1],\mathbf{0}}\right\rangle\Big\}$,
$\{|\Phi_2\rangle\} = \Big\{\left|\Psi_{l_1[\boldsymbol{e}_1\oplus\boldsymbol{e}_3]\oplus l_2[\boldsymbol{e}_3\oplus\boldsymbol{e}_5],\mathbf{0}}\right\rangle, \cdots, \left|\Psi_{l_1[\boldsymbol{e}_1\oplus\boldsymbol{e}_3]\oplus l_2[\boldsymbol{e}_{2M-1}\oplus\boldsymbol{e}_1],\mathbf{0}}\right\rangle, \cdots,$
$\left|\Psi_{l_1[\boldsymbol{e}_3\oplus\boldsymbol{e}_5]\oplus l_2[\boldsymbol{e}_5\oplus\boldsymbol{e}_7],\mathbf{0}}\right\rangle, \cdots, \left|\Psi_{l_1[\boldsymbol{e}_3\oplus\boldsymbol{e}_5]\oplus l_2[\boldsymbol{e}_{2M-1}\oplus\boldsymbol{e}_1],\mathbf{0}}\right\rangle, \cdots\Big\}$

Recall from Equation 6.1.1 that a binary-like mixture state can be completely described in terms of the coefficients $\lambda_{\boldsymbol{\mu}_A,\mathbf{0}}$ of the binary-like basis vectors $|\Psi_{\boldsymbol{\mu}_A,\mathbf{0}}\rangle$. To determine explicitly the coefficients of the state in Equation 7.1.12, we ask whether the sum over all $b_{M,K}$ states $|\Phi_K\rangle$ plus the state $|\Psi_{\mathbf{0},\mathbf{0}}\rangle$ covers all states from $\mathbb{1}_{V_A}$. Note that we can absorb $|\Psi_{\mathbf{0},\mathbf{0}}\rangle$ into the sum, since it is the unique state $|\Phi_0\rangle$. Each basis state in the sum occurs only once. The number of basis states in the sum is,

$$\sum_{K=0}^{M} \binom{M}{K}(d-1)^K = \sum_{K=0}^{M} \binom{M}{K}(d-1)^K 1^{M-K} = d^M, \tag{7.1.13}$$

where we used the binomial theorem to carry out the summation. The meaning of the calculation is that there are d^M unique binary-like basis states, hence they cover all states from $\mathbb{1}_{V_A}$. Overall then, the coefficients of the state $\mathcal{M}_{2M}\circ\cdots\circ\mathcal{M}_2\Big(\rho_A(x)\Big)$ can be written as,

$$\lambda'_{M,K} = x(1-p)^{M-K}\Big(\frac{q}{d-1}\Big)^K + \Big(\frac{1-x}{d^M}\Big),\ K\in\{0,1,\cdots,M\}, \tag{7.1.14}$$

each of which occurs $b_{M,K} = \binom{M}{K}(d-1)^K$ times. The coefficients of the state resulting from the faulty purification subroutine P1 acting on input state $\rho_A(x)$ can then be determined by applying the map in Equation 6.1.2 to the coefficients. The fidelity of the output state is,

$$\begin{aligned}\widetilde{F} &= \frac{(\lambda'_{M,0})^2}{\sum_{K=0}^{M} b_{M,K}(\lambda'_{M,K})^2} \\ &= \frac{\Big(x(1-p)^M + \Big(\frac{1-x}{d^M}\Big)\Big)^2}{\sum_{K=0}^{M} b_{M,K}\left[x(1-p)^{M-K}\Big(\frac{p}{d-1}\Big)^K + \Big(\frac{1-x}{d^M}\Big)\right]^2}.\end{aligned} \tag{7.1.15}$$

To achieve purification, it is necessary that $\widetilde{F} > F$. To determine the critical values for p and x, that is the values which define the boundary of the purification regime, we look for fixed points in of the fidelity, $\widetilde{F}(x,p) = F(x)$. Recall that the parameter p relates to the gate error parameter through $(1-p) = \frac{1}{d}\big((d-1)(1-q)+1\big)$.

When purification subroutine $P1$ with faulty two-qudit operations of the form described by Equations 7.1.1 and 7.1.2 is used to purify states of the form given in Equation 7.1.9, the maximum (x_+) and minimum (x_-) state parameters, which define the maximum reachable fidelity and minimal initial required fidelity, are,

$$x_\pm = \frac{BC - A^2 \pm \sqrt{\Delta}}{2C(B-1)}, \tag{7.1.16}$$

where $\Delta = \big(A^2 - BC\big)^2 + 4C\big(1-B\big)\big[2AB - B\big(1-B\big)\big]$, and we define the functions,

$$\begin{aligned} A(p,d) &:= (1-p)^M - \frac{1}{d^M}, \\ B(d) &:= \frac{1}{d^M}, \\ C(p,d) &:= \big[(1-p)^2 + \frac{p^2}{d-1}\big]^M - \frac{1}{d^M}. \end{aligned}$$

See Appendix E for the derivation of Equation 7.1.16. The critical parameter p_{crit}, which defines the critical gate error parameter q_{crit} through $(1-p) = \frac{1}{d}\big((d-1)(1-q)+1\big)$ is obtained by solving $\Delta = 0$ for p, which can be done numerically.

To get a sense for how the gate error threshold, q_{crit} depends on the qudit dimension, d, and number of nodes N of the closed linear cluster state, we study separately the scaling with N for a fixed dimension and the scaling with d for a fixed number of nodes. In Section 6.3 we proposed that the amount of depolarizing noise that can be applied per qudit to a graph state depends primarily on the degree of the graph, and found that for linear cluster states, which always have degree 2, the error tolerance per qudit is independent of N. According to this model, we expect to see a similar insensitivity to increasing N reflected in the gate error threshold. Figure 7.2a offers evidence in support of the relative insensitivity to increasing N of the gate error threshold for closed linear cluster states, especially in the large N regime. This relationship contrasts the sharp suppression of error tolerance with increasing N observed for GHZ type states, in Section 7.1.1.

Also made accessible by the analytic results is the scaling of gate error tolerance with qudit dimension in the large dimension regime. Figure 7.2b demonstrates the scaling with dimension for a closed linear cluster state with $M = 53$ ($N = 2M = 106$), for prime qudit dimensions up to 97. In the low dimension regime, where $d \lesssim 20$ there is a sizeable benefit to increasing the dimension, in terms of the improved error threshold. For dimensions across the mid range $20 \lesssim d \lesssim 60$ and into the large dimension range $d \gtrsim 60$, the increase in error tolerance with dimension slowly approaches saturation. This suggests that when there exists an experimental tradeoff between costs of working with states of larger dimension (examples: lower fidelity operations, operations requiring longer amounts of time, etc.) and the benefit of higher error thresholds, the greatest net benefit likely exists in the range $3 < d < 20$.

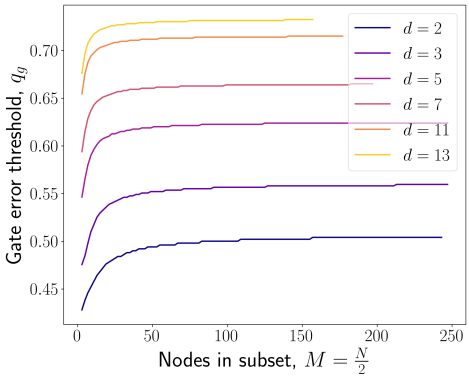

(a) Gate error threshold scaling with node number, $N = 2M$.

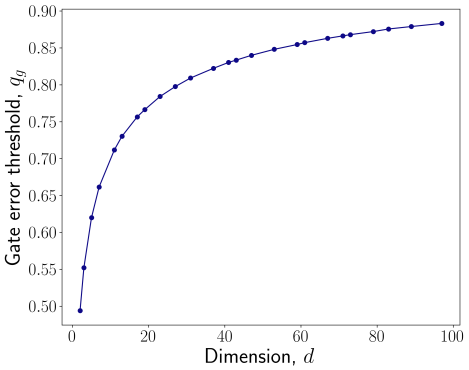

(b) Gate error threshold scaling with qudit dimension, and $M = 53$ fixed.

Figure 7.2: Scaling of the gate error threshold value for purification of closed linear cluster type graph states in a binary-like mixture (Equation 7.1.9), using subroutine P1 with faulty two qudit operations as modelled by Equations 7.1.1, 7.1.2. In (b) the points are unevenly spaced because only prime dimensions are plotted.

7.2. Numerical analysis

By numerically simulating[3] the purification protocol it is possible to examine the gate error tolerance under a depolarization error model, which constitutes the most general uncorrelated error model. Moreover, in the numerical analysis it is possible to consider depolarized input states, the purification of which are examined for the error-free protocol in Section 6.3. The numerical analysis allows a more realistic look at the scaling of gate error thresholds with dimension and node number than is offered by the upper bounds derived in the previous section. The drawback is that the numerical approach is computationally heavy and large dimensions and node numbers remain inaccessible with this technique[4]. In Appendix F.2 we assess the validity of the numerics in the qubit case by comparison to the results published in [25].

For a TCGS G, label the nodes in subset V_A of size $N_A = |V_A|$ by $\{a_1, a_2, \cdots, a_{N_A}\}$ and the nodes in V_B of size $N_B = |V_B|$ by $\{b_1, b_2, \cdots, b_{N_B}\}$. As in Section 6.3,

[3] The software developed for simulating the protocol with two-qudit gate errors is publicly available on GitHub [59].

[4] Working computer has the following specs:
CPU: Intel Xeon Gold 6230 @ 80x 3.9GHz
RAM: 59260MiB / 193114MiB.
Example completion times for data points in Figure 7.3a: ($d = 7$, $N = 2$, time= 131 seconds), ($d = 7$, $N = 3$, time= 3.1 hours), ($d = 7$, $N = 4$, time= 184 hours).
Each simulation used multiprocessing across an average of 20 of the available 80 cores.

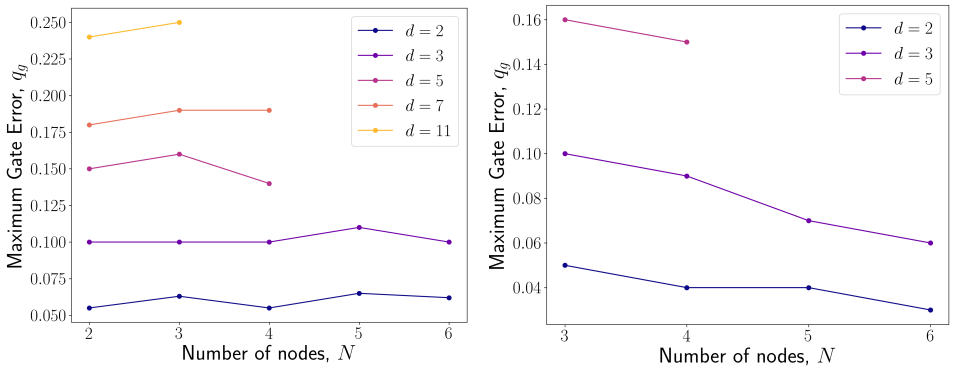

(a) Linear cluster state.

(b) GHZ type state.

Figure 7.3: Gate error threshold vs. number of nodes for (a) linear cluster type states and (b) GHZ type state, for various dimensions of the state's qudits.

we consider depolarized input states, which result from sending each node of the perfect TCGS through a depolarization channel,

$$\rho(q_s) = \mathcal{E}_{a1} \circ \cdots \mathcal{E}_{a_{N_A}} \circ \mathcal{E}_{b1} \circ \cdots \circ \mathcal{E}_{b_{N_B}} \left(|\Psi_{\mathbf{0}}\rangle \langle \Psi_{\mathbf{0}}|_G \right), \tag{7.2.1}$$

where each $\mathcal{E}_j$ is given by Equation 2.2.6, with depolarization parameter q_s. We study the effect of using an imperfect realization of the purification protocol described in Section 5.2, where all of the two qudit gates in each of subroutines P1 and P2 (see Section 5.1) are replaced with faulty operations, as modelled by Equation 7.0.1, where each $\mathcal{E}_j$ is given by Equation 2.2.6, with error parameter q_g. In Figure 7.3 we plot the calculated error thresholds for both linear cluster and GHZ type states of low node numbers. The results indicate very favorable scaling of the error tolerance with qudit dimension, as each increment from one prime dimension to the next yields an increase of several percent in the error threshold. In an experimental setting, these results may serve as one possible benchmark of whether two qudit operations are of high enough fidelity to be useful in applications. Moreover, they may serve as an indicator of whether there is an experimental advantage to working with states of higher dimension; an advantage may exist if for a particular dimension the difference between the gate error levels and the threshold value exceeds the difference obtained for qubit systems.

Another question addressed by the numerical analysis is whether the scaling of the gate error thresholds with the node number is consistent with the model that the error threshold for states of fixed qudit dimension only depends on the degree of the graph. In Figure 7.3 we see that the numeric results for states of dimension $d = 2$ and $d = 3$, suggest that the model remains consistent, as for linear cluster states

(which have constant degree) the threshold is essentially constant with N, whereas for GHZ type states (where the degree is $N-1$) the error threshold decreases as N increases. It is also worth noting that the qualitative nature of the scaling of error threshold with node number matches that of the analytically derived upper bounds, suggesting that the analytic bound meaningfully captures the qualitative trends.

8

Conclusions and Outlook

We have proposed a recurrence based purification protocol for TCGS where the underlying quantum systems are qudits of prime dimension and analyzed from a variety of angles how the system dimension and number of nodes in a state impact the performance of the protocol. The proposed protocol is an extension of the work in [25], in which the qubit case was studied. In Chapter 5 we detail the protocol and in Chapter 6 we study the performance of the protocol in the absence of errors. In the error-less case the minimum fidelity of input states, which is the primary metric for characterizing this scenario, is found to decrease dramatically with increasing system dimension. In Section 6.1 we presented a conceptual model explaining the improvement in performance of the protocol with increasing dimension, which relies on the interplay of entropy and information in quantum mechanics. In higher dimensions a greater amount of information is learned during the measurement step of each purification subroutine, leading to a greater decrease in the entropy of the state. In Section 6.3 the relation between node number and the maximum amount of noise tolerated per node of a TCGS was found to depend on the topology of the TCGS under consideration. We extended an existing model from the qubit case which attributes the maximum error tolerance per node of a graph state to the degree of the graph state, in order to explain the dependence on graph topology. In the context of the error-less protocol we have demonstrated using linear cluster states that for a given per-qudit noise level and target fidelity, there is a practical advantage to using the protocol to purify states of higher dimension (Section 6.3); we found that the expected number of attempts required to complete the protocol could drop by several orders of magnitude when increasing the qudit dimension. In an experimental setting, such a practical advantage will of course have to be weighted against any experimental costs incurred by working with higher dimensional systems.

In Chapter 7 we obtained both analytic and numeric results indicating the error tolerance of the protocol with respect to faulty two-qudit operations, and we have studied how this tolerance depends on qudit dimension and state node number. The analytic results, derived in Section 7.1 under a restricted error model for the two-

qudit operations and considering a restricted class of input states, can reasonably be expected to provide an upper bound to the error tolerance under more general error models and with arbitrary input states. A study of the error tolerance in the regimes of high qudit dimension ($d \gtrsim 20$) and large node numbers ($N \gtrsim 10$) was made possible by the analytic results. The upper bound in the scaling of error tolerance with dimension indicates that while there remains an incentive (in the form of improved error tolerance) to increasing system dimension in the high dimensional regime, the benefits of increasing dimension are greatest in the low dimensional regime ($2 \lesssim d \lesssim 20$). In the high dimensional regime the magnitude of the slope of the upper bound on gate error threshold versus dimension decreases towards zero, despite remaining always positive; this indicates saturation of the error threshold for higher dimensions. The main result of the protocol performance analysis is the numerically determined favorable scaling of the gate error threshold with dimension (Section 7.2). We observe by studying several dimensions $(2, 3, 5, 7, 11)$ that in each case a gain of several percentage points in the gate error threshold is possible by increasing the dimension. In the numerical study we have considered white noise in the gate error model and depolarized input states. The primary benefit of the larger error threshold is that higher dimensional states can allow successful completion of the protocol when faced with gate error levels that would cause the protocol to fail for lower dimensions. The secondary benefit is that for a given gate error level the protocol will work better for higher dimensional states, since the protocol will be operating further from the error threshold, and the performance of the protocol near the error threshold tends to deteriorate severely. In terms of the scaling with node number, both the analytic and numeric results are consistent with the model suggesting that the error tolerance per node of a graph state depends entirely upon the topology of the graph.

There is in principle no reason why the protocol presented here cannot be extended to apply to TCGS on qudits with prime-power dimensions (as opposed to only prime dimensions, considered here). To do so would require properly accounting for the $N < K < 2N$ stabilizer generators of an N qudit TCGS and reformulating the analysis, especially of Section 4.3, in terms of these stabilizer generators. A promising direction for future work on this topic would be to present a recurrence type purification protocol for arbitrary graph states. In the qubit case, one such protocol exists [48] which is an extension of the protocol for TCGS [25] and which uses noisy TCGS as resources. Another interesting direction would be to develop a hashing type purification protocol for TCGS, possibly by extending the protocol for GHZ type states discussed in [51]. A hashing type protocol would be expected to function deterministically and achieve a finite yield and generally higher output fidelities as compared with recurrence type purification. A drawback of hashing

type purification is that input states of higher fidelity are typically required.

The increased error tolerances for states of higher dimension observed in the analysis of this protocol adds to a growing body of research [10, 11, 12, 13, 14, 15, 16, 17] demonstrating the advantages of using qudit systems as the basis of quantum information, communication and computing protocols. Practically, the advantages promised by higher dimensional systems have to be balanced against possible costs of working with these systems. One example is that the achievable gate error level for higher dimensional systems may exceed the level achievable for qubits. To the best of our knowledge the question of how to experimentally realize generalizations of the CNOT operation for $d > 2$ remains an open problem. When techniques for executing these operations are eventually developed, the numerically calculated gate error thresholds for the protocol presented here may serve as one benchmark of the performance of these operations. Specifically, if these operations for a given dimension can be demonstrated to work with error levels below those presented here, then the gates will be useful for at least one type of quantum information protocol. If the error levels are significantly below the threshold level, then it will be reasonable to expect working with higher dimensional systems to offer a practical advantage.

A

Properties of Weyl operators

Lemma 2.1. [28] For any two Weyl operators $W_{\boldsymbol{v}}$ and $W_{\boldsymbol{w}}$ with $\boldsymbol{v}, \boldsymbol{w} \in \mathbb{Z}^{2N}$ the following properties hold:

(i) $W_{\boldsymbol{v}} W_{\boldsymbol{w}} = \tau^{2[\boldsymbol{w},\boldsymbol{v}]} W_{\boldsymbol{w}} W_{\boldsymbol{v}} = \omega^{[\boldsymbol{w},\boldsymbol{v}]} W_{\boldsymbol{w}} W_{\boldsymbol{v}}$, these are the commutation relations for Weyl operators.

(ii) $\left[W_{\boldsymbol{v}}, W_{\boldsymbol{w}}\right] = 0$ if and only if $[\boldsymbol{v}, \boldsymbol{w}] = 0 \bmod d$. This is a corollary of (i).

(iii) $W_{\boldsymbol{v}}^t = W_{t\boldsymbol{v}}$ for $t \in \mathbb{Z}$. In particular, $W_{\boldsymbol{v}}^\dagger = W_{-\boldsymbol{v}}$.

(iv) The order of $W_{\boldsymbol{v}}$ divides d.

Proof.
Recall that $\tau := (-1)^d e^{\frac{i\pi}{d}} = e^{i\pi \frac{d^2+1}{d}}$.

(i) The commutation relations follow directly from Equation 2.1.12,

$$\begin{aligned} W_{\boldsymbol{v}} W_{\boldsymbol{w}} &= \tau^{-[\boldsymbol{v},\boldsymbol{w}]} W_{\boldsymbol{v}+\boldsymbol{w}} \\ &= \tau^{[\boldsymbol{w},\boldsymbol{v}]} W_{\boldsymbol{w}+\boldsymbol{v}} \\ &= \tau^{[\boldsymbol{w},\boldsymbol{v}]} \tau^{[\boldsymbol{w},\boldsymbol{v}]} W_{\boldsymbol{w}} W_{\boldsymbol{v}} \\ &= \tau^{2[\boldsymbol{w},\boldsymbol{v}]} W_{\boldsymbol{w}} W_{\boldsymbol{v}}. \end{aligned} \tag{A.0.1}$$

(ii) ($\Rightarrow$) Assume $\left[W_{\boldsymbol{v}}, W_{\boldsymbol{w}}\right] = 0$. Making use of the commutation relations in (i),

$$W_{\boldsymbol{v}} W_{\boldsymbol{w}} = W_{\boldsymbol{w}} W_{\boldsymbol{v}} \;\Rightarrow\; \omega^{[\boldsymbol{w},\boldsymbol{v}]} = 1. \tag{A.0.2}$$

In turn, this implies that $[\boldsymbol{w}, \boldsymbol{v}] = 0 \bmod d$ and hence also $[\boldsymbol{v}, \boldsymbol{w}] = 0 \bmod d$.

($\Leftarrow$) Assume $[\boldsymbol{v}, \boldsymbol{w}] = 0 \bmod d$. Then, $\omega^{[\boldsymbol{w},\boldsymbol{v}]} = 1$. Using the commutation relations in (i), it then follows that $\left[W_{\boldsymbol{v}}, W_{\boldsymbol{w}}\right] = 0$.

A

(iii) Here, it is helpful to again recall Equation 2.1.12. A single application of the relation yields,

$$W_{t\boldsymbol{v}} = W_{\boldsymbol{v}+(t-1)\boldsymbol{v}} = \tau^{[\boldsymbol{v},\boldsymbol{v}]} W_{\boldsymbol{v}} W_{(t-1)\boldsymbol{v}} = W_{\boldsymbol{v}} W_{(t-1)\boldsymbol{v}}. \tag{A.0.3}$$

Iterated application of Equation 2.1.12 yields the desired result.

(iv) In lieu of proving explicitly this point, we will state exactly the order of $W_{\boldsymbol{v}}$ for all of the cases of interest to this work, which is given in Corollary 11a of [28]. Recall that D denotes the order of τ, which is d in the case that d is odd, and $2d$ in the case that d is even. For all cases of interest we consider $\boldsymbol{v} \in \mathbb{Z}_D^m$, where $m = 2N$. First, we establish some notation. Define the *harmonic number* $\eta(\boldsymbol{v}) = \gcd(v_1, v_2, \cdots, v_m, d)$ of $\boldsymbol{v}$. If $\eta(\boldsymbol{v}) = 1$, we say that $\boldsymbol{v}$ is fundamental.

By Corollary 11a of [28], for any $\boldsymbol{v} \in \mathbb{Z}_D^{2N}$, the order of $W_{\boldsymbol{v}}$ is $\frac{d}{\eta(\boldsymbol{v})}$. In particular, $W_{\boldsymbol{v}}$ has order 1 if and only if $\boldsymbol{v}$ is fundamental.

□

Lemma 2.2. [28] For all $\boldsymbol{v}, \boldsymbol{w} \in \mathbb{Z}^{2N}$ we have $W_{\boldsymbol{v}} \propto W_{\boldsymbol{w}}$ if and only if $\boldsymbol{w} = \boldsymbol{v} + d \cdot \boldsymbol{x}$ for some $\boldsymbol{x} \in \mathbb{Z}^{2N}$, in which case

$$W_{\boldsymbol{w}} = (-1)^{(d+1)[\boldsymbol{x},\boldsymbol{v}]} W_{\boldsymbol{v}}. \tag{2.1.13}$$

In particular, $W_{\boldsymbol{w}} = W_{\boldsymbol{v}}$ if $\boldsymbol{w} = \boldsymbol{v} \bmod D$.

Proof.
($\Rightarrow$) Suppose that $W_{\boldsymbol{w}} \propto W_{\boldsymbol{v}}$, with proportionality constant α, so that $W_{\boldsymbol{w}} = \alpha W_{\boldsymbol{v}}$. We proceed by comparing the actions of $W_{\boldsymbol{w}}$ and $\alpha W_{\boldsymbol{v}}$ on an element of the basis for the N qudit Hilbert space, $\mathcal{H}_{d,N}$, $|\boldsymbol{i}\rangle = |i_1, \cdots, i_N\rangle$ with $i_j \in \mathbb{Z}_d$. Denote the parts of $\boldsymbol{v}, \boldsymbol{w} \in \mathbb{Z}^{2N}$ by $\boldsymbol{v} = (\boldsymbol{v}_1, \boldsymbol{v}_2)$, $\boldsymbol{w} = (\boldsymbol{w}_1, \boldsymbol{w}_2)$.

$$\begin{aligned} W_{\boldsymbol{w}} |\boldsymbol{i}\rangle &= \tau^{\boldsymbol{w}_1 \cdot \boldsymbol{w}_2} Z^{\boldsymbol{w}_1} X^{\boldsymbol{w}_2} |\boldsymbol{i}\rangle \\ &= \tau^{2\boldsymbol{w}_1 \cdot \boldsymbol{i}} \tau^{\boldsymbol{w}_1 \cdot \boldsymbol{w}_2} |\boldsymbol{i} \oplus \boldsymbol{w}_2\rangle \end{aligned} \tag{A.0.4}$$

Similarly,

$$\alpha W_{\boldsymbol{v}} |\boldsymbol{i}\rangle = \alpha \tau^{2\boldsymbol{v}_1 \cdot \boldsymbol{i}} \tau^{\boldsymbol{v}_1 \cdot \boldsymbol{v}_2} |\boldsymbol{i} \oplus \boldsymbol{v}_2\rangle . \tag{A.0.5}$$

Following the hypothesis, we equate A.0.4 and A.0.5. There are two implications of this equality. First,

$$\boldsymbol{i} \oplus \boldsymbol{w}_2 = \boldsymbol{i} \oplus \boldsymbol{v}_2 \bmod d$$

$$\Rightarrow \boldsymbol{w}_2 = \boldsymbol{v}_2 + d\boldsymbol{x}_2, \text{ for some } \boldsymbol{x}_2 \in \mathbb{Z}^N. \tag{A.0.6}$$

The second implication is that

$$\tau^{2\boldsymbol{w}_1\cdot\boldsymbol{i}} = \tau^{2\boldsymbol{v}_1\cdot\boldsymbol{i}} \bmod d$$

$$\Rightarrow \boldsymbol{w}_1 = \boldsymbol{v}_1 + d\boldsymbol{x}_1, \text{ for some } \boldsymbol{x}_1 \in \mathbb{Z}^N. \tag{A.0.7}$$

Writing now $\boldsymbol{x} = (\boldsymbol{x}_1, \boldsymbol{x}_2)$, it follows directly from Equation A.0.7 and A.0.6 that $\boldsymbol{w} = \boldsymbol{v} + d\boldsymbol{v}$. Before considering the other direction, it is helpful to continue by determining the proportionality constant α. To do so, we again equate A.0.4 and A.0.5, this time making use of the relations in A.0.7 and A.0.6,

$$\tau^{2(\boldsymbol{v}_1+d\boldsymbol{x}_2)\cdot\boldsymbol{i}}\tau^{(\boldsymbol{v}_1+d\boldsymbol{x}_1)\cdot(\boldsymbol{w}_2+d\boldsymbol{x}_2)}\,|\boldsymbol{i}\oplus\boldsymbol{v}_2\rangle = \alpha\tau^{2\boldsymbol{v}_1\cdot\boldsymbol{i}}\tau^{\boldsymbol{v}_1\cdot\boldsymbol{v}_2}\,|\boldsymbol{i}\oplus\boldsymbol{v}_2\rangle$$

$$\Rightarrow\ \tau^{(\boldsymbol{v}_1+d\boldsymbol{x}_1)\cdot(\boldsymbol{w}_2+d\boldsymbol{x}_2)} = \alpha\tau^{\boldsymbol{v}_1\cdot\boldsymbol{v}_2}. \tag{A.0.8}$$

More simplification to the equation for α is still possible. Recall that the order of τ is $D = d$ for odd d and $D = 2d$ for even d, so in any case $\tau^{2d} = 1$. Proceeding,

$$\begin{aligned}
\alpha &= \tau^{d(\boldsymbol{v}_1\cdot\boldsymbol{x}_2+\boldsymbol{v}_2\cdot\boldsymbol{x}_1+\boldsymbol{x}_1\cdot d\boldsymbol{x}_2)} \\
&= (-1)^{(d^2+1)(\boldsymbol{v}_1\cdot\boldsymbol{x}_2+\boldsymbol{v}_2\cdot\boldsymbol{x}_1)}(-1)^{(d^2+1)d(\boldsymbol{x}_1\cdot\boldsymbol{x}_2)} \\
&= (-1)^{(d+1)(\boldsymbol{v}_1\cdot\boldsymbol{x}_2+\boldsymbol{v}_2\cdot\boldsymbol{x}_1)} \\
&= (-1)^{(d+1)(\boldsymbol{v}_1\cdot\boldsymbol{x}_2-\boldsymbol{v}_2\cdot\boldsymbol{x}_1+2\boldsymbol{v}_2\cdot\boldsymbol{x}_1)} \\
&= (-1)^{(d+1)[\boldsymbol{x},\boldsymbol{v}]}.
\end{aligned} \tag{A.0.9}$$

In the third line we made use of the fact that $(d^2+1)d$ has even parity, regardless of the parity of d, and also that (d^2+1) has the same parity as $(d+1)$, regardless of the parity of d. Overall then,

$$\alpha = (-1)^{(d+1)[\boldsymbol{x},\boldsymbol{v}]}. \tag{A.0.10}$$

($\Leftarrow$) The second direction follows very simply, making use of the previous derivation of α. Assume that $\boldsymbol{w} = \boldsymbol{v} + d\boldsymbol{x}$. Then, the expansion of $W_{\boldsymbol{w}}$ is,

$$\begin{aligned}
W_{\boldsymbol{w}} &= \tau^{-(\boldsymbol{v}_1\cdot\boldsymbol{v}_2+\boldsymbol{v}_1\cdot d\boldsymbol{x}_2+\boldsymbol{v}_2\cdot d\boldsymbol{x}_1+d\boldsymbol{x}_1\cdot d\boldsymbol{x}_2)}Z^{\boldsymbol{v}_1+d\boldsymbol{x}_1}X^{\boldsymbol{v}_2+d\boldsymbol{x}_2} \\
&= \tau^{-\boldsymbol{v}_1\cdot\boldsymbol{v}_2}\tau^{(\boldsymbol{v}_1\cdot d\boldsymbol{x}_2+\boldsymbol{v}_2\cdot d\boldsymbol{x}_1+d\boldsymbol{x}_1\cdot d\boldsymbol{x}_2)}\tau^{-2(\boldsymbol{v}_1\cdot d\boldsymbol{x}_2+\boldsymbol{v}_2\cdot d\boldsymbol{x}_1+d\boldsymbol{x}_1\cdot d\boldsymbol{x}_2)}Z^{\boldsymbol{v}_1}X^{\boldsymbol{v}_2} \\
&= \tau^{-\boldsymbol{v}_1\cdot\boldsymbol{v}_2}\tau^{(\boldsymbol{v}_1\cdot d\boldsymbol{x}_2+\boldsymbol{v}_2\cdot d\boldsymbol{x}_1+d\boldsymbol{x}_1\cdot d\boldsymbol{x}_2)}Z^{\boldsymbol{v}_1}X^{\boldsymbol{v}_2} \\
&= \tau^{(\boldsymbol{v}_1\cdot d\boldsymbol{x}_2+\boldsymbol{v}_2\cdot d\boldsymbol{x}_1+d\boldsymbol{x}_1\cdot d\boldsymbol{x}_2)}W_{\boldsymbol{v}} \\
&= \alpha W_{\boldsymbol{v}}.
\end{aligned} \tag{A.0.11}$$

In the last line of the proof, we made use of Equation A.0.9. □

B

Yield calculation for recurrence protocols

Suppose that there are N parties who can undertake a repeatable, distributed quantum state preparation procedure, which allows them to prepare noisy copies of their targeted entangled state. These parties may decide that to purify their noisy states they will use a recurrence based purification protocol, and perform a sequence of I subroutine iterations in total.

Each successful subroutine has a yield of one half, since two copies are taken as input and one purified copy is the output. Since each iteration may have a different success probability, denote by p_i the probability that the i-th iteration in the sequence succeeds. The number of attempts required to successfully complete a single subroutine iteration follows a geometric distribution [58] with probability p_i. From the properties of the geometric distribution, the expected number of attempts to complete an iteration is $\frac{1}{p_i}$. Hence the expected yield of iteration i is $Y_i = \frac{p_i}{2}$. In order to carry out the purification, all iterations must be repeated with success enough times to produce the purified input states needed as input for subsequent iterations. Moreover, the full chain of iterations needs to be completed sequentially and thus failure may require restarting. The yield for the protocol can therefore be written

$$Y = (\frac{p_1}{2})^{2^{I-1}} \cdot (\frac{p_2}{2})^{2^{I-2}} \cdots (\frac{p_{I-1}}{2})^2 \cdot (\frac{p_I}{2}). \tag{B.0.1}$$

Notice that since p_i is bounded between zero and 1, $\frac{p_i}{2} < 1 \ \forall \ i$, and hence the yield is strictly less than 1. To calculate an upper bound, determine $p_{\max} := \max(p_1,\ p_2,\ \cdots,\ p_I)$. Then, the following inequality holds

$$Y \leq (\frac{p_{\max}}{2})^{2^s}, \text{ with } s = \frac{I(I+1)}{2}. \tag{B.0.2}$$

It is then clear that the yield is zero in the asymptotic limit, since it tends to zero super-exponentially,

$$\lim_{I \to \infty} Y \to 0. \tag{B.0.3}$$

C

Local unitary equivalence of GHZ type states and star graph states

Here we demonstate that a GHZ type state can be transformed into a star graph state by applying a generalized Hadamard operation to all but the first qudit of a GHZ type state. The first qudit will be the central qudit from the star graph state following the transformation. Since the generalized Hadamard is a unitary operator, this verification establishes local unitary equivalence of the two states. The equivalence of different classes of graph states and the effect of local unitary or Clifford operations has been extensively studied in the qubit case [9, 60, 61].

To begin, we write down the star graph state explicitly, using Equation 4.1.4 and the adjacency matrix of the star graph. The entries of the adjacency matrix are given by,

$$\Gamma_{ij} = \begin{cases} 1, \text{ if } (i = 1 \text{ and } j \neq 1) \text{ or } (i \neq 1 \text{ and } j = 1) \\ 0, \text{ otherwise.} \end{cases} \tag{C.0.1}$$

Recall that the vectors $\{\boldsymbol{e}_j\}$ are the standard basis vectors of $\mathbb{Z}_{\mathrm{d}}^{\mathrm{N}}$, and that $\{\boldsymbol{q}\} = \mathbb{Z}_d^N$. The star graph state for N qudits of dimension d is then,

$$|\mathrm{Star}_{d,N}\rangle = \frac{1}{d^{\frac{N}{2}}} \sum_{\boldsymbol{q}} \omega^{\sum_{j=2}^{N} (\boldsymbol{q}\cdot\boldsymbol{e}_1)(\boldsymbol{q}\cdot\boldsymbol{e}_j)} |\boldsymbol{q}\rangle \,. \tag{C.0.2}$$

Next, we look at the result of applying a generalized Hadamard operator to the state $|\mathrm{GHZ}_{d,N}\rangle$, given by Equation 4.5.1. Recall the generalized Hadamard operator on qudits of dimension, given in Equation 2.1.6. The effect of applying the Hadamard

operator to the second qudit of the GHZ type state is,

$$H_2 \left|\mathrm{GHZ}_{d,N}\right\rangle = \frac{1}{\sqrt{d}} \frac{1}{\sqrt{d}} \sum_{x,y=0}^{d-1} \omega^{xy} (\mathbb{1} \otimes \left|x\right\rangle \left\langle y\right| \otimes \mathbb{1}^{\otimes(N-2)}) \sum_{k=0}^{d-1} \left|k\right\rangle^{\otimes N}$$
$$= \left(\frac{1}{\sqrt{d}}\right)^2 \sum_{x,k=0}^{d-1} \omega^{xk} \left|k\right\rangle \left|x\right\rangle \left|k\right\rangle^{\otimes(N-2)} . \tag{C.0.3}$$

The star graph is then obtained by applying Hadamard operators to the last $N-2$ qudits of the state in Equation C.0.3. The result is,

$$H_N \otimes \cdots \otimes H_3 \otimes H_2 \left|\mathrm{GHZ}_{d,N}\right\rangle = \left(\frac{1}{\sqrt{d}}\right)^N \sum_{k=0}^{d-1} \sum_{x_2=0}^{d-1} \sum_{x_3=0}^{d-1} \cdots \sum_{x_N=0}^{d-1} \omega^{k(x_2+x_3+\cdots+x_N)}$$
$$\cdot \left|k\right\rangle \left|x_2\right\rangle \left|x_3\right\rangle \cdots \left|x_N\right\rangle \tag{C.0.4}$$
$$= \frac{1}{d^{\frac{N}{2}}} \sum_{\boldsymbol{x}} \omega^{\sum_{j=2}^{N} (\boldsymbol{x}\cdot\boldsymbol{e}_1)(\boldsymbol{x}\cdot\boldsymbol{e}_j)} \left|\boldsymbol{x}\right\rangle . \tag{C.0.5}$$

That Equations C.0.2 and C.0.5 are the same completes the proof.

D

Proof of subroutine P1

The proof of protocol P1 relies upon the decomposition of the controlled lower and controlled raise gates in terms of phase and shift operators, detailed in Section 2.1. In tandem, we will also make use of the known action of phase and shift matrices on graph basis states, detailed in Section 4.3

Claim 1. The sequence of multilateral controlled raising and lowering operations $\big(\prod_{j=1}^{N_B} CX_d^-\big)\big(\prod_{i=1}^{N_A} CX_d^+\big)$, where the lowering operations work with state copy one as source and copy two as target, and the raising operations work with copy two as source and copy one as target, perform the following map:

$$|\Psi_{\boldsymbol{\mu}_A,\boldsymbol{\mu}_B}\rangle\,|\Psi_{\boldsymbol{\nu}_A,\boldsymbol{\nu}_B}\rangle \longmapsto \left|\Psi_{\boldsymbol{\mu}_A,\boldsymbol{\mu}_B\oplus(d-1)\boldsymbol{\nu}_B}\right\rangle|\Psi_{\boldsymbol{\nu}_A\oplus\boldsymbol{\mu}_A,\boldsymbol{\nu}_B}\rangle\,.$$

Proof. As a first step, we demonstrate how $CX_d^{+(v_{a_i})}$ (Equation 2.1.15) with state copy two as source and copy one as target acts on input state $|\Psi_{\boldsymbol{\mu}_A,\boldsymbol{\mu}_B}\rangle\,|\Psi_{\boldsymbol{\nu}_A,\boldsymbol{\nu}_B}\rangle$. In complement, we determine the action of $CX_d^{-(v_{b_j})}$ (Equation 2.1.17) with state copy one as source and two as target, on the same input state. Define $\boldsymbol{\Gamma}_{a_i}$ as the row of the adjacency matrix $\boldsymbol{\Gamma}$ of graph G which corresponds to the vertex $v_{a_i} \in V_A$ with all columns corresponding to V_A deleted. This means $\boldsymbol{\Gamma}_{a_i} \in \mathbb{F}_d^{\otimes N_B}$ and $\boldsymbol{\Gamma}_{\boldsymbol{a_i}} = [\Gamma_{a_ib_1}, \Gamma_{a_ib_2}, \cdots, \Gamma_{a_ib_{N_B}}]$. Similarly, $\boldsymbol{\Gamma}_{b_i}$ is the row of the adjacency matrix corresponding to vertex $v_{b_j} \in V_B$ with all the columns corresponding to vertices of V_B deleted. We will need the standard basis vectors $\boldsymbol{e}_{a_i}$, $\boldsymbol{e}_{b_j}$ of lengths N_A and N_B, respectively. To understand the following derivation, recall Equations 4.3.8 and 4.3.4. The controlled raising (lowering) operator acts on the two qudits corresponding to vertex v_{a_i} (v_{b_j}) of the pair of graph basis states as,

$$
\begin{aligned}
CX_d^{+(v_{a_i})}\left|\Psi_{\boldsymbol{\mu}_A,\boldsymbol{\mu}_B}\right\rangle\left|\Psi_{\boldsymbol{\nu}_A,\boldsymbol{\nu}_B}\right\rangle &= \frac{1}{d}\Big(\sum_{n=0}^{d-1}X^n\otimes\big[\sum_{m=0}^{d-1}\omega^{d-mn}Z^m\big]\Big)\left|\Psi_{\boldsymbol{\mu}_A,\boldsymbol{\mu}_B}\right\rangle\left|\Psi_{\boldsymbol{\nu}_A,\boldsymbol{\nu}_B}\right\rangle \\
&= \frac{1}{d}\sum_{n=0}^{d-1}\Big(\omega^{n(d-1)\mu_{a_i}}\left|\Psi_{\boldsymbol{\mu}_A,\boldsymbol{\mu}_B\oplus n(d-1)\boldsymbol{\Gamma}_{a_i}}\right\rangle\big(\sum_{m=0}^{d-1}\omega^{d-mn}\left|\Psi_{\boldsymbol{\nu}_A\oplus m\boldsymbol{e}_{a_i},\boldsymbol{\nu}_B}\right\rangle\big)\Big) \\
&= \frac{1}{d}\sum_{n,m=0}^{d-1}\Big(\omega^{n(d-1)\mu_{a_i}}\omega^{d-mn}\left|\Psi_{\boldsymbol{\mu_A},\boldsymbol{\mu}_B\oplus n(d-1)\boldsymbol{\Gamma}_{a_i}}\right\rangle\left|\Psi_{\boldsymbol{\nu}_A\oplus m\boldsymbol{e}_{a_i},\boldsymbol{\nu}_B}\right\rangle\Big) \qquad \text{(D.0.1)}
\end{aligned}
$$

$$
\begin{aligned}
CX_d^{-(v_{b_j})}\left|\Psi_{\boldsymbol{\mu}_A,\boldsymbol{\mu}_B}\right\rangle\left|\Psi_{\boldsymbol{\nu}_A,\boldsymbol{\nu}_B}\right\rangle &= \frac{1}{d}\Big(\sum_{n=0}^{d-1}\big[\sum_{m=0}^{d-1}\omega^{d-mn}Z^m\big]\otimes X^{n\cdot(d-1)}\Big)\left|\Psi_{\boldsymbol{\mu}_A,\boldsymbol{\mu}_B}\right\rangle\left|\Psi_{\boldsymbol{\nu}_A,\boldsymbol{\nu}_B}\right\rangle \\
&= \frac{1}{d}\sum_{n=0}^{d-1}\Big(\sum_{m=0}^{d-1}\big(\omega^{d-mn}\left|\Psi_{\boldsymbol{\mu}_A,\boldsymbol{\mu}_B\oplus m\boldsymbol{e}_{b_j}}\right\rangle\big)\omega^{n\nu_{b_j}}\left|\Psi_{\boldsymbol{\nu}_A\oplus n\boldsymbol{\Gamma}_{b_j},\boldsymbol{\nu}_B}\right\rangle\Big) \\
&= \frac{1}{d}\sum_{n,m=0}^{d-1}\Big(\omega^{n\nu_{b_j}}\omega^{d-mn}\left|\Psi_{\boldsymbol{\mu}_A,\boldsymbol{\mu}_B\oplus m\boldsymbol{e}_{b_j}}\right\rangle\left|\Psi_{\boldsymbol{\nu}_A\oplus n\boldsymbol{\Gamma}_{b_j},\boldsymbol{\nu}_B}\right\rangle\Big) \qquad \text{(D.0.2)}
\end{aligned}
$$

From examining the action of the controlled raising and lowering gates employed in the protocol it is clear that protocol P1 will leave fixed the indices of all vertices from set V_A of the first input state, as well as the indices of all vertices from set V_B of the second input state. This means that if the input state of protocol P1 is $\left|\Psi_{\boldsymbol{\mu}_A,\boldsymbol{\mu}_B}\right\rangle\left|\Psi_{\boldsymbol{\nu}_A,\boldsymbol{\nu}_B}\right\rangle$, then the output state will be of the form $\left|\Psi_{\boldsymbol{\mu}_A,\boldsymbol{\eta}_B}\right\rangle\left|\Psi_{\ \boldsymbol{\eta}_A,\boldsymbol{\nu}_B}\right\rangle$, for some $\boldsymbol{\eta}_B\in\mathbb{F}_d^{\otimes N_B}$ and $\boldsymbol{\eta}_A\in\mathbb{F}_d^{\otimes N_A}$.

With the action of the controlled raising and lowering operators made plain, it is straightforward to determine the effect of the two parts of the protocol. In the first stage, N_A CX_d^+ gates are applied with state copy two as source and copy one as target. These are between the two qudits held by each of the N_A parties with qudits from the set V_A. In the second stage, N_B CX_d^- gates are applied with state copy one as source and copy two as target. These are between the two qudits held by each of the N_B parties with qudits from the set V_B. Before demonstrating the effect of each stage, define the row vectors $\boldsymbol{K}^{(1)},\boldsymbol{K}^{(2)}\in\mathbb{F}_d^{\otimes N_A}$. Furthermore, define a weighted sum of the adjacency matrix partial row vectors: $\boldsymbol{\Gamma}\cdot\boldsymbol{K}^{(1)}:=\boldsymbol{\Gamma}_{a_1}K_{a_1}^{(1)}+\cdots+\boldsymbol{\Gamma}_{a_{N_A}}\boldsymbol{K}_{a_{N_A}}^{(1)}$. Define also a weighted sum of the entries of the multi-index $\boldsymbol{\mu_A}:\boldsymbol{\mu}_A\cdot\boldsymbol{K}^{(1)}:=\mu_{a_1}K_{a_1}^{(1)}+\cdots+\mu_{a_{N_A}}K_{a_{N_A}}^{(1)}$. Note that $\boldsymbol{\Gamma}\cdot\boldsymbol{K}^{(1)}\in\mathbb{F}_d^{\otimes N_B}$ and $\boldsymbol{\mu}_A\cdot\boldsymbol{K}^{(1)}\in\mathbb{F}_d^{\otimes N_A}$

The state which results from applying $\prod_{i=1}^{N_A}CX_d^{+(v_{a_i})}$ with state copy two as source and copy one as target, to the product state $\left|\Psi_{\boldsymbol{\mu}_A,\boldsymbol{\mu}_B}\right\rangle\left|\Psi_{\boldsymbol{\nu}_A,\boldsymbol{\nu}_B}\right\rangle$ is a superposition state with $d^{N_A}\cdot d^{N_A}$ terms. It can be calculated by repetition of Equation D.0.1 for each of the vertices in V_A,

$$\begin{aligned}
\prod_{i=1}^{N_A} CX_d^{+(v_{a_i})} \left|\Psi_{\boldsymbol{\mu}_A,\boldsymbol{\mu}_B}\right\rangle \left|\Psi_{\boldsymbol{\nu}_A,\boldsymbol{\nu}_B}\right\rangle &= \prod_{i=2}^{N_A} CX_d^{+(v_{a_i})} \left[\frac{1}{d} \sum_{K_{a_1}^{(1)},K_{a_1}^{(2)}=0}^{d-1} \omega^{K_{a_1}^{(1)}(d-1)\mu_{a_1}} \omega^{d-K_{a_1}^{(2)}K_{a_1}^{(1)}} \right. \\
&\quad \left. \left|\Psi_{\boldsymbol{\mu_A},\boldsymbol{\mu}_B\oplus K_{a_1}^{(1)}(d-1)\boldsymbol{\Gamma}_{a_1}}\right\rangle \left|\Psi_{\boldsymbol{\nu}_A\oplus K_{a_1}^{(2)}\boldsymbol{e}_{a_1},\boldsymbol{\nu}_B}\right\rangle\right] \\
&= \prod_{i=3}^{N_A} CX_d^{+(v_{a_i})} \left[\frac{1}{d} \sum_{K_{a_1}^{(1)},K_{a_1}^{(2)}=0}^{d-1} \sum_{K_{a_2}^{(1)},K_{a_2}^{(2)}=0}^{d-1} \omega^{(d-1)(\mu_{a_1}K_{a_1}^{(1)}+\mu_{a_2}K_{a_2}^{(1)})} \right. \\
&\quad \omega^{d-(K_{a_1}^{(2)}K_{a_1}^{(1)})+K_{a_2}^{(2)}K_{a_2}^{(1)}} \left|\Psi_{\boldsymbol{\mu_A},\boldsymbol{\mu}_B\oplus(d-1)(K_{a_1}^{(1)}\boldsymbol{\Gamma}_{a_1}\oplus K_{a_2}^{(1)}\boldsymbol{\Gamma}_{a_2})}\right\rangle \\
&\quad \left.\left|\Psi_{\boldsymbol{\nu}_A\oplus(K_{a_1}^{(2)}\boldsymbol{e}_{a_1}\oplus K_{a_2}^{(2)}\boldsymbol{e}_{a_2}),\boldsymbol{\nu}_B}\right\rangle\right] \\
&\vdots \\
&= \frac{1}{d^{N_A}} \sum_{\boldsymbol{K^{(1)}}} \sum_{\boldsymbol{K^{(2)}}} \omega^{(d-1)\boldsymbol{\mu}_A\cdot\boldsymbol{K}^{(1)}} \omega^{d-\boldsymbol{K}^{(1)}\cdot\boldsymbol{K}^{(2)}} \\
&\quad \left|\Psi_{\boldsymbol{\mu}_A,\boldsymbol{\mu}_B\oplus(d-1)\boldsymbol{\Gamma}\cdot\boldsymbol{K}^{(1)}}\right\rangle \left|\Psi_{\boldsymbol{\nu}_A\oplus\boldsymbol{K}^{(2)},\boldsymbol{\nu}_B}\right\rangle \qquad \text{(D.0.3)}
\end{aligned}$$

With the action of the controlled raise operations known, it is possible to determine the form of the resulting state after the subsequent controlled lowering operations. The calculation consists of iteratively applying Equation D.0.2 to the state in Equation D.0.3. The result will be a superposition state with $(d^{N_A})^2 \cdot (d^{N_B})^2$ terms. One observation is that since $\boldsymbol{\mu}_A$ and $\boldsymbol{\nu}_B$ remain fixed in the procedure, the number of unique terms in the superposition is limited to $d^{N_A+N_B}$, suggesting a large amount of repetition of basis states in the resulting superposition. Define now the multi-indices $\boldsymbol{M}^{(1)},\ \boldsymbol{M}^{(2)} \in \mathbb{F}_d^{\otimes N_B}$. Note that $\boldsymbol{\Gamma}\cdot\boldsymbol{M}^{(2)} \in \mathbb{F}_d^{\otimes N_A}$ and $\boldsymbol{\nu}_B\cdot\boldsymbol{M}^{(2)} \in \mathbb{F}_d^{\otimes N_B}$.

$$\begin{aligned}
\mathrm{P1}\big(\left|\Psi_{\boldsymbol{\mu}_A,\boldsymbol{\mu}_B}\right\rangle \left|\Psi_{\boldsymbol{\nu}_A,\boldsymbol{\nu}_B}\right\rangle\big) &= \prod_{j=1}^{N_B} CX_d^{-(v_{b_j})} \prod_{i=1}^{N_A} CX_d^{+(v_{a_i})} \left|\Psi_{\boldsymbol{\mu}_A,\boldsymbol{\mu}_B}\right\rangle \left|\Psi_{\boldsymbol{\nu}_A,\boldsymbol{\nu}_B}\right\rangle \\
&= \frac{1}{d^{N_A+N_B}} \sum_{\boldsymbol{M}^{(1)},\boldsymbol{M}^{(2)}} \sum_{\boldsymbol{K}^{(1)},\boldsymbol{K}^{(2)}} \omega^{(d-\boldsymbol{K}^{(1)}\cdot\boldsymbol{K}^{(2)})+(d-\boldsymbol{M}^{(1)}\cdot\boldsymbol{M}^{(2)})} \\
&\quad \omega^{\boldsymbol{\nu}_B\cdot\boldsymbol{M}^{(2)}+(d-1)\boldsymbol{\mu}_A\cdot\boldsymbol{K}^{(1)}} \left|\Psi_{\boldsymbol{\mu}_A,\boldsymbol{\mu}_B\oplus(d-1)\boldsymbol{\Gamma}\cdot\boldsymbol{K}^{(1)}\oplus\boldsymbol{M}^{(1)}}\right\rangle \\
&\quad \left|\Psi_{\boldsymbol{\nu}_A\oplus\boldsymbol{K}^{(2)}\oplus\boldsymbol{\Gamma}\cdot\boldsymbol{M}^{(2)},\boldsymbol{\nu}_B}\right\rangle. \qquad \text{(D.0.4)}
\end{aligned}$$

The first important thing to notice about the resulting state concerns the updated multi-index of the vertices in V_B of state 1. If we fix a multi-index $\boldsymbol{K}^{(1)}$, then $(d-1)\boldsymbol{\Gamma}\cdot\boldsymbol{K}^{(1)}$ is a fixed vector in $\mathbb{F}_d^{\otimes N_B}$. Hence if we have a sum over all multi-indices $\boldsymbol{M}^{(1)} \in \mathbb{F}_d^{\otimes N_B}$, then we can introduce the multi-index $\boldsymbol{B} \in \mathbb{F}_d^{\otimes N_B}$ and make the replacement,

$$(d-1)\boldsymbol{\Gamma}\cdot\boldsymbol{K}^{(1)} \oplus \boldsymbol{M}^{(1)} \equiv \boldsymbol{B}. \qquad \text{(D.0.5)}$$

Following a similar argument, for fixed $\boldsymbol{M}^{(2)}$ we can introduce the multi-index $\boldsymbol{A} \in \mathbb{F}_d^{\otimes N_A}$ and make the following replacement,

$$\boldsymbol{\Gamma} \cdot \boldsymbol{M}^{(2)} \oplus \boldsymbol{K}^{(2)} \equiv \boldsymbol{A}. \tag{D.0.6}$$

With both replacements made, the resulting state is

$$\begin{aligned}
\mathrm{P1}\big(|\Psi_{\boldsymbol{\mu}_A,\boldsymbol{\mu}_B}\rangle\,|\Psi_{\boldsymbol{\nu}_A,\boldsymbol{\nu}_B}\rangle\big) &= \frac{1}{d^{N_A+N_B}} \sum_{\boldsymbol{A}} \cdot \sum_{\boldsymbol{B}} \cdot \sum_{\boldsymbol{M}^{(2)}} \cdot \sum_{\boldsymbol{K}^{(1)}} \omega^{d-\boldsymbol{M}^{(2)}\cdot(\boldsymbol{\Gamma}\cdot\boldsymbol{K}^{(1)})} \omega^{d-(d-1)(\boldsymbol{K}^1\cdot(\boldsymbol{\Gamma}\cdot\boldsymbol{M}^{(2)}))} \\
&\quad \omega^{\boldsymbol{M}^{(2)}\cdot(\boldsymbol{\nu}_B\ominus\boldsymbol{B})} \omega^{\boldsymbol{K}^{(1)}\cdot((d-1)\boldsymbol{\mu}_A\ominus\boldsymbol{A})}\,|\Psi_{\boldsymbol{\mu}_A,\boldsymbol{\mu}_B\oplus\boldsymbol{B}}\rangle\,|\Psi_{\boldsymbol{\nu}_A\oplus\boldsymbol{A},\boldsymbol{\nu}_B}\rangle \\
&= \frac{1}{d^{N_A+N_B}} \sum_{\boldsymbol{A}} \cdot \sum_{\boldsymbol{B}} \cdot \sum_{\boldsymbol{M}^{(2)}} \cdot \sum_{\boldsymbol{K}^{(1)}} \omega^{\boldsymbol{M}^{(2)}\cdot(\boldsymbol{\nu}_B\ominus\boldsymbol{B})} \omega^{\boldsymbol{K}^{(1)}\cdot((d-1)\boldsymbol{\mu}_A\ominus\boldsymbol{A})} \\
&\quad |\Psi_{\boldsymbol{\mu}_A,\boldsymbol{\mu}_B\oplus\boldsymbol{B}}\rangle\,|\Psi_{\boldsymbol{\nu}_A\oplus\boldsymbol{A},\boldsymbol{\nu}_B}\rangle \\
&= \sum_{\boldsymbol{A}} \cdot \sum_{\boldsymbol{B}} \delta_{\boldsymbol{\nu}_B,\boldsymbol{B}}\ \delta_{(d-1)\boldsymbol{\mu}_A,\boldsymbol{A}}\,|\Psi_{\boldsymbol{\mu}_A,\boldsymbol{\mu}_B\oplus\boldsymbol{B}}\rangle\,|\Psi_{\boldsymbol{\nu}_A\oplus\boldsymbol{A},\boldsymbol{\nu}_B}\rangle\,.
\end{aligned} \tag{D.0.7}$$

In the last line of the equation we note that the sums over $\boldsymbol{M}^{(2)}$ and $\boldsymbol{K}^{(1)}$ are over all the roots of unity, with each root raised to some exponent $\boldsymbol{\nu}_B\ominus\boldsymbol{B}$ and $(d-1)\boldsymbol{\mu}_A\ominus\boldsymbol{A}$, respectively. These sums are zero if the two exponents are non-zero, and equal to d^{N_B} and d^{N_A} respectively if the exponents are both zero. We have introduced a multi-indexed Kronecker-delta $\delta_{\boldsymbol{i},\boldsymbol{j}}$ used to represent the product of Kronecker-delta's, one for each index in the multi-index, $\delta_{\boldsymbol{i},\boldsymbol{j}} := \delta_{i_1,j_1}\delta_{i_2,j_2}\cdots\delta_{i_{N_i},j_{N_j}}$. Finally, we carry out the summation, making use of the Kronecker-deltas,

$$\mathrm{P1}\big(|\Psi_{\boldsymbol{\mu}_A,\boldsymbol{\mu}_B}\rangle\,|\Psi_{\boldsymbol{\nu}_A,\boldsymbol{\nu}_B}\rangle\big) = |\Psi_{\boldsymbol{\mu}_A,\boldsymbol{\mu}_B\oplus\boldsymbol{\nu}_B}\rangle\,\big|\Psi_{\boldsymbol{\nu}_A\oplus(d-1)\boldsymbol{\mu}_A,\boldsymbol{\nu}_B}\big\rangle\,. \tag{D.0.8}$$

□

During the measurement stage, all parties belonging to set V_A measure their qudits from state copy ρ_2 in the eigenbasis of the shift operator, recording in results $\omega^{\alpha_1}\omega^{\alpha_2}\cdots\omega^{\alpha_{N_A}} := \omega^{\boldsymbol{\alpha}_A}$, $\boldsymbol{\alpha}_A \in \mathbb{F}_d^{\otimes N_A}$, and all parties belonging to the set V_B measure their qudits from state copy ρ_2 in the eigenbasis of the phase operator, recording results $\omega^{\boldsymbol{\beta}_B}$, $\boldsymbol{\beta}_B \in \mathbb{F}_d^{\otimes N_B}$.

Claim 2. If the measurement results fulfill the condition

$$(\alpha_j + \sum_{k,j\in E} \Gamma_{jk}\beta_k) \bmod d = 0,\ \forall j \in \mathbb{Z}_{N_A}$$

then $\boldsymbol{\mu}_A \equiv \boldsymbol{\nu}_A$ and the output state will have the updated coefficients

$$\tilde{\lambda}_{\boldsymbol{\gamma}_A,\boldsymbol{\gamma}_B} = \sum_{\{(\boldsymbol{\mu}_B,\boldsymbol{\nu}_B)|\boldsymbol{\mu}_B\oplus\boldsymbol{\nu}_B=\boldsymbol{\gamma}_B\}} \frac{1}{K_1}\lambda_{\boldsymbol{\gamma}_A,\boldsymbol{\mu}_B}\lambda_{\boldsymbol{\gamma}_A,\boldsymbol{\nu}_B},$$

where $K_1 = \sum_{\boldsymbol{\mu}_A}\sum_{\boldsymbol{\mu}_B}\sum_{\boldsymbol{\nu}_B}\lambda_{\boldsymbol{\mu}_A,\boldsymbol{\mu}_B}\lambda_{\boldsymbol{\mu}_A,\boldsymbol{\nu}_B}$.

Proof. To begin, we write the graph state corresponding to a graph G in the eigenbasis of the phase operator Z, which we also reference as the standard basis.

$$|\Psi_{\mathbf{0},\mathbf{0}}\rangle_G = \frac{1}{d^{\frac{N}{2}}} \sum_{\boldsymbol{i_A}} \sum_{\boldsymbol{i_B}} \omega^{\sum_{a=1}^{N_A} \sum_{b=N_A+1}^{N_B+N_A} \Gamma_{ab}(\boldsymbol{e}_a \cdot \boldsymbol{i}_A)(\boldsymbol{e}_b \cdot \boldsymbol{i}_B)} |\boldsymbol{i}_A, \boldsymbol{i}_B\rangle\,, \tag{D.0.9}$$

where the multi-indices labelling the state are $\boldsymbol{i}_A \in \mathbb{F}_d^{N_A}$, $\boldsymbol{i}_B \in \mathbb{F}_d^{N_B}$. Recall the Weyl operators 2.3 from Section 2.1.3. By applying the Weyl operator $W_{(0,\boldsymbol{\mu})}$, with $\boldsymbol{\mu} = (\boldsymbol{\mu}_A, \boldsymbol{\mu}_B)$, the action of which follows from Equation 4.3.4, we can then write an arbitrary graph basis state in the standard basis as,

$$|\Psi_{\boldsymbol{\mu}_A,\boldsymbol{\mu}_B}\rangle_G = \frac{1}{d^{\frac{N}{2}}} \sum_{\boldsymbol{i_A}\boldsymbol{i_B}} \omega^{\boldsymbol{\mu}_A \cdot \boldsymbol{i}_A} \omega^{\boldsymbol{\mu}_B \cdot \boldsymbol{i}_B} \omega^{\sum_{a=1}^{N_A} \sum_{b=N_A+1}^{N_B+N_A} \Gamma_{ab}(\boldsymbol{e}_a \cdot \boldsymbol{i}_A)(\boldsymbol{e}_b \cdot \boldsymbol{i}_B)} |\boldsymbol{i}_A, \boldsymbol{i}_B\rangle\,. \tag{D.0.10}$$

Recall that we consider as input two identical copies of a mixed state that is diagonal in the graph state basis,

$$\begin{aligned}\rho_{12} &= \rho_1 \otimes \rho_2 \\ &= \sum_{\boldsymbol{\mu}_A,\boldsymbol{\mu}_B} \lambda_{\boldsymbol{\mu}_A,\boldsymbol{\mu}_B} |\Psi_{\boldsymbol{\mu}_A,\boldsymbol{\mu}_B}\rangle \langle\Psi_{\boldsymbol{\mu}_A,\boldsymbol{\mu}_B}|_G \otimes \sum_{\boldsymbol{\nu}_A,\boldsymbol{\nu}_B} \lambda_{\boldsymbol{\nu}_A,\boldsymbol{\nu}_B} |\Psi_{\boldsymbol{\nu}_A,\boldsymbol{\nu}_B}\rangle \langle\Psi_{\boldsymbol{\nu}_A,\boldsymbol{\nu}_B}|_G.\end{aligned} \tag{D.0.11}$$

Allow $CG(\cdot)$ to represent the transformations implemented by the sequence of multilateral gates applied in P1. It then follows from claim 1 that the state is updated to,

$$\begin{aligned}CG(\rho_{12}) = \sum_{\boldsymbol{\mu}_A,\boldsymbol{\mu}_B} \sum_{\boldsymbol{\nu}_A,\boldsymbol{\nu}_B} \lambda_{\boldsymbol{\mu}_A,\boldsymbol{\mu}_B} \lambda_{\boldsymbol{\nu}_A,\boldsymbol{\nu}_B} |\Psi_{\boldsymbol{\mu}_A,\boldsymbol{\mu}_B \oplus \boldsymbol{\nu}_B}\rangle \langle\Psi_{\boldsymbol{\mu}_A,\boldsymbol{\mu}_B \oplus \boldsymbol{\nu}_B}|_G \\ \otimes \left|\Psi_{\boldsymbol{\nu}_A \oplus (d-1)\boldsymbol{\mu}_A,\boldsymbol{\nu}_B}\right\rangle \left\langle\Psi_{\boldsymbol{\nu}_A \oplus (d-1)\boldsymbol{\mu}_A,\boldsymbol{\nu}_B}\right|_G.\end{aligned} \tag{D.0.12}$$

Since the protocol mandates measuring each qudit of the second copy of the state, we write the second part of the state in the eigenbasis of the Z operator,

$$\begin{aligned}CG(\rho_{12}) = \sum_{\boldsymbol{\mu}_A,\boldsymbol{\mu}_B} \sum_{\boldsymbol{\nu}_A,\boldsymbol{\nu}_B} \lambda_{\boldsymbol{\mu}_A,\boldsymbol{\mu}_B} \lambda_{\boldsymbol{\nu}_A,\boldsymbol{\nu}_B} |\Psi_{\boldsymbol{\mu}_A,\boldsymbol{\mu}_B \oplus \boldsymbol{\nu}_B}\rangle \langle\Psi_{\boldsymbol{\mu}_A,\boldsymbol{\mu}_B \oplus \boldsymbol{\nu}_B}|_G \\ \otimes \Big\{ \frac{1}{d^N} \sum_{\boldsymbol{i}_A,\boldsymbol{k}_A} \sum_{\boldsymbol{i}_B,\boldsymbol{k}_B} \omega^{(\boldsymbol{\nu}_A \oplus (d-1)\boldsymbol{\mu}_A) \cdot (\boldsymbol{i}_A - \boldsymbol{k}_A)} \omega^{\boldsymbol{\nu}_B \cdot (\boldsymbol{i}_B - \boldsymbol{k}_B)} \\ \omega^{\sum_{a=1}^{N_A} \sum_{b=N_A+1}^{N_B+N_A} \Gamma_{ab}[(\boldsymbol{e}_a \cdot \boldsymbol{i}_A)(\boldsymbol{e}_b \cdot \boldsymbol{i}_B) - (\boldsymbol{k}_A \cdot \boldsymbol{e}_a)(\boldsymbol{k}_B \cdot \boldsymbol{e}_b)]} \Big\} |\boldsymbol{i}_A, \boldsymbol{i}_B\rangle \langle\boldsymbol{k}_A, \boldsymbol{k}_B|\,.\end{aligned} \tag{D.0.13}$$

The first step of the measurement stage in protocol P1 is for each of the parties belonging to set V_B to measure their qudit belonging to the second state in the Z eigenbasis. Denote the measurements[1] as $M_B(\cdot)$ and their measurement results

[1] For a resource explaining the formalism of measurements in quantum mechanics see [6]. Here we only require projective measurements.

$\omega^{\boldsymbol{j}_B} := \omega^{j_1}\omega^{j_2}\cdots\omega^{j_{N_B}}$, where $j_i \in \mathbb{F}_d$. Let π_{j_l} be the projector [6] onto the j_l-th eigenstate of the Z operator. The post-measurement state is as follows,

$$
\begin{aligned}
M_B(CG(\rho_{12})) &= \frac{(\pi_{j1}\otimes\pi_{j2}\cdots\pi_{j_{N_B}})CG(\rho_{12})(\pi_{j1}\otimes\pi_{j2}\cdots\pi_{j_{N_B}})^\dagger}{Tr\big((\pi_{j1}\otimes\pi_{j2}\cdots\pi_{j_{N_B}})CG(\rho_{12})\big)} \\
&= \frac{1}{Tr\big((\pi_{j1}\otimes\pi_{j2}\cdots\pi_{j_{N_B}})CG(\rho_{12})\big)}\Bigg[\frac{1}{d^N}\sum_{\boldsymbol{\mu}_A,\boldsymbol{\mu}_B}\sum_{\boldsymbol{\nu}_A,\boldsymbol{\nu}_B}\lambda_{\boldsymbol{\mu}_A,\boldsymbol{\mu}_B}\lambda_{\boldsymbol{\nu}_A,\boldsymbol{\nu}_B}\left|\Psi_{\boldsymbol{\mu}_A,\boldsymbol{\mu}_B\oplus\boldsymbol{\nu}_B}\right\rangle\left\langle\Psi_{\boldsymbol{\mu}_A,\boldsymbol{\mu}_B\oplus\boldsymbol{\nu}_B}\right|_G \\
&\quad\otimes\Big(\sum_{\boldsymbol{i}_A,\boldsymbol{k}_A}\omega^{(\boldsymbol{\nu}_A\oplus(d-1)\boldsymbol{\mu}_A)\cdot(\boldsymbol{i}_A-\boldsymbol{k}_A)}\Big)\Big(\sum_{\boldsymbol{i}_B,\boldsymbol{k}_B}\boldsymbol{\delta}_{\boldsymbol{i}_B,\boldsymbol{j}_B}\boldsymbol{\delta}_{\boldsymbol{k}_B,\boldsymbol{j}_B}\,\omega^{\boldsymbol{\nu}_B\cdot(\boldsymbol{i}_B-\boldsymbol{k}_B)} \\
&\quad\omega^{\sum_{a=1}^{N_A}\sum_{b=N_A+1}^{N_B+N_A}\Gamma_{ab}[(\boldsymbol{e}_a\cdot\boldsymbol{i}_A)(\boldsymbol{e}_b\cdot\boldsymbol{i}_B)-(\boldsymbol{k}_A\cdot\boldsymbol{e}_a)(\boldsymbol{k}_B\cdot\boldsymbol{e}_b)]}\Big)\left|\boldsymbol{i}_A,\boldsymbol{j}_B\right\rangle\left\langle\boldsymbol{k}_A,\boldsymbol{j}_B\right|\Bigg] \\
&= \sum_{\boldsymbol{\mu}_A,\boldsymbol{\mu}_B}\sum_{\boldsymbol{\nu}_A,\boldsymbol{\nu}_B}\lambda_{\boldsymbol{\mu}_A,\boldsymbol{\mu}_B}\lambda_{\boldsymbol{\nu}_A,\boldsymbol{\nu}_B}\left|\Psi_{\boldsymbol{\mu}_A,\boldsymbol{\mu}_B\oplus\boldsymbol{\nu}_B}\right\rangle\left\langle\Psi_{\boldsymbol{\mu}_A,\boldsymbol{\mu}_B\oplus\boldsymbol{\nu}_B}\right|_G\otimes \\
&\quad\Big(\frac{1}{d^{N_A}}\sum_{\boldsymbol{i}_A,\boldsymbol{k}_A}\omega^{(\boldsymbol{\nu}_A\oplus(d-1)\boldsymbol{\mu}_A)\cdot(\boldsymbol{i}_A-\boldsymbol{k}_A)}\omega^{\sum_{a=1}^{N_A}\sum_{b=N_A+1}^{N_B+N_A}\Gamma_{ab}(\boldsymbol{e}_a\cdot(\boldsymbol{i}_A-\boldsymbol{k}_A))(\boldsymbol{e}_b\cdot\boldsymbol{j}_B)}\Big) \\
&\quad\left|\boldsymbol{i}_A,\boldsymbol{j}_B\right\rangle\left\langle\boldsymbol{k}_A,\boldsymbol{j}_B\right|, \qquad \text{(D.0.14)}
\end{aligned}
$$

where in the last line we compute the normalization factor $Tr\big((\pi_{j1}\otimes\pi_{j2}\cdots\pi_{j_{N_B}})CG(\rho_{12})\big) = \frac{1}{d^{N_B}}$. In order to measure the qudits of state two belonging to set V_A in the X eigenbasis, we first make a basis transformation by applying a Hadamard operator to each qudit in the set. The resulting state is:

$$
\begin{aligned}
M_B(CG(\rho_{12}))^x &= H^{\otimes N_A}M_B(CG(\rho_{12}))(H^\dagger)^{\otimes N_A} \\
&= \sum_{\boldsymbol{\mu}_A,\boldsymbol{\mu}_B}\sum_{\boldsymbol{\nu}_A,\boldsymbol{\nu}_B}\lambda_{\boldsymbol{\mu}_A,\boldsymbol{\mu}_B}\lambda_{\boldsymbol{\nu}_A,\boldsymbol{\nu}_B}\left|\Psi_{\boldsymbol{\mu}_A,\boldsymbol{\mu}_B\oplus\boldsymbol{\nu}_B}\right\rangle\left\langle\Psi_{\boldsymbol{\mu}_A,\boldsymbol{\mu}_B\oplus\boldsymbol{\nu}_B}\right|_G\otimes \\
&\quad\Big(\frac{1}{d^{2N_A}}\sum_{\boldsymbol{i}_A,\boldsymbol{k}_A}\omega^{(\boldsymbol{\nu}_A\oplus(d-1)\boldsymbol{\mu}_A)\cdot(\boldsymbol{i}_A-\boldsymbol{k}_A)}\omega^{\sum_{a=1}^{N_A}\sum_{b=N_A+1}^{N_B+N_A}\Gamma_{ab}(\boldsymbol{e}_a\cdot(\boldsymbol{i}_A-\boldsymbol{k}_A))(\boldsymbol{e}_b\cdot\boldsymbol{j}_B)}\Big) \\
&\quad\sum_{\boldsymbol{x},\boldsymbol{z}}\omega^{\boldsymbol{x}\cdot\boldsymbol{i}_A-\boldsymbol{k}_A\cdot\boldsymbol{z}}\left|\boldsymbol{x},\boldsymbol{j}_B\right\rangle\left\langle\boldsymbol{z},\boldsymbol{j}_B\right|, \qquad \text{(D.0.15)}
\end{aligned}
$$

where, the multi-indices $\boldsymbol{x},\ \boldsymbol{z} \in \mathbb{F}_{\mathbb{d}}^{\mathbb{N}_{\mathbb{A}}}$. With the basis transformation implemented, we measure each qudit of state two belonging to the set V_A. As before, denote the measurements by $M_A(\cdot)$ and the measurement results of the N_A parties by $\omega^{\boldsymbol{j}'_A} := \omega^{j'_1}\omega^{j'_2}\cdots\omega^{j'_{N_A}}$, where each $j'_i \in \mathbb{F}_d$. The post-measurement state is as

follows,

$$
\begin{aligned}
M_A(M_B(CG(\rho_{12})))^x = & \frac{(\pi_{j'_1}\otimes\pi_{j'_2}\cdots\pi_{j'_{N_A}})(MB(CG(\rho_{12})))^x(\pi_{j'_1}\otimes\pi_{j'_2}\cdots\pi_{j'_{N_A}})^\dagger}{Tr\big((\pi_{j'_1}\otimes\pi_{j'_2}\otimes\cdots\otimes\pi_{j'_{N_A}})(MB(CG(\rho_{12})))^x\big)} \\
= & \sum_{\boldsymbol{\mu}_A,\boldsymbol{\mu}_B}\sum_{\boldsymbol{\nu}_A,\boldsymbol{\nu}_B}\lambda_{\boldsymbol{\mu}_A,\boldsymbol{\mu}_B}\lambda_{\boldsymbol{\nu}_A,\boldsymbol{\nu}_B}\left|\Psi_{\boldsymbol{\mu}_A,\boldsymbol{\mu}_B\oplus\boldsymbol{\nu}_B}\right\rangle\left\langle\Psi_{\boldsymbol{\mu}_A,\boldsymbol{\mu}_B\oplus\boldsymbol{\nu}_B}\right|_G\otimes \\
& \Big(\frac{1}{d^{2N_A}}\sum_{\boldsymbol{i}_A,\boldsymbol{k}_A}\omega^{[\boldsymbol{\nu}_A\oplus(d-1)\boldsymbol{\mu}_A\oplus\boldsymbol{j}_A\oplus(\sum_{a=1}^{N_A}\sum_{b=N_A+1}^{N_B+N_A}\Gamma_{ab}(\boldsymbol{e}_b\cdot\boldsymbol{j}_B))\boldsymbol{e}_a]\cdot(\boldsymbol{i}_A-\boldsymbol{k}_A)}\Big)\left|\boldsymbol{j}_A,\boldsymbol{j}_B\right\rangle\left\langle\boldsymbol{j}_A,\boldsymbol{j}_B\right| \\
= & \sum_{\boldsymbol{\mu}_A,\boldsymbol{\mu}_B}\sum_{\boldsymbol{\nu}_A,\boldsymbol{\nu}_B}\lambda_{\boldsymbol{\mu}_A,\boldsymbol{\mu}_B}\lambda_{\boldsymbol{\nu}_A,\boldsymbol{\nu}_B}\left|\Psi_{\boldsymbol{\mu}_A,\boldsymbol{\mu}_B\oplus\boldsymbol{\nu}_B}\right\rangle\left\langle\Psi_{\boldsymbol{\mu}_A,\boldsymbol{\mu}_B\oplus\boldsymbol{\nu}_B}\right|_G\otimes \\
& \delta_{[\boldsymbol{\nu}_A\oplus(d-1)\boldsymbol{\mu}_A\oplus\boldsymbol{j}_A+(\sum_{a=1}^{N_A}\sum_{b=N_A+1}^{N_B+N_A}\Gamma_{ab}(\boldsymbol{e}_b\cdot\boldsymbol{j}_B))\boldsymbol{e}_a],\boldsymbol{0}}\left|\boldsymbol{j}_A,\boldsymbol{j}_B\right\rangle\left\langle\boldsymbol{j}_A,\boldsymbol{j}_B\right|. \quad \text{(D.0.16)}
\end{aligned}
$$

In the third line we obtain the multi-indexed Dirac delta because the sum over the d-th primitive roots of unity vanishes unless the exponent of each is zero. The multi-indexed Dirac delta in the post-measurement state gives rise to the post-selection condition, which is to require that: $\boldsymbol{j}_A \oplus (\sum_{a=1}^{N_A}\sum_{b=N_A+1}^{N_B+N_A}\boldsymbol{\Gamma}_{ab}(\boldsymbol{e}_b\cdot\boldsymbol{j}_B)\boldsymbol{e}_a)) = 0 \bmod d$, because this implies that $\boldsymbol{\nu}_A \oplus (d-1)\boldsymbol{\mu}_A = 0 \bmod d$, and hence $\boldsymbol{\mu}_A = \boldsymbol{\nu}_A \bmod d$. The post selection condition can be re-written explicitly as a system of Equations, in which case we have that for each node of set V_A, a_i, $i \in \{0,\cdots N_A\}$ the measurement results must satisfy the following Equations with the results from nodes of set V_B, b_l, $l \in \{0,\cdots,N_B\}$:

$$
\Big(j_{a_i} + \sum_{(i,l)\in E}\boldsymbol{\Gamma}_{il}j_{b_l}\Big) \bmod d = 0. \quad \text{(D.0.17)}
$$

Furthermore, by applying the post-selection condition and tracing out the qudits from the second state copy, we arrive at the updated state which is output by sub-routine P1,

$$
\tilde{\rho} = \frac{\sum_{\boldsymbol{\mu}_A,\boldsymbol{\mu}_B}\sum_{\boldsymbol{\nu}_B}\lambda_{\boldsymbol{\mu}_A,\boldsymbol{\mu}_B}\lambda_{\boldsymbol{\mu}_A,\boldsymbol{\nu}_B}\left|\Psi_{\boldsymbol{\mu}_A,\boldsymbol{\mu}_B\oplus\boldsymbol{\nu}_B}\right\rangle\left\langle\Psi_{\boldsymbol{\mu}_A,\boldsymbol{\mu}_B\oplus\boldsymbol{\nu}_B}\right|_G}{\sum_{\boldsymbol{\mu}_A,\boldsymbol{\mu}_B}\sum_{\boldsymbol{\nu}_B}\lambda_{\boldsymbol{\mu}_A,\boldsymbol{\mu}_B}\lambda_{\boldsymbol{\mu}_A,\boldsymbol{\nu}_B}}, \quad \text{(D.0.18)}
$$

which has the updated coefficients

$$
\tilde{\lambda}_{\boldsymbol{\gamma}_A,\boldsymbol{\gamma}_B} = \sum_{\{(\boldsymbol{\mu}_B,\boldsymbol{\nu}_B)|\boldsymbol{\mu}_B\oplus\boldsymbol{\nu}_B=\boldsymbol{\gamma}_B\}}\frac{1}{K_1}\lambda_{\boldsymbol{\gamma}_A,\boldsymbol{\mu}_B}\lambda_{\boldsymbol{\gamma}_A,\boldsymbol{\nu}_B}, \quad \text{(D.0.19)}
$$

where $K_1 = \sum_{\boldsymbol{\mu}_A}\sum_{\boldsymbol{\mu}_B}\sum_{\boldsymbol{\nu}_B}\lambda_{\boldsymbol{\mu}_A,\boldsymbol{\mu}_B}\lambda_{\boldsymbol{\mu}_A,\boldsymbol{\nu}_B}$.

□

The proof of subroutine P2 is exactly analogous, and hence will not be demonstrated here.

E

Proofs for Section 7.1

Proposition 7.1. Application of purification subroutine P1 (P2)[1] with faulty two-qudit operations modeled by Equations 7.1.1 and 7.1.2 is equivalent to first applying all noise processes, followed by application of the errorless purification subroutine.

Proof.
We will show here only the proof for subroutine P1, as the proof for P2 is analagous.

The sequence of faulty gates in subroutine P1 is represented by,

$$\mathcal{E}_{\tilde{U}_{b_{N_B,1},b_{N_B,2}}} \circ \cdots \circ \mathcal{E}_{\tilde{U}_{b_{1,1},b_{1,2}}} \circ \mathcal{E}_{U_{a_{N_A,2},a_{N_A,1}}} \circ \cdots \circ \mathcal{E}_{U_{a_{2,2},a_{2,1}}} \circ \mathcal{E}_{U_{a_{1,2},a_{1,1}}}(\cdot) \quad \text{(E.0.1)}$$

where U and $\tilde{U}$ represent CX_d^+ and CX_d^-, respectively, and $a_{i,j}$ ($b_{i,j}$) represents the i-th qudit of set V_A (V_B), belonging to state copy j. We must demonstrate that this faulty sequence is equivalent to the sequence where all noise processes act first, followed by the perfect two-qudit operations,

$$\tilde{U}_{b_{N_B,1},b_{N_B,2}} \otimes \cdots \otimes U_{a_{1,2},a_{1,1}} \Big[(\mathcal{M}_{b_{N_B,1}} \circ \mathcal{M}_{b_{N_B},2}) \circ \cdots \circ (\mathcal{M}_{a_{1,2}} \circ \mathcal{M}_{a_{1,1}})(\cdot) \Big] (\tilde{U}_{b_{N_B,1},b_{N_B,2}} \otimes \cdots \otimes U_{a_{1,2},a_{1,1}})^\dagger. \quad \text{(E.0.2)}$$

Notice that because of the definition of $\mathcal{M}_j$ in Equation 7.1.2, we could have omitted the $\mathcal{M}_{a_{i,j}}$ from the previous equation. The question of the equivalence of Equations E.0.1 and E.0.2 reduces to checking the equivalence of,

$$\big(CX_d^-\big)_i \Big[\mathcal{M}_{b_{j,1}} \circ \mathcal{M}_{b_{j,2}}(\rho_{12}) \Big] (CX_d^-)_i^\dagger, \quad \text{(E.0.3)}$$

and,

$$\mathcal{M}_{b_{j,1}} \circ \mathcal{M}_{b_{j,2}} \Big(\big(CX_d^-\big)_i (\rho_{12}) \big(CX_d^-\big)_i^\dagger \Big), \quad \text{(E.0.4)}$$

where $(CX_d^-)_i$ acts on the i-th qudits of set V_B, with the one from state copy one as control, and the one from state copy two as target. For the verification, we write

[1] For use of P2 we must consider binarylike input states with noise confined to subset V_B and the the restricted error model must be modified by swapping the role of subsets V_A and V_B in equation 7.1.2

explicitly the error processes $\mathcal{M}_{b_{j,1}} \circ \mathcal{M}_{b_{j,2}}(\rho_{12})$ and demonstrate the commutation with the two-qudit operators term-wise. We have,

$$
\begin{aligned}
(CX_d^-)_i\big[\mathcal{M}_{b_{j,1}} \circ \mathcal{M}_{b_{j,2}}(\rho_{12})\big](CX_d^-)_i^\dagger &= (1-q)^2 (CX_d^-)_i \rho_{12} (CX_d^-)_i^\dagger && \text{(E.0.5)}\\
&+ \frac{q(1-q)}{d}(CX_d^-)_i\big[\big(\mathbb{1}^{\otimes N} \otimes \sum_{l=0}^{d-1} X^{l\boldsymbol{e}_j}\big) \\
&\quad (\rho_{12})\big(\mathbb{1}^{\otimes N} \otimes \sum_{l=0}^{d-1} X^{l\boldsymbol{e}_j}\big)^\dagger\big](CX_d^-)_i^\dagger && \text{(E.0.6)}\\
&+ \frac{q(1-q)}{d}(CX_d^-)_i\big[\big(\sum_{l=0}^{d-1} X^{l\boldsymbol{e}_j} \otimes \mathbb{1}^{\otimes N}\big) \\
&\quad (\rho_{12})\big(\sum_{l=0}^{d-1} X^{l\boldsymbol{e}_j} \otimes \mathbb{1}^{\otimes N}\big)^\dagger\big](CX_d^-)_i^\dagger && \text{(E.0.7)}\\
&+ \frac{q^2}{d^2}(CX_d^-)_i\big[\big(\sum_{l=0}^{d-1} X^{l\boldsymbol{e}_j} \otimes \sum_{m=0}^{d-1} X^{m\boldsymbol{e}_j}\big) \\
&\quad (\rho_{12})\big(\sum_{l=0}^{d-1} X^{l\boldsymbol{e}_j} \otimes \sum_{m=0}^{d-1} X^{m\boldsymbol{e}_j}\big)^\dagger\big](CX_d^-)_i^\dagger && \text{(E.0.8)}
\end{aligned}
$$

For the first term (E.0.5), the commutation is automatic, since $\mathbb{1}^{\otimes N} \otimes \mathbb{1}^{\otimes N}$ always commutes with any operator. To verify the commutation for the remaining terms, recall the decomposition of CX_d^-, as given by Equation 2.1.18. For term E.0.6 we then consider,

$$
\begin{aligned}
(CX_d^-)_i\big(\mathbb{1}^{\otimes N} \otimes \sum_{l=0}^{d-1} X^{l\boldsymbol{e}_j}\big) &= \frac{1}{d}\sum_{s=0}^{d-1}\sum_{t=0}^{d-1} \omega^{d-(st)} Z^{s\boldsymbol{e}_i} \otimes X^{t(d-1)\boldsymbol{e}_i}\big(\mathbb{1}^{\otimes N} \otimes \sum_{l=0}^{d-1} X^{l\boldsymbol{e}_j}\big)\\
&= \big(\mathbb{1}^{\otimes N} \otimes \sum_{l=0}^{d-1} X^{l\boldsymbol{e}_j}\big)\ \frac{1}{d}\sum_{s=0}^{d-1}\sum_{t=0}^{d-1} \omega^{d-(st)} Z^{s\boldsymbol{e}_i} \otimes X^{t(d-1)\boldsymbol{e}_i}\\
&= \big(\mathbb{1}^{\otimes N} \otimes \sum_{l=0}^{d-1} X^{l\boldsymbol{e}_j}\big)(CX_d^-)_i. && \text{(E.0.9)}
\end{aligned}
$$

The commutation in the second line follows because $[\mathbb{1}, Z] = 0$ and $[X^{k_1\boldsymbol{e}_i}, X^{k_2\boldsymbol{e}_i}] = 0\ \forall\ k_1, k_2$. Without writing the calculation explicitly for the other two terms, we explain why it is possible. For term three (E.0.7), the relevant identities are $[\mathbb{1}, X] = 0$, and Equation 2.1.4, which dictates that $Z^{k_1\boldsymbol{e}_i} X^{k_2\boldsymbol{e}_j} = \omega^{k_1 k_2 \boldsymbol{e}_i\cdot\boldsymbol{e}_j} X^{k_2\boldsymbol{e}_j} Z^{k_1\boldsymbol{e}_i}\ \forall\ k_1, k_2$. Hence in term 3 the commutation introduces a phase factor, which cancels out due to the commutation of the Hermitian conjugates. Finally term 4 (E.0.8) does not contain any components not already covered by terms 2 and 3, and hence the error process commutes with the controlled lowering operation.

We have shown the equivalence of Equations E.0.3 and E.0.2, thus confirming the equivalence of Equations E.0.1 and E.0.2. To finish the proof we point out that when all error processes occur before the two-qudit controlled operations, then it is as if the error free protocol is applied to input states that have passed through an additional noisy quantum channel.

□

Proposition 7.2. The state resulting from the error process $\mathcal{M}_{b_j}(\cdot),\ j \in \{1,\ \cdots,\ N_B\}$, given by Equation 7.1.2, on an input state given by Equation 7.1.3, remains of the same form but with the new parameter $x(1-q)$. That is,

$$\mathcal{M}_{b_j}\left(\rho_A(x)\right) = \rho_A(x(1-q)). \tag{7.1.4}$$

Proof.
The calculation called for by Equation 7.1.4 is rather straightforward and makes use of the identity in Equation 4.3.8. For the GHZ type state, which corresponds to the star graph (see Figure C.0.2) every vertex in subset V_B shares a single egde with the lone vertex in subset V_A. By Equation 4.3.8,

$$X^{k\boldsymbol{e}_j}\left|\Psi_{l,\mathbf{0}}\right\rangle = \left|\Psi_{l+k(d-1),\mathbf{0}}\right\rangle. \tag{E.0.10}$$

Equation E.0.10 is used to calculate the action of $\mathcal{M}_{b_j}$ on $\rho_A(x)$,

$$\begin{aligned}
\mathcal{M}_{b_j}\left(\rho_A(x)\right) &= x(1-q)\left|\Psi_{0,\mathbf{0}}\right\rangle\left\langle\Psi_{0,\mathbf{0}}\right| + x\frac{q}{d}\sum_{k=0}^{d-1} X^{k\boldsymbol{e}_j}\left|\Psi_{0,\mathbf{0}}\right\rangle\left\langle\Psi_{0,\mathbf{0}}\right|\left(X^{k\boldsymbol{e}_j}\right)^\dagger \\
&\quad + \frac{1-x}{d}(1-q)\mathbb{1}_{V_A} + \frac{1-x}{d}\frac{q}{d}\sum_{k=0}^{d-1}\sum_{l=0}^{d-1} X^{k\boldsymbol{e}_j}\left|\Psi_{l,\mathbf{0}}\right\rangle\left\langle\Psi_{l,\mathbf{0}}\right|\left(X^{k\boldsymbol{e}_j}\right)^\dagger \\
&= x(1-q)\left|\Psi_{0,\mathbf{0}}\right\rangle\left\langle\Psi_{0,\mathbf{0}}\right| + x\frac{q}{d}\mathbb{1}_{V_A} + \frac{1-x}{d}(1-q)\mathbb{1}_{V_A} + \frac{1-x}{d}\frac{q}{d}d\mathbb{1}_{V_A} \\
&= x(1-q)\left|\Psi_{0,\mathbf{0}}\right\rangle\left\langle\Psi_{0,\mathbf{0}}\right| + \frac{1-x(1-q)}{d}\mathbb{1}_{V_A} \\
&= \rho_A(x(1-q)).
\end{aligned} \tag{E.0.11}$$

□

Here we proceed by deriving equations 7.1.7 and 7.1.8.

Derivation.
To obtain an equation for $x_{\max}$ we look for a fixed point of the fidelity as a result of purification. That is, we search for x such that $\widetilde{F}(x,q) = F(x)$, for a given error level, q. The fidelity of the input states is $F(x) = x + \frac{1-x}{d}$. The fidelity of the state following purification subroutine $P1$ is stated in Equation 7.1.6. Define $\beta := x(1-q)^{N-1}$ and note that immediately we use the identity $\frac{1-F'}{(d-1)} = \frac{1-\beta}{d}$, where $F' = \beta + \frac{1-\beta}{d}$.

$$\begin{aligned}
\frac{\frac{\beta}{(1-q)^{N-1}}(d-1)+1}{d} &= \frac{((d-1)\beta+1)^2\frac{1}{d^2}}{((d-1)\beta+1)^2\frac{1}{d^2} + (d-1)(1-\beta)^2\frac{1}{d^2}} \\
\frac{(d-1)\frac{\beta}{(1-q)^{N-1}}+1}{d} &= \frac{[(d-1)\beta]^2 + 1 + 2(d-1)\beta}{[(d-1)\beta]^2 + 1 + \cancel{2(d-1)\beta} + (d-1) + (d-1)\beta^2 - \cancel{2\beta(d-1)}} \\
(d-1)\frac{\beta}{(1-q)^{N-1}} + 1 &= \frac{[(d-1)\beta]^2 + 1 + 2(d-1)\beta}{1 + (d-1)\beta^2}.
\end{aligned}$$

Rearranging leads to,

$$\begin{aligned}
0 &= [(d-1)\beta]^2 + 1 + 2(d-1)\beta - (1+(d-1)\beta^2)\big((d-1)\frac{\beta}{(1-q)^{N-1}} + 1\big) \\
0 &= [(d-1)\beta]^2 + \cancel{1} + 2(d-1)\beta - \cancel{1} - (d-1)\frac{\beta}{(1-q)^{N-1}} - (d-1)^2\frac{\beta^3}{(1-q)^{N-1}} - (d-1)\beta^2 \\
0 &= \beta(d-1)\Big((d-2)\beta + 2 - \frac{1}{(1-q)^{N-1}} - \frac{(d-1)}{(1-q)^{N-1}}\beta^2\Big) \qquad \text{(E.0.12)}
\end{aligned}$$

For $\beta > 0$ Equation E.0.12 is,

$$\begin{aligned}
\frac{(d-1)}{(1-q)^{N-1}}\beta^2 - (d-2)\beta - 2 + \frac{1}{(1-q)^{N-1}} &= 0 \\
x^2(1-q)^{2(N-1)} - x\frac{d-2}{d-1}(1-q)^{2(N-1)} - \frac{2(1-q)^{N-1}-1}{d-1} &= 0 \qquad \text{(E.0.13)}
\end{aligned}$$

Using the quadratic formula one obtains,

$$x_{\max} = \frac{\frac{d-2}{d-1}(1-q)^{2(N-1)} + \sqrt{\big(\frac{d-2}{d-1}\big)^2(1-q)^{4(N-1)} + 4(1-q)^{2(N-1)}\Big(\frac{2(1-q)^{N-1}-1}{d-1}\Big)}}{2(1-q)^{2(N-1)}}. \qquad \text{(E.0.14)}$$

To derive the gate error threshold from Equation 7.1.7 we solve for q by setting the radical equal to zero. The point at which the radical disappears defines the boundary of the purification regime because beyond that point there can be no real $x_{\max}$, and therefore no maximal reachable fidelity. Define $\alpha := (1-q)^{N-1}$.

$$\begin{aligned}
\big(\frac{d-2}{d-1}\big)^2\alpha^4 + 4\alpha^2\Big(\frac{2\alpha-1}{d-1}\Big) &= 0 \\
\frac{(d-2)^2}{d-1}\alpha^2 + 8\alpha - 4 &= 0. \qquad \text{(E.0.15)}
\end{aligned}$$

Using the quadratic formula and simplifying,

$$\alpha = 2\frac{(d-1)}{(d-2)^2}\Big(\sqrt{4 + \big(\frac{(d-2)^2}{d-1}\big)} - 2\Big). \qquad \text{(E.0.16)}$$

Finally, isolating for q,

$$q_{\text{crit}} = 1 - \left[2\frac{(d-1)}{(d-2)^2}\Big(\sqrt{4 + \frac{(d-2)^2}{d-1}} - 2\Big)\right]^{\frac{1}{N-1}}. \qquad \text{(E.0.17)}$$

□

Proposition 7.3. A single error process $\mathcal{M}_j$, given by Equation 7.1.2, preserves the identity on subset V_A, $\mathcal{M}_j(\mathbb{1}_{V_A}) = \mathbb{1}_{V_A}$, and acts on binary-like closed linear cluster graph basis states as,

$$\mathcal{M}_j\Big(\left|\Psi_{\boldsymbol{\mu}_A,\mathbf{0}}\right\rangle\left\langle\Psi_{\boldsymbol{\mu}_A,\mathbf{0}}\right|\Big) = (1-p)\left|\Psi_{\boldsymbol{\mu}_A,\mathbf{0}}\right\rangle\left\langle\Psi_{\boldsymbol{\mu}_A,\mathbf{0}}\right| + \frac{p}{d-1}\sum_{k=1}^{d-1}\left|\Psi_{\boldsymbol{\mu}_A\oplus k[\boldsymbol{e}_{j-1}\oplus\boldsymbol{e}_{j+1}],\mathbf{0}}\right\rangle\left\langle\Psi_{\boldsymbol{\mu}_A\oplus k[\boldsymbol{e}_{j-1}\oplus\boldsymbol{e}_{j+1}],\mathbf{0}}\right|, \quad (7.1.10)$$

where $(1-p) = \frac{1}{d}\big((d-1)(1-q)+1\big)$.

Proof.
To establish the action of the error process $\mathcal{M}_j$ as in Equation 7.1.2 on binary-like graph basis states, we look to the relation in Equation 4.3.8, which describes the action of powers of shift operators on graph basis states. Here,

$$X_j^k\left|\Psi_{\boldsymbol{\mu}_A,\mathbf{0}}\right\rangle = \omega^{k(d-1)\boldsymbol{\mu}_A\cdot\boldsymbol{e}_j}\left|\Psi_{\boldsymbol{\mu}_A+\oplus k\boldsymbol{\Gamma}_j,\mathbf{0}}\right\rangle. \quad (E.0.18)$$

For a closed linear cluster state the j-th row of the adjacency matrix Γ always contains two entries, which are ones in columns $j-1$ and $j+1$. That is, $\boldsymbol{\Gamma}_j = \boldsymbol{e}_{j-1} + \boldsymbol{e}_{j+1}$. Applied to Equation E.0.18 we have,

$$X_j^k\left|\Psi_{\boldsymbol{\mu}_A,\mathbf{0}}\right\rangle = \omega^{k(d-1)\boldsymbol{\mu}_A\cdot\boldsymbol{e}_j}\left|\Psi_{\boldsymbol{\mu}_A+\oplus k[\boldsymbol{e}_{j-1}\oplus\boldsymbol{e}_{j+1}],\mathbf{0}}\right\rangle. \quad (E.0.19)$$

Overall the equation indicates that shift type errors on one node of a closed linear cluster state are equivalent to phase type errors on the adjacent two vertices. In determining the effect of the error process $\mathcal{M}_j$, we first look at the effect on the identity of subset V_A $\mathbb{1}_{V_A}$,

$$\begin{aligned}
\mathcal{M}_j(\mathbb{1}_{V_A}) &= (1-q)\mathbb{1}_{V_A} + \frac{q}{d}\sum_{k=0}^{d-1} X_j^k\,\mathbb{1}_{V_A}(X_j^k)^\dagger \\
&= (1-q)\mathbb{1}_{V_A} + \frac{q}{d}\sum_{k=0}^{d-1}\sum_{\boldsymbol{\mu}_A} X_j^k\left|\Psi_{\boldsymbol{\mu}_A,\mathbf{0}}\right\rangle\left\langle\Psi_{\boldsymbol{\mu}_A,\mathbf{0}}\right|(X_j^k)^\dagger \\
&= (1-q)\mathbb{1}_{V_A} + \frac{q}{d}\sum_{k=0}^{d-1}\sum_{\boldsymbol{\mu}_A}\left|\Psi_{\boldsymbol{\mu}_A\oplus k[\boldsymbol{e}_{j-1}\oplus\boldsymbol{e}_{j+1}],\mathbf{0}}\right\rangle\left\langle\Psi_{\boldsymbol{\mu}_A\oplus k[\boldsymbol{e}_{j-1}\oplus\boldsymbol{e}_{j+1}],\mathbf{0}}\right| \\
&= (1-q)\mathbb{1}_{V_A} + \frac{q}{d}\sum_{k=0}^{d-1}\sum_{\boldsymbol{\nu}_A}\left|\Psi_{\boldsymbol{\nu}_A,\mathbf{0}}\right\rangle\left\langle\Psi_{\boldsymbol{\nu}_A,\mathbf{0}}\right| \\
&= (1-q)\mathbb{1}_{V_A} + \frac{q}{d}\,d\;\mathbb{1}_{V_A} \\
&= \mathbb{1}_{V_A}. \qquad (E.0.20)
\end{aligned}$$

In the fourth line we noticed that $\boldsymbol{\mu}_A \oplus k[\boldsymbol{e}_{j-1}\oplus\boldsymbol{e}_{j+1}]$ is some vector $\boldsymbol{\nu}_A$, and $\{\boldsymbol{\mu}_A\} \equiv \{\boldsymbol{\nu}_A\}$ up to re-ordering since $\{\boldsymbol{\mu}_A\}$ includes all elements of $\mathbb{F}_d^M$. Having established that the error process preserves the identity of subset V_A, we demonstrate

the effect on binary-like basis vectors,

$$\begin{aligned}\mathcal{M}_j\Big(|\Psi_{\boldsymbol{\mu}_A,\mathbf{0}}\rangle\langle\Psi_{\boldsymbol{\mu}_A,\mathbf{0}}|\Big) &= (1-q)\,|\Psi_{\boldsymbol{\mu}_A,\mathbf{0}}\rangle\langle\Psi_{\boldsymbol{\mu}_A,\mathbf{0}}| \\ &\quad + \frac{q}{d}\sum_{k=0}^{d-1}\Big|\Psi_{\boldsymbol{\mu}_A\oplus k[\boldsymbol{e}_{j-1}\oplus\boldsymbol{e}_{j+1}],\mathbf{0}}\Big\rangle\Big\langle\Psi_{\boldsymbol{\mu}_A\oplus k[\boldsymbol{e}_{j-1}\oplus\boldsymbol{e}_{j+1}],\mathbf{0}}\Big| \\ &= (1-p)\,|\Psi_{\boldsymbol{\mu}_A,\mathbf{0}}\rangle\langle\Psi_{\boldsymbol{\mu}_A,\mathbf{0}}| \\ &\quad + \frac{p}{d-1}\sum_{k=1}^{d-1}\Big|\Psi_{\boldsymbol{\mu}_A\oplus k[\boldsymbol{e}_{j-1}\oplus\boldsymbol{e}_{j+1}],\mathbf{0}}\Big\rangle\Big\langle\Psi_{\boldsymbol{\mu}_A\oplus k[\boldsymbol{e}_{j-1}\oplus\boldsymbol{e}_{j+1}],\mathbf{0}}\Big|, \end{aligned} \tag{E.0.21}$$

where $(1-p) = \frac{1}{d}\big((d-1)(1-q)+1\big)$. □

Proposition 7.4. The effect of the error sequence $\mathcal{M}_{2M}\circ\cdots\circ\mathcal{M}_2(\cdot)$ on the perfect closed linear cluster state, $|\Psi_{\mathbf{0},\mathbf{0}}\rangle$ with $N = 2M$ vertices, where M is odd, can be described using a subset of the basis states $\{|\Psi_{\boldsymbol{\mu}_A,\mathbf{0}}\rangle\}$. Define $\{|\Phi_K\rangle\}$ to be the subset of basis states[2] with the phase type errors Z^{l_1}, Z^{l_2}, $\cdots$, Z^{l_K} on K pairs of next nearest neighbor vertices, such that the error Z^{l_i} applies to both nodes of the i-th pair of next nearest neighbor nodes. Furthermore, if we write a sum over $b_{M,K}\,|\Phi_K\rangle\langle\Phi_K|$, where $b_{M,K} = \binom{M}{K}(d-1)^K$, it is to be interpreted as the sum of all possible samples of states from $\{|\Phi_K\rangle\}$, of which there are $b_{M,K}$. In this notation, the effect of the error sequence is,

$$\begin{aligned}\mathcal{M}_{2M}\circ\cdots\circ\mathcal{M}_2\Big(|\Psi_{\mathbf{0},\mathbf{0}}\rangle\langle\Psi_{\mathbf{0},\mathbf{0}}|\Big) &= (1-p)^M\,|\Psi_{\mathbf{0},\mathbf{0}}\rangle\langle\Psi_{\mathbf{0},\mathbf{0}}| \\ &\quad + \sum_{K=1}^{M}(1-p)^{M-K}\Big(\frac{p}{d-1}\Big)^K b_{M,K}\,|\Phi_K\rangle\langle\Phi_K|. \end{aligned} \tag{7.1.11}$$

Proof.
Equation E.0.21 error process $\mathcal{M}_j$ maps a single closed linear cluster graph basis state into a mixed state consisting of the input state with probability $(1-p)$, and $(d-1)$ states with the additional phase type error Z^l, $l \in \{1,\cdots,d-1\}$ on the next nearest neighbour nodes $j-1$ and $j+1$, each with probability $\frac{p}{d-1}$. Hence $\mathcal{M}_{2M}\circ\cdots\circ\in\Big(|\Psi_{\mathbf{0},\mathbf{0}}\rangle\langle\Psi_{\mathbf{0},\mathbf{0}}|\Big)$ is a mixed state of the perfect closed linear cluster state and the states with phase errors on K of the M pairs of next nearest neighbor nodes in set V_A, where $K \in \{1,\cdots,M\}$. For illustration, we demonstrate here the first few lines of the calculation of $\mathcal{M}_{2M}\circ\cdots\circ\mathcal{M}_2\Big(|\Psi_{\mathbf{0},\mathbf{0}}\rangle\langle\Psi_{\mathbf{0},\mathbf{0}}|\Big)$, for $M > 3$. Recall that we are considering M odd, which impacts the calculations because it

[2] For example: $\{|\Phi_0\rangle\} = \{|\Psi_{\mathbf{0},\mathbf{0}}\rangle\}$,
$\{|\Phi_1\rangle\} = \Big\{\Big|\Psi_{l_1[\boldsymbol{e}_1\oplus\boldsymbol{e}_3],\mathbf{0}}\Big\rangle, \Big|\Psi_{l_1[\boldsymbol{e}_3\oplus\boldsymbol{e}_5],\mathbf{0}}\Big\rangle, \cdots, \Big|\Psi_{l_1[\boldsymbol{e}_{2M-1}\oplus\boldsymbol{e}_1],\mathbf{0}}\Big\rangle\Big\}$,
$\{|\Phi_2\rangle\} = \Big\{\Big|\Psi_{l_1[\boldsymbol{e}_1\oplus\boldsymbol{e}_3]\oplus l_2[\boldsymbol{e}_3\oplus\boldsymbol{e}_5],\mathbf{0}}\Big\rangle, \cdots, \Big|\Psi_{l_1[\boldsymbol{e}_1\oplus\boldsymbol{e}_3]\oplus l_2[\boldsymbol{e}_{2M-1}\oplus\boldsymbol{e}_1],\mathbf{0}}\Big\rangle, \cdots,$
$\Big|\Psi_{l_1[\boldsymbol{e}_3\oplus\boldsymbol{e}_5]\oplus l_2[\boldsymbol{e}_5\oplus\boldsymbol{e}_7],\mathbf{0}}\Big\rangle, \cdots, \Big|\Psi_{l_1[\boldsymbol{e}_3\oplus\boldsymbol{e}_5]\oplus l_2[\boldsymbol{e}_{2M-1}\oplus\boldsymbol{e}_1],\mathbf{0}}\Big\rangle, \cdots\Big\}$

means that each of the basis states in the superposition only occurs once.

$$
\begin{aligned}
\mathcal{M}_{2M}\circ\cdots\circ\mathcal{M}_2\Big(|\Psi_{\mathbf{0},\mathbf{0}}\rangle\langle\Psi_{\mathbf{0},\mathbf{0}}|\Big) &= \mathcal{M}_{2M}\circ\cdots\circ\mathcal{M}_4\Bigg((1-p)|\Psi_{\mathbf{0},\mathbf{0}}\rangle\langle\Psi_{\mathbf{0},\mathbf{0}}| \\
&+\frac{p}{d-1}\sum_{l_1=1}^{d-1}|\Psi_{l_1[\boldsymbol{e}_1\oplus\boldsymbol{e}_3],\mathbf{0}}\rangle\langle\Psi_{l_1[\boldsymbol{e}_1\oplus\boldsymbol{e}_3],\mathbf{0}}|\Bigg) \\
&= \mathcal{M}_{2M}\circ\cdots\circ\mathcal{M}_6\Bigg((1-p)^2|\Psi_{\mathbf{0},\mathbf{0}}\rangle\langle\Psi_{\mathbf{0},\mathbf{0}}| \\
&+(1-p)\frac{p}{d-1}\sum_{l_1=1}^{d-1}|\Psi_{l_1[\boldsymbol{e}_3\oplus\boldsymbol{e}_5],\mathbf{0}}\rangle\langle\Psi_{l_1[\boldsymbol{e}_3\oplus\boldsymbol{e}_5],\mathbf{0}}| \\
&+(1-p)\frac{p}{d-1}\sum_{l_1=1}^{d-1}|\Psi_{l_1[\boldsymbol{e}_1\oplus\boldsymbol{e}_3],\mathbf{0}}\rangle\langle\Psi_{l_1[\boldsymbol{e}_1\oplus\boldsymbol{e}_3],\mathbf{0}}| \\
&+\Big(\frac{p}{d-1}\Big)^2\sum_{l_1=1}^{d-1}\sum_{l_2=1}^{d-1}|\Psi_{l_1[\boldsymbol{e}_1\oplus\boldsymbol{e}_3]\oplus l_2[\boldsymbol{e}_3\oplus\boldsymbol{e}_5],\mathbf{0}}\rangle\langle\Psi_{l_1[\boldsymbol{e}_1\oplus\boldsymbol{e}_3]\oplus l_2[\boldsymbol{e}_3\oplus\boldsymbol{e}_5],\mathbf{0}}|\Bigg) \\
&= \mathcal{M}_{2M}\circ\cdots\circ\mathcal{M}_8\Bigg((1-p)^3|\Psi_{\mathbf{0},\mathbf{0}}\rangle\langle\Psi_{\mathbf{0},\mathbf{0}}| \\
&+(1-p)^2\frac{p}{d-1}\sum_{l_1=1}^{d-1}|\Psi_{l_1[\boldsymbol{e}_5\oplus\boldsymbol{e}_7],\mathbf{0}}\rangle\langle\Psi_{l_1[\boldsymbol{e}_5\oplus\boldsymbol{e}_7],\mathbf{0}}| \\
&+(1-p)^2\frac{p}{d-1}\sum_{l_1=1}^{d-1}|\Psi_{l_1[\boldsymbol{e}_3\oplus\boldsymbol{e}_5],\mathbf{0}}\rangle\langle\Psi_{l_1[\boldsymbol{e}_3\oplus\boldsymbol{e}_5],\mathbf{0}}| \\
&+(1-p)^2\frac{p}{d-1}\sum_{l_1=1}^{d-1}|\Psi_{l_1[\boldsymbol{e}_1\oplus\boldsymbol{e}_3],\mathbf{0}}\rangle\langle\Psi_{l_1[\boldsymbol{e}_1\oplus\boldsymbol{e}_3],\mathbf{0}}| \\
&+(1-p)\Big(\frac{p}{d-1}\Big)^2\sum_{l_1=1}^{d-1}\sum_{l_2=1}^{d-1}|\Psi_{l_1[\boldsymbol{e}_3\oplus\boldsymbol{e}_5]\oplus l_2[\boldsymbol{e}_5\oplus\boldsymbol{e}_7],\mathbf{0}}\rangle\langle\Psi_{l_1[\boldsymbol{e}_3\oplus\boldsymbol{e}_5]\oplus l_2[\boldsymbol{e}_5\oplus\boldsymbol{e}_7],\mathbf{0}}| \\
&+(1-p)\Big(\frac{p}{d-1}\Big)^2\sum_{l_1=1}^{d-1}\sum_{l_2=1}^{d-1}|\Psi_{l_1[\boldsymbol{e}_1\oplus\boldsymbol{e}_3]\oplus l_2[\boldsymbol{e}_5\oplus\boldsymbol{e}_7],\mathbf{0}}\rangle\langle\Psi_{l_1[\boldsymbol{e}_1\oplus\boldsymbol{e}_3]\oplus l_2[\boldsymbol{e}_5\oplus\boldsymbol{e}_7],\mathbf{0}}| \\
&+(1-p)\Big(\frac{p}{d-1}\Big)^2\sum_{l_1=1}^{d-1}\sum_{l_2=1}^{d-1}|\Psi_{l_1[\boldsymbol{e}_1\oplus\boldsymbol{e}_3]\oplus l_2[\boldsymbol{e}_3\oplus\boldsymbol{e}_5],\mathbf{0}}\rangle\langle\Psi_{l_1[\boldsymbol{e}_1\oplus\boldsymbol{e}_3]\oplus l_2[\boldsymbol{e}_3\oplus\boldsymbol{e}_5],\mathbf{0}}| \\
&+\Big(\frac{p}{d-1}\Big)^3\sum_{l_1=1}^{d-1}\sum_{l_2=1}^{d-1}\sum_{l_3=1}^{d-1} \\
&|\Psi_{l_1[\boldsymbol{e}_1\oplus\boldsymbol{e}_3]\oplus l_2[\boldsymbol{e}_3\oplus\boldsymbol{e}_5]\oplus l_3[\boldsymbol{e}_5\oplus\boldsymbol{e}_7],\mathbf{0}}\rangle\langle\Psi_{l_1[\boldsymbol{e}_1\oplus\boldsymbol{e}_3]\oplus l_2[\boldsymbol{e}_3\oplus\boldsymbol{e}_5]\oplus l_3[\boldsymbol{e}_5\oplus\boldsymbol{e}_7],\mathbf{0}}|\Bigg)
\end{aligned}
\tag{E.0.22}
$$

Before introducing a system of grouping terms in the superposition, it remains to be shown that when M is odd each of the terms in the superposition is unique. To illustrate why this is the case, we temporarily relax the restriction on M and give an example. Suppose one wants to write the pair of next nearest neighbor basis vectors $[\boldsymbol{e}_1,\boldsymbol{e}_3]$, using only multiples (mod d) of the pairs of next nearest neighbor vectors in the set $S=\{[\boldsymbol{e}_3,\boldsymbol{e}_5],\ [\boldsymbol{e}_5,\boldsymbol{e}_7],\ \cdots,\ [\boldsymbol{e}_{2M-1},\boldsymbol{e}_1]\}$. If the set S contains an odd number of vectors, the unique non-trivial solution consists of sequentially eliminating all of the vectors other than, $\boldsymbol{e}_1$ and $\boldsymbol{e}_3$ using multiples alternating between 1 and

$(d-1)$ of the vectors from S,

$$[\boldsymbol{e}_1, \boldsymbol{e}_3] = [\boldsymbol{e}_{2M-1}, \boldsymbol{e}_1] \oplus [\boldsymbol{e}_3, \boldsymbol{e}_5] \oplus (d-1)[\boldsymbol{e}_5, \boldsymbol{e}_7] \oplus (d-1)[\boldsymbol{e}_{2M-3}, \boldsymbol{e}_{2M-1}] \\ \oplus [\boldsymbol{e}_{2M-5}, \boldsymbol{e}_{2M-3}] \oplus [\boldsymbol{e}_7, \boldsymbol{e}_9] \oplus \cdots .$$

If the set S contains an even number of vector pairs then no solution is possible. When M is even, then the number of vector pairs in S is odd, whereas when M is odd the number of vectors in S is even. These considerations extend to all possible sums of vectors from the set S, hence when M is odd all basis vectors of the superposition state in Equation E.0.22 are unique.

To obtain a system for grouping the terms in the superposition of Equation E.0.22, define $\{|\Phi_K\rangle\}$ to be the subset of basis states with the phase type errors Z^{l_1}, Z^{l_2}, $\cdots$, Z^{l_K} on K pairs of next nearest neighbor vertices, such that the error Z^{l_i} applies to both nodes of the i-th pair of next nearest neighbor nodes. Furthermore, if we write a sum over $b_{M,K} |\Phi_K\rangle \langle\Phi_K|$, where $b_{M,K} = \binom{M}{K}(d-1)^K$, it is to be interpreted as the sum of all possible samples of states from $\{|\Phi_K\rangle\}$, of which there are $b_{M,K}$. Using this notation, we can fill in the conclusion of the calculation,

$$\begin{aligned}
\mathcal{M}_{2M} \circ \cdots \circ \mathcal{M}_2\Big(|\Psi_{\mathbf{0},\mathbf{0}}\rangle \langle\Psi_{\mathbf{0},\mathbf{0}}| \Big) &= (1-p)^M |\Phi_0\rangle \langle\Phi_0| \\
&\quad + (1-p)^{M-1}\Big(\frac{p}{d-1}\Big)\ b_{M,1}\ |\Phi_1\rangle \langle\Phi_1| \\
&\quad + (1-p)^{M-2}\Big(\frac{p}{d-1}\Big)^2\ b_{M,2}\ |\Phi_2\rangle \langle\Phi_2| \\
&\quad + \cdots + (1-p)\Big(\frac{p}{d-1}\Big)^{M-1}\ b_{M,M-1}\ |\Phi_{M-1}\rangle \langle\Phi_{M-1}| \\
&\quad + \Big(\frac{p}{d-1}\Big)^{M}\ b_{M,M}\ |\Phi_M\rangle \langle\Phi_M| \\
&= (1-p)^M |\Psi_{\mathbf{0},\mathbf{0}}\rangle \langle\Psi_{\mathbf{0},\mathbf{0}}| \\
&\quad + \sum_{K=1}^{M} (1-p)^{M-K}\Big(\frac{p}{d-1}\Big)^K b_{M,K} |\Phi_K\rangle \langle\Phi_K| . \quad \text{(E.0.23)}
\end{aligned}$$

□

Here we proceed by deriving equation 7.1.16

Derivation.
To achieve purification, it is necessary that $\widetilde{F} > F$. To determine the maximum and minimum values of x, that is the values which define the boundary of the purification regime, we look for fixed points in of the fidelity, $\widetilde{F}(x,p) = F(x)$, where $\widetilde{F}$ is as in

Equation 7.1.15, and $F = x + \frac{1-x}{d^M}$. To begin, we work with Equation 7.1.15,

$$\begin{aligned}
\widetilde{F} &= \frac{\left(x(1-p)^M + \left(\frac{1-x}{d^M}\right)\right)^2}{\sum_{K=0}^{M} b_{M,K}\left[x(1-p)^{M-K}\left(\frac{p}{d-1}\right)^K + \left(\frac{1-x}{d^M}\right)\right]^2} \\
&= \frac{\big(xA(p,d) + B(d)\big)^2}{\sum_{K=0} b_{M,K}\Big[x^2\ (1-p)^{2(M-K)}\big(\frac{p}{d-1}\big)^{2K} + \frac{(1-x)^2}{d^{2M}} + 2x\ \frac{1-x}{d^M}(1-p)^{M-K}\big(\frac{p}{d-1}\big)^K\ \Big]} \\
&= \frac{\big(xA(p,d) + B(d)\big)^2}{\sum_{K=0} \binom{M}{K}\Big[x^2\ (1-p)^{2(M-K)}\big(\frac{p^2}{d-1}\big)^K + \frac{(1-x)^2}{d^{2M}}(d-1)^K + 2x\ \frac{1-x}{d^M}\ (1-p)^{M-K}\ p^K\ \Big]} \\
&= \frac{\big(xA(p,d) + B(d)\big)^2}{x^2\big[(1-p)^2 + \frac{p^2}{d-1}\big]^M + \frac{(1-x)^2}{d^M} + 2x\ \frac{(1-x)}{d^M}} \\
&= \frac{\big(xA(p,d) + B(d)\big)^2}{x^2\big[(1-p)^2 + \frac{p^2}{d-1}\big]^M + \frac{(1-x^2)}{d^M}} \\
&= \frac{\big(xA(p,d) + B(d)\big)^2}{x^2C(p,d) + B(d)}.
\end{aligned} \tag{E.0.24}$$

In the fourth line we use the binomial theorem to carry out the sums. The fixed point of the fidelity is then calculated by re-arranging the equation $\widetilde{F}(x,p) = F(x)$, and using the quadratic formula.

$$\begin{aligned}
\widetilde{F}(x,p) &= F(x) \\
\frac{\big(xA + B\big)^2}{x^2C + B} &= x + (1-x)B \\
x^2A^2 + B^2 + 2xAB &= x^3C + x^2(1-x)BC + Bx + (1-x)B^2 \\
0 &= x^2C(B-1) + x(BC - A^2) - \big(2AB - B(1-B)\big)
\end{aligned} \tag{E.0.25}$$

The solutions are,

$$x_\pm = \frac{BC - A^2 \pm \sqrt{\Delta}}{2C(B-1)}, \tag{E.0.26}$$

where $\Delta = \big(A^2 - BC\big)^2 + 4C\big(1-B\big)\big[2AB - B\big(1-B\big)\big]$.

□

F

Verification of numerics

F.1. Sending a qubit GHZ state through depolarization channels

In order to verify the correctness of the numeric implementation of depolarization channels used in Sections 6.3 and 7 we here perform an analytic calculation of the state that results from successively sending each node of a simple graph state through a depolarization channel with fixed parameter value, q. The updates to the density matrix due to the Weyl operators (here these are simply Pauli operators) that make up the channel follows from the relations in Section 4.3. Since the number of terms present in the density matrix describing the state after the action of the depolarizing channel scales as an exponential of the number of nodes in the graph state with base the dimension of the underlying system (qudit dimension), we choose to examine a qubit GHZ type state with 3 nodes for the sake of simplicity. Note that for a three node GHZ type state the set of vertices is $V = \{1,\ 2,\ 3\}$, and since the graph is two colorable, we partition the vertices as $V_A = \{1\}$, $V_B = \{2,\ 3\}$. The edges of the graph are defined by the adjacency matrix

$$\mathbf{\Gamma} = \begin{bmatrix} 0 & 1 & 1 \\ 1 & 0 & 0 \\ 1 & 0 & 0 \end{bmatrix}.$$

Initially, we have a perfect graph state $\rho = |\Psi_{0,00}\rangle \langle \Psi_{0,00}|$. Since the state is at all times diagonal in the graph state basis, each diagonal entry of the density matrix corresponds uniquely to the label of a graph basis state. For maximum clarity, it will be useful to describe the quantum state solely terms of the diagonal entries of its denstiy matrix. We write below the diagonal of the initial density matrix, with each entry explicitly labelled. For the subsequent density matrices, the labels will not be explicitly indicated, but the ordering will remain unchanged from the initial

matrix.

$$\rho = diag\ \big(\{0,00\} = 1,\ \{0,01\} = 0,\ \{0,10\} = 0,\ \{0,11\} = 0,\ \{1,00\} = 0,$$
$$\{1,01\} = 0,\ \{1,10\} = 0,\ \{1,11\} = 0\ \big)$$

We begin by sending the qubit 1, which is in set V_A through the depolarizing channel. The resulting density matrix is

$$\mathcal{E}_1(\rho) = (1-q)\rho + \frac{q}{3}\big(X_1\rho {X_1}^\dagger + Z_1\rho {Z_1}^\dagger + X_1Z_1\rho(X_1Z_1)^\dagger\big)$$
$$\mathcal{E}_1(\rho) = diag(\ (1-q),\ 0,\ 0,\ \tfrac{q}{3},\ \tfrac{q}{3},\ 0,\ 0,\ \tfrac{q}{3}\ ) \tag{F.1.1}$$

Next, qubit 2, which is in set V_B is sent through the depolarizing channel. The resulting density matrix is

$$\mathcal{E}_2 \circ \mathcal{E}_1(\rho) = (1-q)\mathcal{E}_1(\rho) + \frac{q}{3}\big(X_2\mathcal{E}_1(\rho){X_2}^\dagger + Z_2\mathcal{E}_1(\rho){Z_2}^\dagger + X_2Z_2\mathcal{E}_1(\rho)(X_2Z_2)^\dagger\big)$$

$$\mathcal{E}_2 \circ \mathcal{E}_1(\rho) = diag(\ (1-q)^2 + (\tfrac{q}{3})^2,\ 2(\tfrac{q}{3})^2,\ \tfrac{q}{3}(1-q) + (\tfrac{q}{3})^2,\ \tfrac{q}{3}(1-q) + (\tfrac{q}{3})^2, \tag{F.1.2}$$
$$2\tfrac{q}{3}(1-q),\ 2(\tfrac{q}{3})^2,\ \tfrac{q}{3}(1-q) + (\tfrac{q}{3})^2,\ \tfrac{q}{3}(1-q) + (\tfrac{q}{3})^2\ ).$$

Finally, qubit 3, which is in set V_B is sent through the channel. The resulting density matrix is

$$\mathcal{E}_3 \circ \mathcal{E}_2 \circ \mathcal{E}_1(\rho) = (1-q)\mathcal{E}_2 \circ \mathcal{E}_1(\rho) + \frac{q}{3}\big(X_2\mathcal{E}_2 \circ \mathcal{E}_1(\rho){X_2}^\dagger$$
$$+ Z_2\mathcal{E}_2 \circ \mathcal{E}_1(\rho){Z_2}^\dagger + X_2Z_2\mathcal{E}_2 \circ \mathcal{E}_1(\rho)(X_2Z_2)^\dagger\big), \tag{F.1.3}$$

$$\mathcal{E}_3 \circ \mathcal{E}_2 \circ \mathcal{E}_1(\rho) = diag\big((1-q)^3 + 3(1-q)(\tfrac{q}{3})^2 + 4(\tfrac{q}{3})^3,\ (1-q)^2\tfrac{q}{3} + 3(\tfrac{q}{3})^3 + 4(\tfrac{q}{3})^2(1-q),$$
$$(1-q)^2\tfrac{q}{3} + 3(\tfrac{q}{3})^3 + 4(\tfrac{q}{3})^2(1-q),\ (1-q)^2\tfrac{q}{3} + 3(\tfrac{q}{3})^3 + 4(\tfrac{q}{3})^2(1-q),$$
$$3(1-q)^2\tfrac{q}{3} + 5(\tfrac{q}{3})^3,\ (1-q)^2\tfrac{q}{3} + 3(\tfrac{q}{3})^3 + 4(\tfrac{q}{3})^2(1-q),$$
$$(1-q)^2\tfrac{q}{3} + 3(\tfrac{q}{3})^3 + 4(\tfrac{q}{3})^2(1-q),\ (1-q)^2\tfrac{q}{3} + 3(\tfrac{q}{3})^3 + 4(\tfrac{q}{3})^2(1-q)\big). \tag{F.1.4}$$

With the analytic form in hand, it is possible to draw a comparison against the numeric results achieved when each node of a qubit based, 3 node GHZ state is sent through the depolarizing channel with parameter q. For example, setting $q = 0.4$ in the numeric implementation we obtain,

$$\mathcal{E}_3 \circ \mathcal{E}_2 \circ \mathcal{E}_1(\rho) = diag(0.257,\ 0.098,\ 0.098,\ 0.098,\ 0.156,\ 0.098,\ 0.098,\ 0.098). \tag{F.1.5}$$

As can be simply verified by substitution into F.1.4, the numeric results agree with the analytic calculation, hence the numeric implementation of the depolarization channel functions appropriately in this case.

F.2. Comparison to published numerics for the qubit case

In this appendix we restrict all discussion to the case of qubits. Reference [25] presents a purification protocol for qubit TCGS, to which the protocol of Chapter 5 reduces in the qubit case. One method of validating the numeric routines [59] used in Chapters 6 and 7 for assessing the performance of our protocol of Chapter 5 is to compare the results obtained in the qubit case to the results published in [25]. Although differences in the exact quantities presented in each study may be expected to differ since they are reported by independent numeric routines, the qualitative features of the results of our study should be in accordance with those of [25] for us to conclude that our study is functioning appropriately.

The authors of [25] numerically study the performance of the error-less protocol with depolarized input states. Note that the authors use a description of depolarization noise that is different but equivalent to the description given by equation 2.2.6. The alternative description is,

$$\mathcal{E}_j(\rho) = p\rho + (1-p)\frac{\mathbb{1}_j}{2} \otimes \mathrm{Tr}_j(\rho). \tag{F.2.1}$$

The parameter p of equation F.2.1 is related to the parameter q in equation 2.2.6 by $q = \frac{3}{4}(1-p)$. Notice that in this formulation of depolarizing noise the extremal value of noise that can be applied to the state is given by $p_{\min}$. In the figures of this appendix we work with the depolarization noise as in equation F.2.1. In Figure F.1 we plot the results obtained when studying the performance of the error-less protocol with depolarized input states using our numeric routine as well as the data presented in Figure 2 of [25]. One important consideration is that the numeric study determines the value of $p_{\min}$, and $F_{\min}$ simply follows from the value of $p_{\min}$. For this reason we emphasize comparison of the values of $p_{\min}$. From Figure F.1 we see that the qualitative behaviour of our results for $p_{\min}$ are consistent with those of [25]; in particular, for linear cluster states (Figure F.1a) we notice that the observed values of $p_{\min}$ are essentially constant as N increases; for GHZ type states (Figure F.1b) we notice that the observed values of $p_{\min}$ increase as N increases. Another consideration is that the values we report for $p_{\min}$ are consistently higher than those of [25], hence our results can be considered a conservative bound when compared to [25].

Another important case where comparison is available is in the performance analysis of the protocol with faulty two-qubit operations. In Figure F.2 we consider depolarized states as input and faulty two-qubit operations given by Equation 7.0.1 with the error processes of Equation F.2.1; the purification regimes reported by our numeric simulation framework (Figure F.2a) are compared to the results presented in Figure 4 of [25] (Figure F.2b). For each gate error parameter, the purification regime

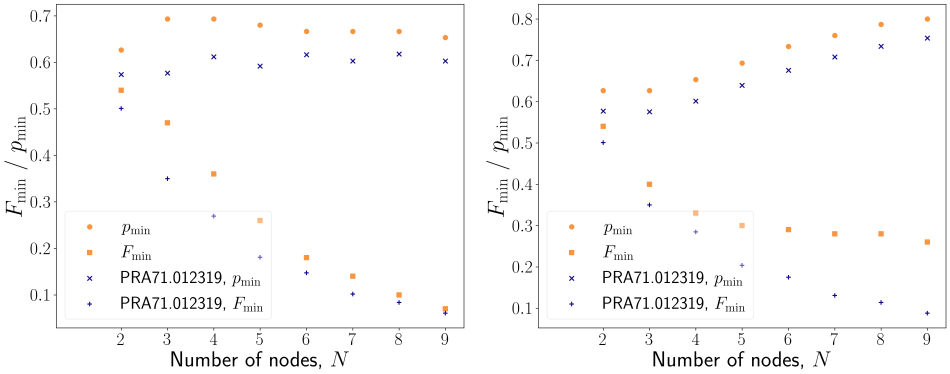

(a) Linear cluster state.

(b) GHZ type state.

Figure F.1: Minimal values of the input state fidelity F and depolarization parameter p for various node numbers, with perfect local operations. Orange dataset (circle and square markers) corresponds to numerics from this work. Blue dataset (x and + markers) corresponds to data extracted from [25] using the plot digitization tool available at https://apps.automeris.io/wpd.

consists of the area between the minimal required input state fidelity to achieve purification and the maximum obtainable output fidelity, for any input state.

From observation of Figure F.2a, we notice that the purification regime broadens with increasing N, and in general both the maximum reachable and minimal required fidelity decrease as N increases, both of which are consistent with Figure F.2b. We note also that the numeric values reported in Figures F.2a and F.2b are similar. We conclude that our numeric simulation of the protocol with faulty two qubit operations captures the qualitative behaviour of the results reported in [25], and we take this as validation that the simulation functions appropriately in this case.

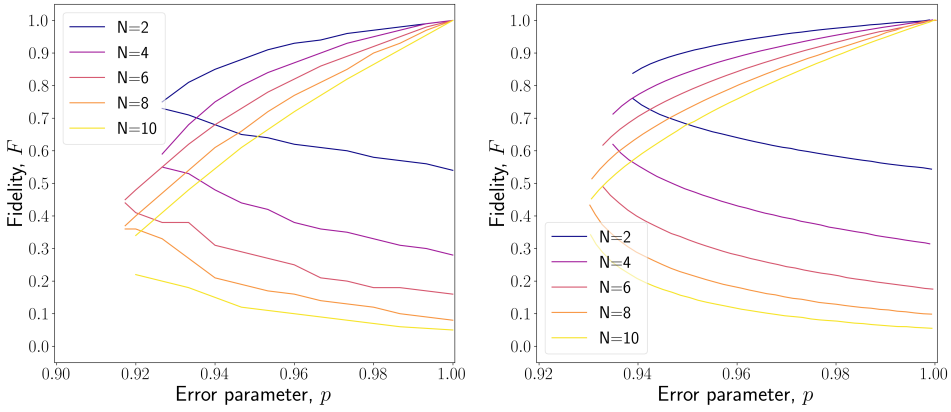

(a) Numeric simulation results.

(b) Results extracted from Figure 4 of [25].

Figure F.2: Purification regimes of depolarized linear cluster input states for various node numbers, N. For each N in both (a) and (b) the critical gate error parameter is the point where the maximum obtainable fidelity and minimum required fidelity converge. Data in (b) was extracted from [25] using the plot digitization tool available at https://apps.automeris.io/wpd.

Bibliography

[1] Gilad Gour and Nolan R. Wallach. "Classification of Multipartite Entanglement of All Finite Dimensionality". In: *Physical Review Letters* 111.6 (Aug. 2013). ISSN: 1079-7114. DOI: 10.1103/physrevlett.111.060502. URL: http://dx.doi.org/10.1103/PhysRevLett.111.060502.

[2] Damian Markham and Barry C. Sanders. "Graph states for quantum secret sharing". In: *Phys. Rev. A* 78 (4 Oct. 2008). DOI: 10.1103/PhysRevA.78.042309.

[3] Adrian Keet et al. "Quantum secret sharing with qudit graph states". In: *Physical Review A* 82.6 (Dec. 2010). DOI: 10.1103/physreva.82.062315.

[4] Robert Raussendorf, Daniel E. Browne, and Hans J. Briegel. "Measurement-based quantum computation on cluster states". In: *Phys. Rev. A* 68 (2 Aug. 2003). DOI: 10.1103/PhysRevA.68.022312.

[5] D. L. Zhou et al. "Quantum computation based on d-level cluster state". In: *Physical Review A* 68.6 (Dec. 2003). DOI: 10.1103/physreva.68.062303.

[6] M. A. Nielsen and I. L. Chuang. *Quantum Computation and Quantum Information*. Cambridge University Press, 2000.

[7] M. Grassl, A. Klappenecker, and M. Rotteler. "Graphs, quadratic forms, and quantum codes". In: *Proceedings IEEE International Symposium on Information Theory,* (). DOI: 10.1109/isit.2002.1023317.

[8] Erik Hostens, Jeroen Dehaene, and Bart De Moor. "Stabilizer states and Clifford operations for systems of arbitrary dimensions and modular arithmetic". In: *Phys. Rev. A* 71 (4 2005). DOI: 10.1103/PhysRevA.71.042315.

[9] M. Hein et al. *Entanglement in Graph States and its Applications*. 2005. URL: https://arxiv.org/abs/quant-ph/0602096.

[10] Daniele Cozzolino et al. "High-Dimensional Quantum Communication: Benefits, Progress, and Future Challenges". In: *Advanced Quantum Technologies* 2.12 (2019). DOI: https://doi.org/10.1002/qute.201900038.

[11] Fern H. E. Watson, Hussain Anwar, and Dan E. Browne. "Fast fault-tolerant decoder for qubit and qudit surface codes". In: *Phys. Rev. A* 92 (3 Sept. 2015). DOI: 10.1103/PhysRevA.92.032309.

[12] Guillaume Duclos-Cianci and David Poulin. "Kitaev's $\mathbb{Z}_d$-code threshold estimates". In: *Phys. Rev. A* 87 (6 June 2013). DOI: 10.1103/PhysRevA.87.062338.

[13] Earl T. Campbell. "Enhanced Fault-Tolerant Quantum Computing in d-Level Systems". In: *Phys. Rev. Lett.* 113 (23 Dec. 2014). DOI: 10.1103/PhysRevLett.113.230501.

[14] Earl T. Campbell, Hussain Anwar, and Dan E. Browne. "Magic-State Distillation in All Prime Dimensions Using Quantum Reed-Muller Codes". In: *Phys. Rev. X* 2 (4 Dec. 2012). DOI: 10.1103/PhysRevX.2.041021.

[15] T. C. Ralph, K. J. Resch, and A. Gilchrist. "Efficient Toffoli gates using qudits". In: *Physical Review A* 75.2 (Feb. 2007). DOI: 10.1103/physreva.75.022313.

[16] Yuchen Wang et al. "Qudits and High-Dimensional Quantum Computing". In: *Frontiers in Physics* 8 (Nov. 2020). DOI: 10.3389/fphy.2020.589504.

[17] Sebastian Ecker et al. "Overcoming Noise in Entanglement Distribution". In: *Physical Review X* 9.4 (Nov. 2019). DOI: 10.1103/physrevx.9.041042.

[18] Hector Sosa-Martinez. *Quantum Control and Quantum Tomography on Neutral Atom Qudits*. 2017. arXiv: 1706.06536 [quant-ph].

[19] Matthew Neeley et al. "Emulation of a Quantum Spin with a Superconducting Phase Qudit". In: *Science* 325.5941 (2009). DOI: 10.1126/science.1173440.

[20] C. Senko et al. "Realization of a Quantum Integer-Spin Chain with Controllable Interactions". In: *Phys. Rev. X* 5 (2 June 2015). DOI: 10.1103/PhysRevX.5.021026.

[21] Manuel Erhard, Mario Krenn, and Anton Zeilinger. "Advances in high-dimensional quantum entanglement". In: *Nature Reviews Physics* 2.7 (June 2020), 365–381. DOI: 10.1038/s42254-020-0193-5.

[22] Manuel Erhard et al. "Experimental Greenberger–Horne–Zeilinger entanglement beyond qubits". In: *Nature Photonics* 12.12 (Oct. 2018). DOI: 10.1038/s41566-018-0257-6.

[23] Christian Reimer et al. "High-dimensional one-way quantum processing implemented on d-level cluster states". In: *Nature Physics* 15 (2 Dec. 2019). DOI: 10.1038/s41567-018-0347-x.

[24] Mario Krenn et al. "Automated Search for new Quantum Experiments". In: *Phys. Rev. Lett.* 116 (9 Mar. 2016). DOI: 10.1103/PhysRevLett.116.090405.

[25] H. Aschauer, W. Dür, and H.-J. Briegel. "Multiparticle entanglement purification for two-colorable graph states". In: *Phys. Rev. A* 71 (1 2005). DOI: 10.1103/PhysRevA.71.012319.

[26] A. Eremenko. *Spectral theorems for hermitian and unitary matrices*. 2017. URL: https://www.math.purdue.edu/~eremenko/dvi/spectral.pdf.

[27] David Gross, Sepehr Nezami, and Michael Walter. *Schur-Weyl Duality for the Clifford Group with Applications: Property Testing, a Robust Hudson Theorem, and de Finetti Representations*. 2021. arXiv: 1712.08628 [quant-ph].

[28] Niel de Beaudrap. *A linearized stabilizer formalism for systems of finite dimension*. 2012. arXiv: 1102.3354 [quant-ph].

[29] Meng-Jun Hu, Xiao-Min Hu, and Yong-Sheng Zhang. "Are observables necessarily Hermitian?" In: *Quantum Studies: Mathematics and Foundations* 4 (3 Sept. 2017). DOI: 10.1007/s40509-016-0098-2.

[30] Vlad Gheorghiu. "Standard form of qudit stabilizer groups". In: *Physics Letters A* 378.5-6 (Jan. 2014), 505–509. DOI: 10.1016/j.physleta.2013.12.009.

[31] J. Eisert and M. B. Plenio. "Introduction to the basics of entanglement theory in continuous-variable systems". In: *Int. J. Quant. Inf.* 1 (4 2003). DOI: 10.1142/S0219749903000371.

[32] John C. Garrison and Jack Wong. "Canonically Conjugate Pairs, Uncertainty Relations, and Phase Operators". In: *Journal of Mathematical Physics* 11.8 (1970). DOI: 10.1063/1.1665388.

[33] Samuel L. Braunstein and Peter van Loock. "Quantum information with continuous variables". In: *Rev. Mod. Phys.* 77 (2 June 2005). DOI: 10.1103/RevModPhys.77.513.

[34] Shubham Dwivedi et al. "Symplectic Vector Spaces". In: *Hamiltonian Group Actions and Equivariant Cohomology*. Cham: Springer International Publishing, 2019. DOI: 10.1007/978-3-030-27227-2_1.

[35] Gernot Alber et al. "Efficient bipartite quantum state purification in arbitrary dimensional Hilbert spaces". In: *Journal of Physics A: Mathematical and General* 34.42 (Oct. 2001). DOI: 10.1088/0305-4470/34/42/307.

[36] Juan Carlos Garcia-Escartin and Pedro Chamorro-Posada. "A SWAP gate for qudits". In: *Quantum Information Processing* 12.12 (Aug. 2013). DOI: 10.1007/s11128-013-0621-x.

[37] John Preskill. *Lecture Notes for Quantum Information, Chapter 3*. 2018.

[38] Grigori G. Amosov. "On Weyl channels being covariant with respect to the maximum commutative group of unitaries". In: *Journal of Mathematical Physics* 48.1 (Jan. 2007). DOI: 10.1063/1.2406054.

[39] Charles H. Bennett et al. "Teleporting an unknown quantum state via dual classical and Einstein-Podolsky-Rosen channels". In: *Phys. Rev. Lett.* 70 (13 Mar. 1993). DOI: 10.1103/PhysRevLett.70.1895.

[40] D. Gottesman. “Stabilizer Codes and Quantum Error Correction”. PhD thesis. Pasadena: Caltech, 1997.

[41] William K. Wootters. “Entanglement of Formation of an Arbitrary State of Two Qubits”. In: *Phys. Rev. Lett.* 80 (10 Mar. 1998). DOI: 10.1103/PhysRevLett.80.2245.

[42] ZhiHao Ma and Xiao-Dong Zhang. *A new entanglement measure: D-concurrence*. 2009. arXiv: 0910.5769 [quant-ph].

[43] H. Bernien et al. “Heralded entanglement between solid-state qubits separated by three metres”. In: *Nature* 497 (2013). DOI: 10.1038/nature12016.

[44] Michael Kues et al. “On-chip generation of high-dimensional entangled quantum states and their coherent control”. In: *Nature* 546 (2017). DOI: 10.1038/nature22986.

[45] W Dür and H J Briegel. “Entanglement purification and quantum error correction”. In: *Reports on Progress in Physics* 70.8 (July 2007), 1381–1424. DOI: 10.1088/0034-4885/70/8/r03.

[46] Charles H. Bennett et al. “Purification of Noisy Entanglement and Faithful Teleportation via Noisy Channels”. In: *Phys. Rev. Lett.* 76 (5 Jan. 1996). DOI: 10.1103/PhysRevLett.76.722.

[47] David Deutsch et al. “Quantum Privacy Amplification and the Security of Quantum Cryptography over Noisy Channels”. In: *Phys. Rev. Lett.* 77 (13 Sept. 1996). DOI: 10.1103/PhysRevLett.77.2818.

[48] Caroline Kruszynska et al. “Entanglement purification protocols for all graph states”. In: *Physical Review A* 74.5 (Nov. 2006). DOI: 10.1103/physreva.74.052316.

[49] Renato Renner. “Symmetry of large physical systems implies independence of subsystems”. In: *Nature Physics* 3 (July 2007). DOI: 10.1038/nphys684.

[50] Alexander Pirker et al. “Entanglement generation secure against general attacks”. In: *New Journal of Physics* 19.11 (Nov. 2017). DOI: 10.1088/1367-2630/aa8086.

[51] J. Miguel-Ramiro and W. Dür. “Efficient entanglement purification protocols for d-level systems”. In: *Phys. Rev. A* 98 (4 2018). DOI: 10.1103/PhysRevA.98.042309.

[52] Michał Horodecki and Paweł Horodecki. “Reduction criterion of separability and limits for a class of distillation protocols”. In: *Phys. Rev. A* 59 (6 June 1999). DOI: 10.1103/PhysRevA.59.4206.

[53] N Gisin and H Bechmann-Pasquinucci. "Bell inequality, Bell states and maximally entangled states for n qubits". In: *Physics Letters A* 246.1-2 (Sept. 1998). DOI: 10.1016/s0375-9601(98)00516-7.

[54] Zihao Li, Yun-Guang Han, and Huangjun Zhu. "Optimal Verification of Greenberger-Horne-Zeilinger States". In: *Physical Review Applied* 13.5 (May 2020). DOI: 10.1103/physrevapplied.13.054002.

[55] Mohsen Bahramgiri and Salman Beigi. "Graph States Under the Action of Local Clifford Group in Non-Binary Case". In: *arXiv e-prints*, quant-ph/0610267 (Oct. 2006). arXiv: quant-ph/0610267 [quant-ph].

[56] Jens Eisert and Hans J. Briegel. "Schmidt measure as a tool for quantifying multiparticle entanglement". In: *Phys. Rev. A* 64 (2 July 2001). DOI: 10.1103/PhysRevA.64.022306.

[57] Achim Kempf. *Lecture Notes: Advanced Quantum Theory*. June 2019.

[58] Barbara Illowsky and Susan Dean. *Introductory Statistics*. 6. Open Access Textbooks, 2018. URL: https://commons.erau.edu/oer-textbook/6.

[59] Scarlett Gauthier. 2021. DOI: 10.5281/zenodo.4675772. URL: https://github.com/scgauthier/Qudit_TCGS.

[60] Axel Dahlberg and Stephanie Wehner. "Transforming graph states using single-qubit operations". In: *Philosophical Transactions of the Royal Society A: Mathematical, Physical and Engineering Sciences* 376.2123 (2018). DOI: 10.1098/rsta.2017.0325.

[61] Maarten Van den Nest, Jeroen Dehaene, and Bart De Moor. "Graphical description of the action of local Clifford transformations on graph states". In: *Phys. Rev. A* 69 (2 Feb. 2004). DOI: 10.1103/PhysRevA.69.022316.